DESIGN AND SYNTHESIS OF LOW-BAND GAP PERYLENE IMIDES

A THESIS SUBMITTED TO THE BOARD OF GRADUATE PROGRAMS

OF

MIDDLE EAST TECHNICAL UNIVERSITY, NORTHERN CYPRUS CAMPUS
BY

SAMUEL ASUMADU-SARKODIE

IN PARTIAL FULFILLMENT OF THE REQUIREMENTS

FOR

THE DEGREE OF MASTER OF SCIENCE

IN

SUSTAINABLE ENVIRONMENT AND ENERGY SYSTEMS

DECEMBER, 2016

Approval of the Board of Graduate Programs

Prof. Dr. Oya Yerin Güneri
Chairperson

I certify that this thesis satisfies all the requirements as a thesis for the degree of Master of Science.

Asst. Prof. Dr. Carter Mandrik
Program Coordinator

This is to certify that we have read this thesis and that in our opinion, it is fully adequate, in scope and quality, as a thesis for the degree of Master of Science.

Asst. Prof. Dr. Mustafa Erkut Özser
Supervisor

Examining Committee Members

Asst. Prof. Dr. Mustafa Erkut Özser	Chemistry Group METU NCC
Asst. Prof. Dr. Erdal Onurhan	Chemistry Group METU NCC
Assoc. Prof. Dr. Ali Muhtaroğlu	EEE Dept. METU NCC
Asst. Prof. Dr. Dizem Arifler	Physics Group METU NCC
Asst. Prof. Dr. Süleyman Aşır	Mat. Sci. and Nanotech. Eng. Dept. Near East University

I hereby declare that all information in this document has been obtained and presented in accordance with academic rules and ethical conduct. I also declare that, as required by these rules and conduct, I have fully cited and referenced all material and results that are not original to this work.

Name, Last name: Samuel Asumadu-Sarkodie

Signature:

ABSTRACT

DESIGN AND SYNTHESIS OF A LOW-BAND GAP PERYLENE IMIDES

Samuel Asumadu-Sarkodie

M.Sc. Sustainable Environment and Energy Systems

Supervisor: Asst. Prof. Dr. Mustafa Erkut Özser

Dye-sensitized solar cells have only achieved between 10% to 12% power conversion efficiency. Therefore, a major advancement in the conversion efficiency would be possible if new materials are developed. In this study, two novel isomerically pure 1, 7-bay substituted perylene-bisimides were designed, synthesized and characterized. The ultimate aim is to expand the solar light harvesting and to improve charge separation and transport abilities. To achieve the goal, a number of various donor substituents were introduced at the core positions of the perylene unit. This led to an enhancement of the spectral response in the red region of the solar spectrum, thus, a step to improving the performance of photovoltaics. The structural and photophysical characteristics of the synthesized new materials were investigated and discussed.

Keywords: Perylene imides, solar cells, low-bandgap, PTCDA, organic photovoltaic

ÖZ

DÜŞÜK BAND ARALIKLI PERİLEN İMİTLERİN TASARIMI VE SENTEZİ

Samuel Asumadu-Sarkodie

M.Sc. Sürdürülebilir Çevre ve Enerji Sistemleri

Tez Yöneticisi: Asst. Prof. Dr. Mustafa Erkut Özser

Boya Duyarlı Güneş Pilleri halen, yalnızca %10-%12 arasında güç dönüşüm verimliliği elde edebilmişlerdir. Verimlilklerinde artış ancak yeni malzemelerin geliştirilmesi ile mümkün olacaktır. Bu çalışmada izomerik olarak saf iki yeni 1,7-sübstitüe perilen-imid tasarlanarak, sentezlenmiş ve karakterize edilmiştir. Nihai amaç malzemelerin güneş ışığı hasatını genişletmek ve yük ayrımı ve taşıma yeteneklerini geliştirmektir. Bu amaçla, bir dizi elektron donör grup, perilen biriminin çekirdek konumlarına eklenmiştir. Böylece, absorbsiyon spektrumlarında kırmızıya kayma elde edilerek, fotovoltaik uygulamalarda verimliliği arttırabilecek bir gelişme sağlanmıştır. Sentezlenen yeni malzemelerin yapısal karakterizasyonları ve fotofiziksel özellikleri araştırılarak tartışılmıştır.

Anahtar Kelimeler: Perilen imidler, güneş pilleri, düşük band aralığı, PTCDA, organik fotovoltaik

DEDICATION

To God be the Glory, great things He has done. This dissertation is dedicated to my wife, Phebe Asantewaa Owusu, my son, Supernatural Emmanuel Asumadu-Sarkodie and the Asumadu-Sarkodie family.

ACKNOWLEDGEMENT

I will bless the LORD at all times: his praise shall continually be in my mouth. My soul shall make her boast in the LORD: the humble shall hear thereof, and be glad. O magnify the LORD with me, and let us exalt his name together (Psalms 34:1-3, KJV). Glory be to the Lord Almighty for His grace and mercies throughout my graduate studies.

Special thanksgiving and gratitude go to my Supervisor and Coordinator of the Chemistry Group, Asst. Prof. Dr. Mustafa Erkut Özser, who has been instrumental and supportive throughout my research in the laboratory and the write-up of this thesis. His seed sowed in my life has made this dissertation successful. I am also grateful to the jury members, Assoc. Prof. Dr. Ali Muhtaroğlu, Asst. Prof. Dr. Erdal Onurhan, Asst. Prof. Dr. Dizem Arifler and Asst. Prof. Dr. Süleyman Aşır.

I acknowledge the technical support of METU-Ankara for the NMR analysis and CIU-Nicosia Engineering Faculty for the Fluorescence Spectroscopy measurements. This project was funded by Middle East Technical University, Northern Cyprus campus under the grant number BAP (FEN-14-D-1).

I sincerely thank the staff of the Chemistry Group and my colleague Teaching Assistants in the Chemistry Laboratory, the Chemistry Research Group (Obaidullah Mohiuddin and Gözde Özeşme), CyFES METU-NCC Bible Club members, and not forgetting all my friends in the 2014/2015 graduate entry class especially Pradeep Herath M. C. Jayaweera and Patrick Rufangura, an alumnus.

Finally, Glory be to God for the life of my wife, Phebe Asantewaa Owusu, my parents, Mr & Mrs Asumadu-Sarkodie, my siblings (Millicent, Adelaide, Daniel, Ebenezer, Patience and Stephen), and my niece and nephews (Rhodah, Benedict and Joshua) for their fervent prayers, love, support and encouragement throughout my studies abroad.

Samuel Asumadu-Sarkodie

TABLE OF CONTENT

ETHICAL DECLARATION iii

ABSTRACT iv

ÖZ v

DEDICATION vi

ACKNOWLEDGEMENT vii

TABLE OF CONTENT viii

LIST OF TABLES xii

LIST OF FIGURES xiii

LIST OF SCHEMES xvii

LIST OF ABBREVIATIONS xviii

CHAPTER 1 1

INTRODUCTION 1

1.1 Background Statement 1

1.2 Problem Statement 4

CHAPTER 2 6

LITERATURE REVIEW 6

2.1 Solar Energy 6

2.1.1 Overview 6

2.1.2 Solar Radiation 7

2.1.3 Photovoltaics 11

2.1.3.1 Overview of Photovoltaics 11

2.1.3.2 History of Photovoltaics 11

2.1.3.3 Photovoltaics: The Global Market 14
2.1.3.4 Photovoltaics: The Cost 16
2.1.3.5 Organic Photovoltaic 17
2.1.3.5.1 Scientific Research on OPV 19
CHAPTER 3 21
THEORETICAL CONCEPT OF DSSC 21
3.1 History of Dye-Sensitized Solar Cells 21
3.2 Configuration of Dye-Sensitized Solar Cell 23
3.3 The Working Electrode 24
3.4 Sensitizer 26
3.5 The Counter Electrode 30
3.6 Electrolyte 31
3.7 Working Principle 35
3.8 Parameters of a Solar Cell 37
3.8.1 Open Circuit Photovoltage 38
3.8.2 Short Circuit Photocurrent 38
3.8.3 Fill Factor 39
3.8.4 Photo Conversion Efficiency 40
3.9 Perylene Diimides 40
3.9.1 Synthesis of Perylene Imides 43
3.9.2 Perylene Diimides Derivatives for DSSC 49
3.9.3 Preparation of Perylene Diimides Derivatives 54
3.9.4 1,7-Di-Substituted Derivatives 58
CHAPTER 4 63
EXPERIMENTAL 63

4.1 Materials and Instruments 63

4.2 Synthetic Procedures 64

4.2.1 Synthesis of perylene-tetracarboxylic tetrabutyl ester (P-1) 64

4.2.2 Synthesis of 1,7-dibromoperylene-3,4,9,10-tetracarboxyl tetrabutylester (P-2) 66

4.2.3 Synthesis of 1,7-Dibromoperylene-3,4,9,10-tetracarboxy monoanhydride Dibutylester (P-3) 68

4.2.4 Synthesis of 1,7-Dibromoperylene-3,4,9,10-tetracarboxylic bisanhydride (P-X) 69

4.2.5 Synthesis of 1,7-Dibromo-N,N'-Bis[2-(diethylamino)ethyl]-3,4,9,10-perylene- tetracarboxylic Diimide (P-4) 70

4.2.6. Synthesis of 1,7-Di(4-tert-butylphenoxy)-N,N'-bis[2-(diethylamino)ethyl]-3,4,9,10-perylene- tetracarboxylic diimide (P-5) 71

4.2.7. Synthesis of 1,7-Di(pyrrolidinyl)-N,N'-bis[2-(diethylamino)ethyl]-3,4,9,10-perylene- tetracarboxylic diimide (P-6) 72

4.3 Data and Calculations 74

4.3.1 Maximum Extinction Coefficient ($\varepsilon_{\max}$) 74

4.3.2 Absorption and Emission Properties 74

4.3.3 Singlet Excitation Energies (E_s) 99

4.3.4 Oscillator Strength (f) 99

4.3.5 Theoretical Radiative Lifetimes ($\boldsymbol{\tau 0}$) 101

4.3.6 Optical Band Gap Energy ($\boldsymbol{Eg}$) 103

4.3.7 Fluorescence Quantum Yield ($\boldsymbol{\Phi F}$) 104

4.3.8 Theoretical Fluorescence Lifetime ($\boldsymbol{\tau F}$) 107

4.3.9 Fluorescence Rate Constant ($\mathbf{k}\boldsymbol{F}$) 107

4.3.10 Rate Constant of Radiationless Deactivation ($\mathbf{k}\boldsymbol{d}$) 108

CHAPTER 5 109

RESULTS AND DISCUSSION 109

5.1 Chemical Synthesis 109

5.2 Physical Properties 114

5.3 Solubility Properties 116

5.4 Optical Properties 118

5.4.1 Steady-State Absorption 118

5.4.2 Steady-State Fluorescence 122

CHAPTER 6 125

CONCLUSION AND FUTURE WORK 125

REFERENCES 128

LIST OF TABLES

Table 4.1. Singlet Excitation Energies for the selected compounds 99

Table 4.2. Half-Width Estimation for the Selected Compounds............................. 101

Table 4.3. Theoretical Radiative Lifetime of Compounds....................................... 102

Table 4.4. Cut-off wavelength of Compounds... 103

Table 4.5. Theoretical Fluorescence Lifetime of P-**4** - P-**6** in $CHCl_3$ 107

Table 4.6. Theoretical Fluorescence Rate Constant of P-**4** - P-**6** in $CHCl_3$ 108

Table 4.7. Rate Constant of Radiationless Deactivation of P-**4** - P-**6** in $CHCl_3$ 108

Table 5.1. Solubility Test for P-**1** - P-**6** 117

Table 5.2. Photophysical data of P-**1** - P-**6** in $CHCl_3$ 120

Table 5.3. Photophysical data of P-**1** - P-**6** in DMF 121

LIST OF FIGURES

Figure 1.1. Breakdown of GHG Emissions by Trade and Industrial Sectors [2]......... 1
Figure 1.2. Global Energy Consumption by Source [11]... 3
Figure 1.3. Global Gross Power Generation Capacity (GW) [12]. 4

Figure 2.1. Electromagnetic Spectrum [68]. 8
Figure 2.2. Solar Radiation [68]... 9
Figure 2.3. Solar spectrum and spectral photon flux density as a function of the frequency v of light multiplied by Planck's constant h [69]. 9
Figure 2.4. Schematic of Air-Mass spectra definition. 10
Figure 2.5. Global Annual PV Installation [96]. 15
Figure 2.6. Cost/Efficiency of Photovoltaic Technology [97]. 17
Figure 2.7. Flat Heterojunction Solar Cell 18
Figure 2.8. Bulk Heterojunction Solar Cell 18
Figure 2.9. Dye Sensitized Solar Cell 19
Figure 2.10. Number of Publications on Organic Photovoltaics 20

Figure 3.1. Schematic representation of the DSSC Makeup..................................... 24
Figure 3.2. Molecular Structure and Band Gap of Semiconductors 25
Figure 3.3. Molecular Structure of chenodeoxycholic acid (CDCA) 27
Figure 3.4. Schematic of a Sensitizer with the Donor-Linker-Acceptor Design 28
Figure 3.5. Molecular Structure of Organic Sensitizers.. 28
Figure 3.6. Molecular Structure of Dyes... 29
Figure 3.7. Molecular Structure of Organic Dyes 30
Figure 3.8. Molecular Structure of Electrolytes (1) 33
Figure 3.9. Molecular Structure of Electrolytes (2) 34
Figure 3.10. Schematic representation of the working DSSC 35
Figure 3.11. Schematic Representation of the Operation Kinetics of a DSSC 37
Figure 3.12. Typical Current-Voltage Characteristic of a Standard Solar Cell 39
Figure 3.13. Molecular Structure of Perylene-3,4,9,10-tetracarboxylic acid............ 41

Figure 3.14. Functionalized Positions of Perylene Core 41
Figure 3.15. Developmental Stages of Perylene Imides 42
Figure 3.16. Synthesis of Perylene Imides in the Peri-Position 43
Figure 3.17. Synthesis of Perylene Imides in the Ortho-Position 45
Figure 3.18. Synthesis of Perylene Imides in the Bay-Position 46
Figure 3.19. Synthesis of Perylene Imides in the Bay + Ortho-Position 47
Figure 3.20. Synthesis of Perylene Imides in the Bay + Peri-Position 48
Figure 3.21. Molecular Structure of Industry Pigments based on PDI 50
Figure 3.22. Molecular Structure of Perylene Diimide Derivatives for DSSC 53
Figure 3.23. Perylene tetracarboxylic acid derivatives 59

Figure 4.1. ^{1}H NMR Spectrum of P-**1** 65
Figure 4.2. ^{13}C NMR Spectrum of P-**1** 65
Figure 4.3. ^{1}H NMR Spectrum of P-**2** 67
Figure 4.4. ^{13}C NMR Spectrum of P-**2** 67
Figure 4.5. ^{1}H NMR spectrum of P-**3** in $CDCl_3$ 69
Figure 4.6. ^{1}H NMR spectrum of P-**4** in $CDCl_3$ 71
Figure 4.7. ^{1}H NMR spectrum of P-**5** in $CDCl_3$ 72
Figure 4.8. ^{1}H NMR spectrum of P-**6** in $CDCl_3$ 73
Figure 4.9. Absorption spectra of P-**1** in $CHCl_3$ 75
Figure 4.10. Absorbance versus Concentration plot of P-**1** at 472 nm in $CHCl_3$ 75
Figure 4.11. Absorbance versus Concentration plot of P-**1** at 443 nm in $CHCl_3$ 76
Figure 4.12. Absorption spectra of P-**2** in $CHCl_3$ 76
Figure 4.13. Absorbance versus Concentration plot of P-**2** at 468 nm in $CHCl_3$ 77
Figure 4.14. Absorbance versus Concentration plot of P-**2** at 443 nm in $CHCl_3$ 77
Figure 4.15. Absorption spectra of P-**3** in $CHCl_3$ 78
Figure 4.16. Absorbance versus Concentration plot of P-**3** at 505 nm in $CHCl_3$ 78
Figure 4.17. Absorbance versus Concentration plot of P-**3** at 484 nm in $CHCl_3$ 79
Figure 4.18. Absorption spectra of P-**4** in $CHCl_3$ 79
Figure 4.19. Absorbance versus Concentration plot of P-**4** at 526 nm in $CHCl_3$ 80
Figure 4.20. Absorbance versus Concentration plot of P-**4** at 491 nm in $CHCl_3$ 80

Figure 4.21. Absorption spectra of P-**5** in $CHCl_3$ 81
Figure 4.22. Absorbance versus Concentration plot of P-**5** at 548 nm in $CHCl_3$ 81
Figure 4.23. Absorbance versus Concentration plot of P-**5** at 512 nm in $CHCl_3$ 82
Figure 4.24. Absorption spectra of P-**6** in $CHCl_3$ 82
Figure 4.25. Absorbance versus Concentration plot of P-**6** at 704 nm in $CHCl_3$ 83
Figure 4.26. Absorbance versus Concentration plot of P-**6** at 435.6 nm in $CHCl_3$ ... 83
Figure 4.27. Absorption spectra of P-**1** in DMF 84
Figure 4.28. Absorbance versus Concentration plot of P-**1** at 469 nm in DMF 84
Figure 4.29. Absorbance versus Concentration plot of P-**1** at 441 nm in DMF 85
Figure 4.30. Absorption spectra of P-**2** in DMF 85
Figure 4.31. Absorbance versus Concentration plot of P-**2** at 466 nm in DMF 86
Figure 4.32. Absorbance versus Concentration plot of P-**2** at 441 nm in DMF 86
Figure 4.33. Absorption spectra of P-**3** in DMF 87
Figure 4.34. Absorbance versus Concentration plot of P-**3** at 497 nm in DMF 87
Figure 4.35. Absorbance versus Concentration plot of P-**3** at 469 nm in DMF 88
Figure 4.36. Absorption spectra of P-**4** in DMF 88
Figure 4.37. Absorbance versus Concentration plot of P-**4** at 523 nm in DMF 89
Figure 4.38. Absorbance versus Concentration plot of P-**4** at 488 nm in DMF 89
Figure 4.39. Absorption spectra of P-**5** in DMF 90
Figure 4.40. Absorbance versus Concentration plot of P-**5** at 541 nm in DMF 90
Figure 4.41. Absorbance versus Concentration plot of P-**5** at 508 nm in DMF 91
Figure 4.42. Absorption spectra of P-**6** in DMF 91
Figure 4.43. Absorbance versus concentration plot of P-**6** at 704 nm in DMF 92
Figure 4.44. Absorbance versus concentration plot of P-**6** at 433 nm in DMF 92
Figure 4.45. Normalized absorption and emission of P-**1** in $CHCl_3$ 93
Figure 4.46. Normalized absorption and emission of P-**2** in $CHCl_3$ 93
Figure 4.47. Normalized absorption and emission of P-**3** in $CHCl_3$ 94
Figure 4.48. Normalized absorption and emission of P-**4** in $CHCl_3$ 94
Figure 4.49. Normalized absorption and emission of P-**5** in $CHCl_3$ 95
Figure 4.50. Normalized absorption and emission of P-**6** in $CHCl_3$ 95
Figure 4.51. Normalized absorption and emission of P-**1** in DMF 96

Figure 4.52. Normalized absorption and emission of P-**2** in DMF 96
Figure 4.53. Normalized absorption and emission of P-**3** in DMF 97
Figure 4.54. Normalized absorption and emission of P-**4** in DMF 97
Figure 4.55. Normalized absorption and emission of P-**5** in DMF 98
Figure 4.56. Normalized absorption and emission of P-**6** in DMF 98
Figure 4.57. Representation of the Half-Width for P-**1** at 472 nm........................... 100
Figure 4.58. Cut-off Wavelength for P-**6** at 770 nm in DMF 104
Figure 4.59. Typical Jablonski Diagram 105
Figure 4.60. Gradient of Standard Sample 106

Figure 5.1. Schematic representation of the synthesized target structures............... 109
Figure 5.2. Picture of P-**1** - P-**6** in chloroform in daylight 115
Figure 5.3. Picture of P-**1** - P-**6** in chloroform under UV light 115
Figure 5.4. Absorption Spectra of P-**1** - P-**6** recorded in (**a**) $CHCl_3$ and (**b**) DMF .. 119
Figure 5.5. Normalized emission spectra of P-**1** - P-**6** in (**a**) $CHCl_3$ and (**b**) DMF.. 123
Figure 5.6. Estimation of Energy Potential 127

LIST OF SCHEMES

Scheme 1.1. Imide Substituent Positions of PDI Preparations (1)............................ 55
Scheme 1.2. Imide Substituent Positions of PDI Preparations (2)............................ 56
Scheme 1.3. Imide Substituent Positions of Asymmetric PDI Preparations............. 57

Scheme 2.1. Synthesis of 1,7-Dibromoperylene-3,4,9,10-tetracarboxy Tetrabutylester (**3**) from PBA (**1**).. 61
Scheme 2.2. Synthesis of 1,7-Dibromo-Substituted Compounds (4-8) from 3 62
Scheme 2.3. Schematic representation of the bromination of perylene bisanhydride 110
Scheme 2.4. Schematic representation of the synthesis of regioisomerically pure 1,7-Dibromoperylene-3,4,9,10-tetracarboxy Tetrabutylester (P-**2**) from PBA (**1**) 111
Scheme 2.5. Tetraester to Bisanhydride formation.. 112
Scheme 2.6. Bisimide formation... 112
Scheme 2.7. Schematic representation of the Synthesis of Regioisomerically Pure 1,7-Dibromoperylene-3,4,9,10-tetracarboxy monoanhydride-dibutylester (**7**) from (**6**) 113

LIST OF ABBREVIATIONS

e^-	Electron
AM	Air mass
$CDCl_3$	Deuterated chloroform
DMF	Dimethylformamide
DSSC	Dye-sensitized Solar Cell
eV	Electronvolt
g	Global
GW	Gigawatt
h	Planck’s constant
IEA	International Energy Agency
IPCC	Intergovernmental Panel on Climate Change
NIR	Near Infrared
NMP	N-Methylpyrrolidone
NMR	Nuclear Magnetic Resonance
NREL	National Renewable Energy Laboratory
PDI	Perylene Diimide
TiO_2	Titanium Dioxide
TW	Terawatt
UV-Vis	Ultraviolet-Visible
v	Frequency
µm	Micrometer
λ	Wavelength

Other symbols and abbreviations are explained in the text

CHAPTER 1

INTRODUCTION

1.1 Background Statement

Global warming has become one of the most vital challenges facing the globe in the impending periods. The Intergovernmental Panel on Climate Change (IPCC) has concluded that the warming of the global climate is as a result of the man-made activities such as deforestation and burning fossil fuels [1]. Figure 1.1 presents the breakdown of greenhouse gas emissions by trade and industrial sectors. Evidence from Figure 1.1 shows that the direct greenhouse gas (GHG) emissions comprise of electricity and heat production (25%), agriculture, forestry and other land use (AFOLU) (24%), industry (21%), transport (14%), other energy (9.6%) and buildings (6.4%). In addition, the breakdown of the 25% greenhouse gas emissions from electricity and heat production is due to buildings (12%), industry (11%), energy (1.4%), AFOLU (0.87%) and transport (0.3%) which are responsible for indirect carbon dioxide emissions.

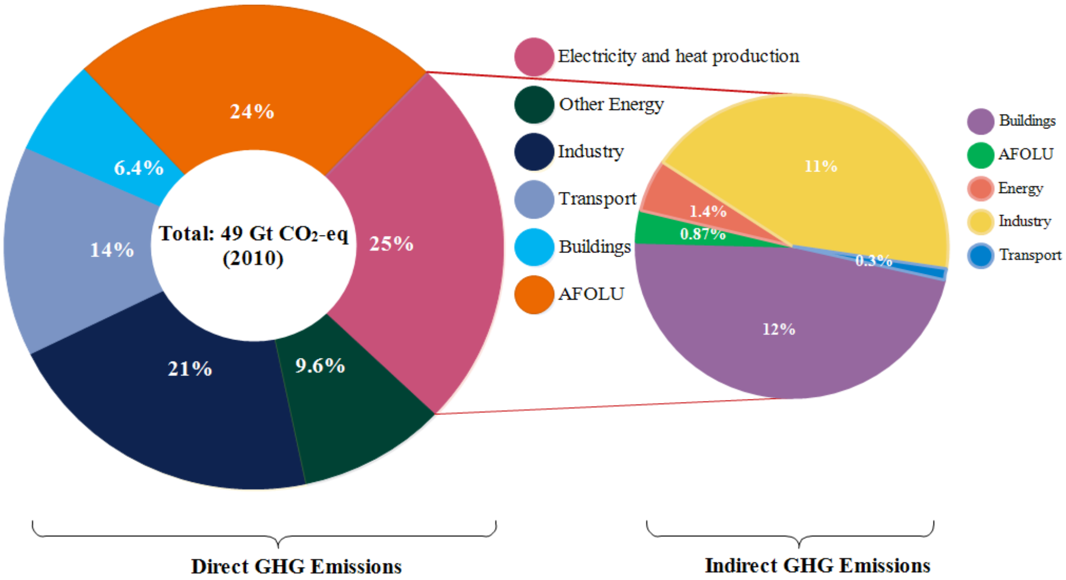

Figure 1.1. Breakdown of GHG Emissions by Trade and Industrial Sectors [2].

Even though the prediction of the actual effects of global warming as a result of climate change and its related impacts are uncertain, nevertheless, developing and utilizing clean and renewable energy sources like solar, wind, and biomass play an important role in the climate change adaptation and mitigation [1, 3, 4]. With the growing global population and energy demand, the availability and accessibility of clean and affordable energy are one of the challenges apart from climate change the world faces within the last decades [5].

The increasing global demand for clean and affordable energy technologies cannot be underestimated due to the waning conventional fuel reserves (i.e. oil, coal and natural gas), which play a role in GHG emissions and subsequently causing global warming. Energy is considered as one of the most important topics in the 21st century [6]. In assumption, the global demand for energy will grow by almost 70% between the year 2000 and 2030. Significantly, 80% of the world’s energy demand is supplied via fossil fuels. In 2002, the global fossil fuel reserves like oil, natural gas and coal were projected to last for; 40 years, 60 years and 200 years [7]. The world’s rate of energy consumption go beyond the 6,000 gigawatts limit and is expected to further increase sharply [8]. This indicates a higher depletion of fossil fuel reserves resulting in a further exacerbation of environmental pollution. In addition to this, the hazards rising from the build-up of plutonium fission products from nuclear reactors threaten the quality of life on earth, unless renewable energy resources are quickly developed [8]. Developing new technologies based on renewable energy sources that provide solutions to the energy problem, as well as address the environmental issues is a great challenge. With the current rapid depletion of fossil fuel based energy, there has being a growing need for clean energy technologies which is widely available, accessible and sustainable. One of the biggest challenges facing humanity is to replace fossil-fuel based energy generation coupled with global warming and its associated climate change with renewable energy sources due to the increasing rate of population and the rising energy demand [9]. As a result, there is an emergence of a global paradigm shift initiated by the IEA, to promote energy security through; a collective response to physical disruptions in fossil fuel based energy supply, by the provision of authoritative research, and analysis on all forms of renewable energy resources. This global action will ensure: a reliable, affordable, accessible, quality, quantity and clean energy provision in a way to reduce greenhouse-gas emissions that contribute to climate change [10]. Figure 1.2 depicts the Global Energy by Source. Evidence from Figure 1.2 shows that in 2014, 86% (11,158.4 mtoe) of the world's primary energy consumption (12,928.4 mtoe) came from fossil fuels while 14% (1,769.9 mtoe) of the world's primary energy consumption came from low-carbon sources like hydropower, solar, wind, biomass and nuclear energy.

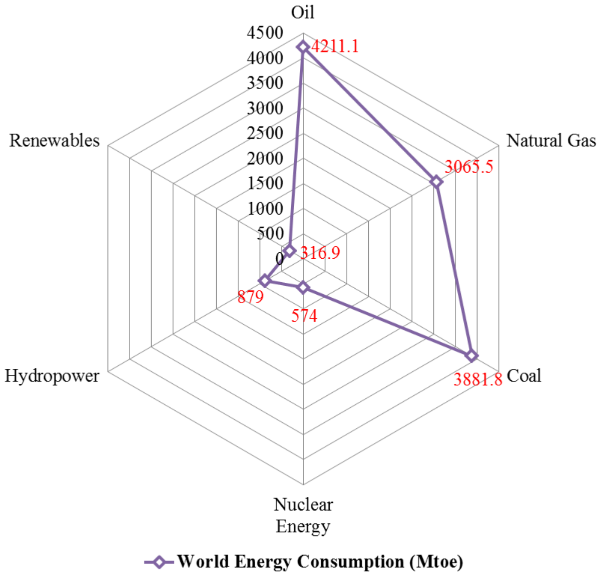

Figure 1.2. Global Energy Consumption by Source [11].

Figure 1.3 depicts the Global Gross Power Generation Capacity. Evidence from Figure 1.3 shows that paradigm shifts in the global gross power generation occurred in 2013 where, clean energy (hydropower, solar, wind, biomass, geothermal and nuclear energy) consumption grew to 143 GW compared to 141 GW of fossil fuel consumption. It is projected that clean energy consumption will increase to 279 GW in 2030 compared to 64 GW of fossil fuel consumption. Evidence from Figure 1.3 shows that solar energy will dominate the clean energy power generation capacity from 2013-2030 and beyond.

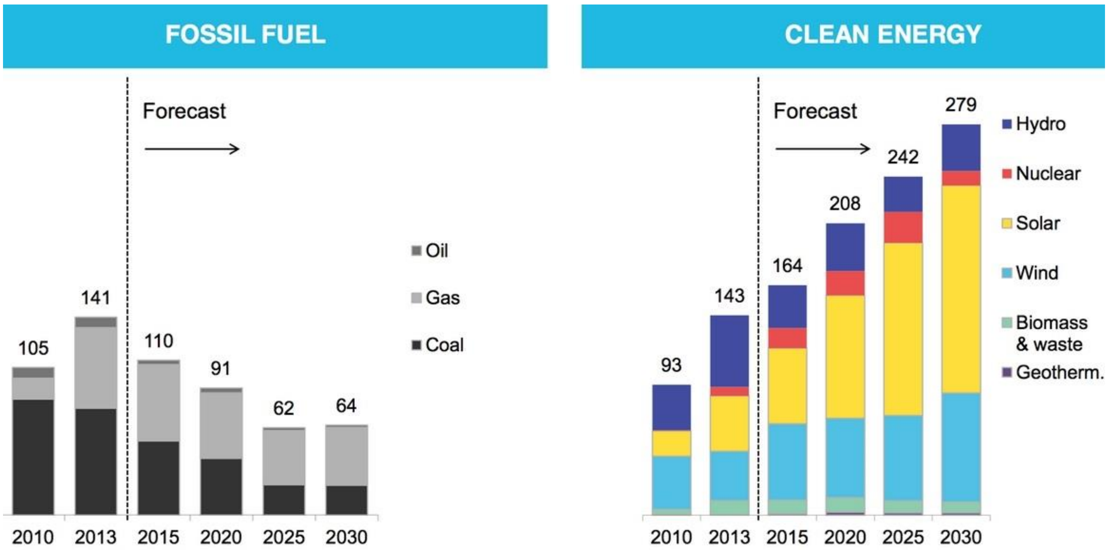

Figure 1.3. Global Gross Power Generation Capacity (GW) [12].

1.2 Problem Statement

In 1954, researchers employed a p–n junction-type of a solar cell to convert the first useful solar radiation into electric energy with 6% efficiency [13]. With the initiation of the space program, photovoltaic cells made from semiconductor-grade silicon rapidly turn out to be the preferred choice of power source for satellites [7]. The solar power conversion efficiencies of most semiconductor-grade silicon were between 15 and 20% [14]. Nonetheless, the comparatively high manufacturing cost of the semiconductor-grade silicon cells disallowed their extensive use in the global market. In addition, the toxicity of the chemicals used for the manufacturing of silicon cells is another disadvantage. These aspects of the conventional devices prompted the study on dye-sensitized solar cells, which are ecologically friendly, and has low-cost solar cell options.

Dye-sensitized solar cells use special dyes to capture the light energy [15-22]. Dye molecules anchored on mesoporous titanium dioxide nanoparticles [23-27], capture the light coming from the sun, which results in photoexcitation. Photoexcitation of the dye initiates redox reactions involving the dye and iodine/triiodide couple [28-31]. As a result, electric current is produced without a net chemical change. The construction of dye-sensitized solar cells is much easier and cheaper compared to silicon-based solar cells [32-39]. Historically, dye-sensitized solar cells have only achieved between 10% to 12% power conversion efficiency [28, 40-60]. Therefore, a major advancement in the conversion efficiency would be possible if new materials are developed [61-63].

The synthesis, characterization, and the study of the photophysical and optical properties of sensitizers are proposed in the study. The study applies a methodology that involves the design, synthesis and characterization of new organic perylene bisimide based dyes as potential sensitizers that may contribute in the direction of improving the power conversion efficiency in dye-sensitized solar cell applications.

CHAPTER 2

LITERATURE REVIEW

2.1 Solar Energy

2.1.1 Overview

The ubiquitous nature of the sun as the source of clean, environmentally friendly, sustainable technology and cheap energy supply has become one of the alternatives to solving the world's energy crisis. The energy from the sun is available freely, abundant globally and recognized as an economically feasible energy source for many solar applications which is worth investing. The solar energy that reaches the earth from the sun is enormous and enduring to a magnitude that, the total annual global energy consumption is provided in a short period like thirty minutes [64]. According to Bauer [65], the life expectancy of the sun, which is the reservoir of solar radiation amounts to 4.5 billion years which makes it effectively inexhaustible. The most incredible thing is that the sun is the cleanest, renewable, and sustainable energy source, which emits neither greenhouse gases nor toxic waste via its exploitation. Among such alternative options of renewable energy technologies are; solar thermal, hydropower, wind, tidal power and wave, liquid fuels derived from biomass and biomass-fired electricity generation. Solar energy technologies like photovoltaics is one of the renewable energy resources that is clean and sustainable alternative sources compared to conventional sources of energy. Photovoltaic is considered as the most promising one, irrespective of their initial capital cost and the area of land used for photovoltaics power system installations. According to Rekioua and Matagne [64], photovoltaic is a technology in which radiant energy from the sun is converted to direct current (DC) electricity. The direct conversion of sunlight into electric power is one of the significant options for renewable energy technologies like photovoltaics.

2.1.2 Solar Radiation

Fossil fuel based energy production is finite and results in carbon dioxide emissions through the combustion process. Gasoline, typically used in combustion engines contains five hydrocarbons and twelve carbon atoms in length. For example, in the combustion of octane, the hydrocarbons react with oxygen thus, releasing carbon dioxide as showed in equation (2.1):

$$2\ \mathrm{C_8H_{18}} + 25\ \mathrm{O_2} \rightarrow 16\ \mathrm{CO_2} + 18\ \mathrm{H_2O} \tag{2.1}$$

Where CO_2 is carbon dioxide emissions, a greenhouse gas (GHG) which is absorbed and emitted as infrared radiation. Thus, the GHG effect is because of the ultraviolet-visible energy of the photons irradiating from the sun onto the earth. The ultraviolet-visible light is absorbed by the earth and re-irradiates infrared photons as the earth heats up. Thus, the temperature of the earth is due to an equilibrium established between the radiation from the sun and the radiated energy into the atmosphere by the earth. The absorption and re-emission of infrared radiation by the greenhouse gases result in global warming [66]. The environmental impact of electricity generation from conventional forms (fossil fuel based energy production) provide more evidence for examining the importance of photovoltaic technology.

The exploitable potential of biomass energy is about 5-7 TW, hydropower energy potential is almost 1.2 TW, geothermal energy is about 1.9 TW, tide/oceanic wave energy is almost 0.7 TW, wind energy is about 14 TW and solar energy is almost 10,000 TW at the surface of the earth [67]. The everyday light experienced is a just a segment of the total emitted energy on the earth by the sun. The solar cell efficiency is delicate to the varying intensity and the dispersal of energy by the sun incident on the earth. Sunlight is a form of electromagnetic radiation that shows a fraction of the electromagnetic spectrum in the form of visible light. Figure 2.1 shows a representation of the electromagnetic spectrum of sunlight. In Figure 2.1, the electromagnetic spectrum describes the visible light as a wave with a specific wavelength, which covers gamma rays, x-rays, ultraviolet, visible, infrared, microwaves, radio and TV waves. Figure 2.2 depicts the solar radiation showing an extra-terrestrial spectrum, a blackbody at 5670 K, visible wavelength and the reference Air Mas 1.5 spectra. Gases, aerosols and dust influence solar radiation through the atmosphere, as they absorb the incident photons. Nevertheless, atmospheric gases such as; ozone (O_3), carbon dioxide (CO_2) and water vapor (H_2O) produces deep channels in the spectral radiation curve due to their high absorption of energy photons as shown in Figure 2.2. Evidence from Figure 2.2 shows that the majority of the UV light lower than 0.3 μm is absorbed by O_3 and a majority of infrared light beyond 2 μm is absorbed by H_2O as well as CO_2 [68].

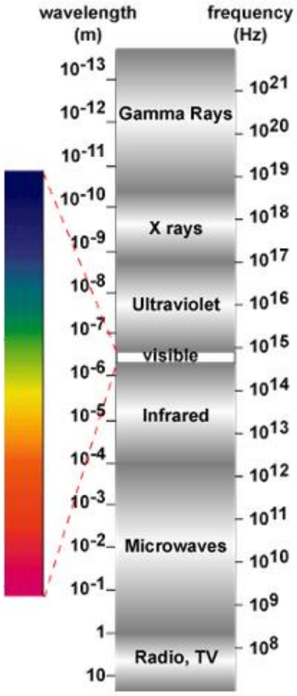

Figure 2.1. Electromagnetic Spectrum [68].

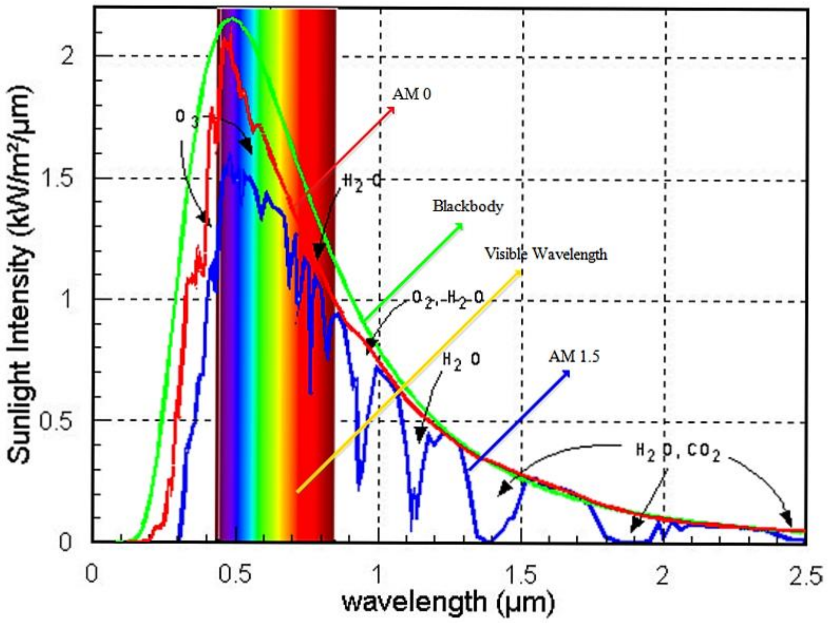

Figure 2.2. Solar Radiation [68].

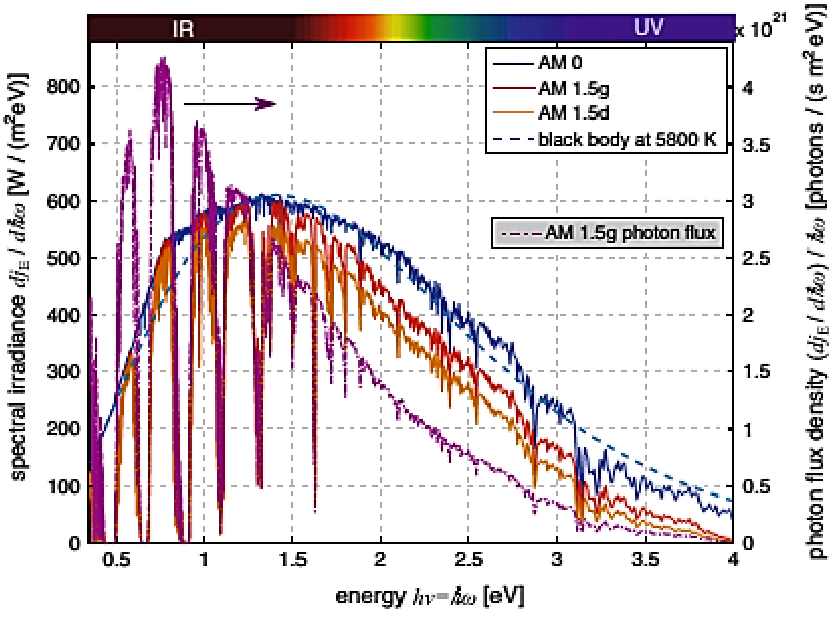

Figure 2.3. Solar spectrum and spectral photon flux density as a function of the frequency v of light multiplied by Planck's constant h [69].

Figure 2.3 depicts the solar spectrum and spectral photon flux density. The spectral energy density ($dj_E/dh\omega$) that is released by the sun and restrained at the sun-earth distance is termed as the solar spectrum depicted in Figure 2.3 (deep-blue line) as a function of frequency v of light multiplied by Planck's constant h (energy). AM 0 represents the air mass of a spectrum measured outside the earth atmosphere with a solar constant of 1,353 W/m^2. Air mass defines sunrays that travel a distance through the atmosphere in multiples of the radial extension of the atmosphere. Accordingly, the air mass measured on the earth's surface is at least one [69]. The air mass (AM 1) is exactly one when the incidence is perpendicular. Figure 2.4 shows the schematic representation of the Air-Mass spectra definition. The air mass on the earth's surface is expressed as $AM = 1/\cos\alpha$. Where, α is the angle of incidence of the sun. At $\alpha =$ 48.2° represents AM 1.5g thus, the standard spectral distribution of the light employed for testing PV devices with a temperature of 25 ℃ and an irradiance of the standard spectrum-per-unit-area and a unit time of 1,000 W/m^2 [70].

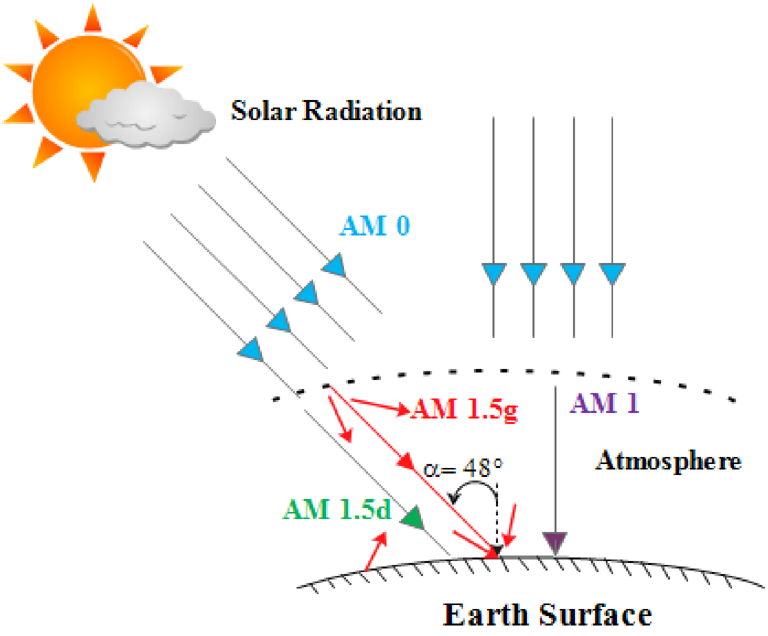

Figure 2.4. Schematic of Air-Mass spectra definition.

For photovoltaic applications, the incident solar energy should exhibit four characteristics in the interaction between the incidence sunlight and the photovoltaic converter. The four characteristics include; the spectral content of the incidence light, the radiant power density from the sun, the angle at which the incidence solar radiation strikes the PV module and the radiant energy from the sun for a particular surface in a day or year [68].

2.1.3 Photovoltaics

2.1.3.1 Overview of Photovoltaics

Photovoltaic solar energy converters are projected to make a significant contribution to the identification of ecologically friendly resolutions to the global energy problem [8]. Electricity from photovoltaic (PV) systems has achieved global prominence and competitiveness in the energy market [71, 72]. The recent sharp drop in the cost of generating electricity using photovoltaic (PV) has triggered an increasing global demand and rapid investment in PV power plants [73] regardless of the intermittent and seasonal variability of solar energy which appears to be the main obstacle impeding its total dependence.

2.1.3.2 History of Photovoltaics

Historically speaking, photovoltaic technology dates back over 160 years where the first scientific discovery photovoltaic effect was made in 1839 by a French Physicist, Alexandre Edmond Becquerel via the experimentation with metal electrodes and electrolyte resulting in a physical phenomenon that allows light-electricity conversion [74]. The photovoltaic effect is expounded as the change of electrical potential existing between two electrodes separated by an appropriate electrolyte. Thus, the photons fall upon a semiconductor and generate an electron-hole pair. Significantly, Edmond Becquerel performed his experiment on liquid photo-electrochemical devices and illuminated solutions that contained metal halide salts. His experiment produced a current between two platinum electrodes submerged in the electrolyte [75]. In 1873, the photoconductivity of selenium was discovered by Smith [76] while in 1883, Charles Fritts discovered his first solar cells made from selenium wafer. In 1886, the photovoltaic effect of selenium was experimented by Hertz [77]. In 1888 and 1901, Edward Weston and Nikola Tesla received their first US patent for solar cell and method of utilizing, and apparatus for the utilization of radiant energy respectively [74, 78].

Lenard [79] discovered in 1904 how the frequency of light plays a role in the energy emitted by electrons. Research advances in 1905, where Albert Einstein elaborated on the theory behind the frequency of light in the energy emitted by electrons photoelectric effect and publishes a paper titled: "*A Heuristic Viewpoint Concerning the Production and Transformation of Light*" [80].

The role of the photovoltaic effect in modern technological advancement is outstanding as it permits a maximum direct changeover of sunlight into electricity. The process involved in photovoltaic effect requires a solar module that is aligned to the sun. Unlike conventional generators with rotating elements, the solar modules do not contain any mechanical wear parts. As a result, there is a long-term stability and low maintenance costs compared to the conventional types of electricity generation [69].

In 1883, the first PV device from selenium film with a large area of 30 cm^2 was manufactured by Fritts [81]. The Bell Laboratory in the US discovered how a voltage was produced by p-n junction diodes under room light. From 1954-1980s, commercial solar age begun on silicon semiconductors, where the photoelectric properties of silicon were discovered leading to the development of silicon solar cells with an efficiency of 6%. Cu_2S/CdS, a thin film heterojunction solar cell achieved an efficiency of 6% within the same year. After a year, RCA Laboratory in the USA reported an efficiency of 6% from gallium arsenide (GaAs) *p-n* junction solar cell [82]. In the same year, Hoffman Electronics in the US sold commercial silicon photovoltaic cells with 2% efficiency for $1500/W. The efficiency of the commercial silicon photovoltaic cells was gradually increased by Hoffman Electronics; 8% in 1957, 9%

in 1958 and 10% in 1959. In 1960, the essential theories of *p-n* junction solar cells were developed to expound the causal link between thermodynamics, temperature, incident-spectrum, band-gap, and the efficiency [83-86].

The first marketable telecommunication satellite Telstar that was power-driven by a PV power system was launched in 1962. Sharp Corporation in Japan produced the first commercial silicon modules in 1963. Remarkably, there is a paradigm shift in clean energy demand, as many countries sought for renewable energy technologies including PVs because of the global oil crisis in 1973. In addition, there was a great improvement in GaAs PV device, as efficiency increased to 13.7% [87].

As the years passes by, there were improvements in the efficiency and the cost of Photovoltaic which led to its popularity as a power source in consumer electronic devices like; radios, watches, calculators, lanterns, and other small-battery-charging gadgets [64, 74, 88]. From 1990-2008, the photovoltaic industry began to grow rapidly due to subsidies introduced by progressive Governments like; Germany, US and Japan to spur its adoption [74].

As the PV technology experienced an exponential increase in the 1980s, the first thin-film solar cell based on cuprous sulphide / cadmium sulphide (Cu_2S/CdS) heterojunction with more than 10% efficiency was made. The Atlantic Richfield Company (ARCO Solar) became the first company to build the largest PV module (100,000; 1' × 4') that produced 5.2 MW in the Carizzo Plain in California and later built a 1 MW grid-connected PV power plant in Hispera, California [89]. In 1985, the researchers of Australia’s University of New South Wales fabricated silicon solar cells with 20% efficiency under standard sunlight in the laboratory.

ARCO Solar manufactured their first commercialized thin film PV array in 1986 while in 1989; British Petroleum (BP) got a thin-film solar cell production patent. In 1990, Siemens acquired ARCO Solar, establishing Siemens Solar which leads to an achievement of 100 MW of power production from the PV modules [90]. In 1997, Siemens Solar became the first solar PV Company to offer a 25-year warranty while SolarWorld entered the Germany’s burgeoning solar market as a start-up business. In

1999, the German Government required utilities to pay feed-in tariffs at a fixed premium rate as a payment for Solar system owners' power contribution to the grid [90].

A number of important events have occurred within the past decades, including the advent of; Cu(InGa)Se_2 polycrystalline thin-film solar cell with 20% efficiency [91], GaInP/GaAs: an ultra-thin and multijunction tandem concentrator cell with an efficiency of 30.2% by the NREL, USA [92], GaInP/GaAs/GaInAs monolithic tandem solar cells for terrestrial concentrator conversion efficiency between 40-45% [93] and a photo-electrochemical DSSCs with 11% efficiency [94].

2.1.3.3 Photovoltaics: The Global Market

There has been a remarkable growth in the PV market in the last decades due to the overwhelming increase in the demand for clean energy [95]. The world's installed PV capacity was over 23 GW at the end of 2009, over 70.5 GW at the end of 2011, almost 100 GW in 2012 and 138.9 GW at the end of 2013-capable of producing at a minimum of 160 TWh of electricity yearly [96]. As of 2013, the installed PV capacity in Europe was 81.5 GW representing 59% thus, making it the leading continent in cumulative installed PV capacity in the world. Asia Pacific countries and the America's follows with a 40.6 GW and 13.7 GW of cumulative installed PV capacity [96]. Nevertheless, the huge potential of solar PV power is receiving much attention in the Middle East, South East Asia, Africa, and Latin America Countries [10, 95, 96].

Figure 2.5 presents the Global Annual PV Installation from 2000 to 2013. The global PV market experienced a high patronization with almost 40 GW installed in 2013 because of a rapid PV power development in Asia, with China alone with 1.1 GW of installed PV capacity. Evidence from Figure 2.5 shows that China achieved the world highest installed PV capacity in 2013 growing from 3.5 GW to 11.8 GW of grid-connected PV. Italy installed 9.3 GW of installed PV capacity in 2011, Germany installed between 7.4 GW and 7.6 GW of PV capacity from 2010-2013. Moreover, Japan installed 6.9 GW of PV capacity in 2013 while the US installed 4.8 GW of PV capacity in 2013 [96].

Evidence from Figure 2.5 shows that Europe has experienced an exponential increase in installed PV capacity from 2 GW in 2007 to 22 GW in 2012 nevertheless, there was a reduction in 2012 and 2013 (about 18 GW and 11 GW) due to economic crisis and unpredictable opposition to the expansion of PV in some European countries. In 2013, the installed PV capacity in Germany, UK, Italy, Romania, and Greece was 3.3 GW, 1.5 GW, 1.4 GW, 1.1 GW, and 1.04 GW respectively. There has being a slow pace in installed PV capacity in the Middle East and Africa (MEA) from 0.1 GW in 2011 to 0.4 in 2013. The Americas have experienced exponential growth in the installed PV capacity from 0.5 GW in 2009 to 5.4 GW in 2013. The Asia-Pacific (APAC) countries have experienced a remarkable increase in the installed PV capacity from 1.6 GW in 2010 to 9.8 GW in 2013. The APAC countries (Japan, Korea, Australia, Taiwan and Thailand) in addition to China were ranked first in the global PV market in 2013 thus, almost 22 GW out of 38.4 GW (56.4%) of the world's PV market compared to Europe's 11 GW (28.6%), Americas' 5.4 GW (14%) and MEA countries' 0.38 (1%).

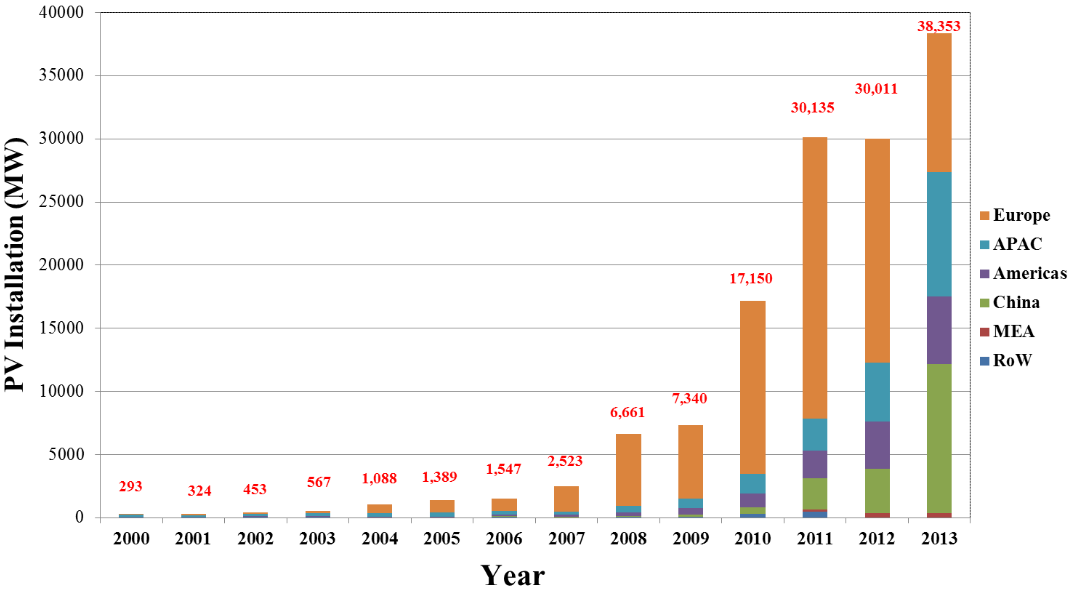

Figure 2.5. Global Annual PV Installation [96].

NB: RoW- Rest of the World, MEA- Middle East and Africa and APAC- Asia Pacific

2.1.3.4 Photovoltaics: The Cost

Presently, the high cost of electricity generation from photovoltaics has become the barrier for market penetration in the Middle East, South East Asia, Africa, and Latin America Countries. Figure 2.6 presents the cost and efficiency of the three generations of solar cells studied at the Australia Research Council (ARC) Photovoltaics Centre of Excellence, University of New South Wales (UNSW). Evidence from Figure 2.6 shows that the first generation (wafer) PV technology has a high production cost per a unit area and moderate possible efficiencies of the PV module level between 14-20%. The short dashes in Figure 2.6 show its corresponding cost per watt thus, the market metric. According to ARC UNSW [97], the market metric (US$1.00/watt-US$3.50/watt) of first generation PV technology is evidential in the Asian manufacturers of first generation products from China. The high cost of the first generation PV technology propelled extensive funding of research into the promising third generation solar cell technology in the UNSW.

The second generation PV technology (thin film) has a lower production cost per a unit area (US$0.50/watt-US$3.50/watt) compared to the first generation PV technology in large scale production and a lower energy-conversion efficiencies of the PV module level between 6-15%.

Evidence from Figure 2.6 shows that the third generation PV technology has the lowest production cost per a unit area (US$0.10/watt-US$0.50/watt) compared to the first and second generation PV technology in large-scale production. Due to its operating principles, there are no constraints in the efficiency of the third generation PV technology compared to the conventional cells of 31% limit. The Shockley-Quiesser 31% limit is only applicable to single-junction cells between 1.25 and 1.45 eV bandgaps operating at AM1.5 global conditions. The limit increases intensely with multijunction concentrator cells which can theoretically utilize the entire photon energy flux from 0.5 to 3.5 eV [98]. Thus, the third generation PV technology focuses on the efficient utilization of the entire solar spectrum with multijunction cells to increase the solar-conversion efficiency greater than 74% if a realistic amount of light is absorbed and utilized [97].

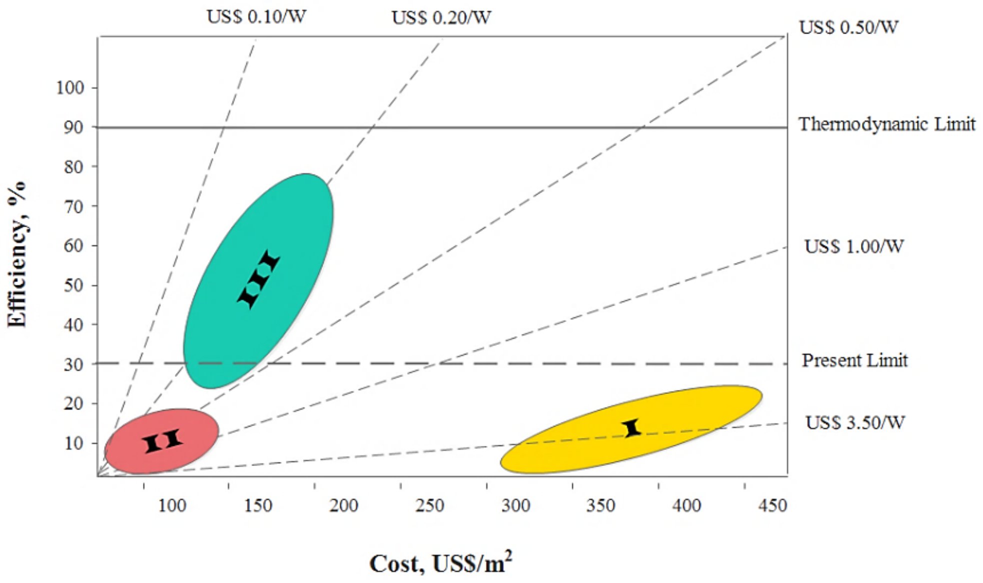

Figure 2.6. Cost/Efficiency of Photovoltaic Technology [97].

2.1.3.5 Organic Photovoltaic

Organic photovoltaic is a new technology that has been developed within the last decades and has experienced the recent development of new classes of solar cells by scientists [99]. Organic photovoltaics can be classified based on their device structures: flat heterojunction solar cell (Figure 2.7), bulk heterojunction solar cell (Figure 2.8) and dye-sensitized solar cell (Figure 2.9) [100].

In flat heterojunction solar cell (Figure 2.7), the donor compound is deposited on the indium tin oxide coated glass/plastic substrate made of transparent conducting electrodes. On top of the donor compound is an acceptor material and on top of the acceptor material are metal electrodes like silver, gold and aluminium deposited by a vacuum sublimation [99].

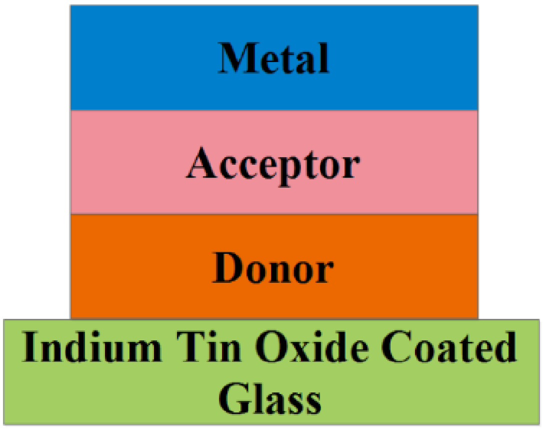

Figure 2.7. Flat Heterojunction Solar Cell

In bulk heterojunction solar cell (Figure 2.8), a mixture of a solution of donor and acceptor like fullerenes are spin-coated on a transparent conducting electrodes followed by an introduction of metal electrodes [99].

Figure 2.8. Bulk Heterojunction Solar Cell

In dye-sensitized solar cell (Figure 2.9), the mesoporous inorganic semiconductor like titanium dioxide is deposited on the fluorine-doped tin oxide coated glass/plastic substrate made of transparent conducting electrodes. The surface of the inorganic semiconductor is then impregnated with a single layer of the dye molecule. A platine coated fluorine-doped tin oxide substrate is then introduced on top of the dye and the semiconductor layer with a subsequent injection of an electrolyte having a redox reagent or a hole-transporting material between the two fluorine-doped tin oxide electrodes [99]. The dye-sensitized solar cell operation is elaborated in Chapter 3.

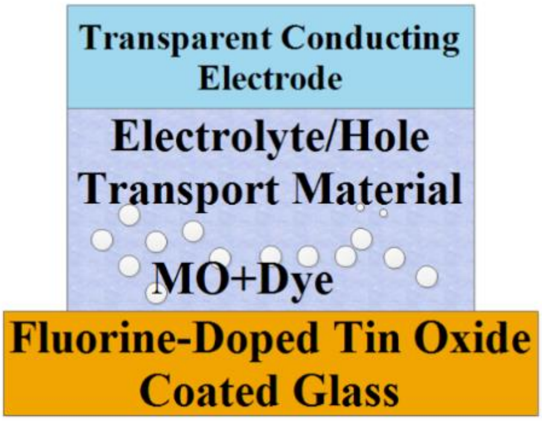

Figure 2.9. Dye-sensitized solar cell

2.1.3.5.1 Scientific Research on OPV

There have been a growing scientific interest and technological advancement in Organic photovoltaics (OPV) within the past decades. A search in Web of Science and Google Scholar on Organic photovoltaics shows a growing scientific research interest within the past decades. Evidence from Figure 2.10 shows that the first scientific research reported in Web of Science was done in 1984 with 3 publications compared to 73 publications in Google Scholar, however; there was a research boom after 2000 and beyond. Currently, there is 12,847 scientific research reported and indexed in Web of Science while a search in Google Scholar on Organic photovoltaics shows a total of 87,229 scientific research papers.

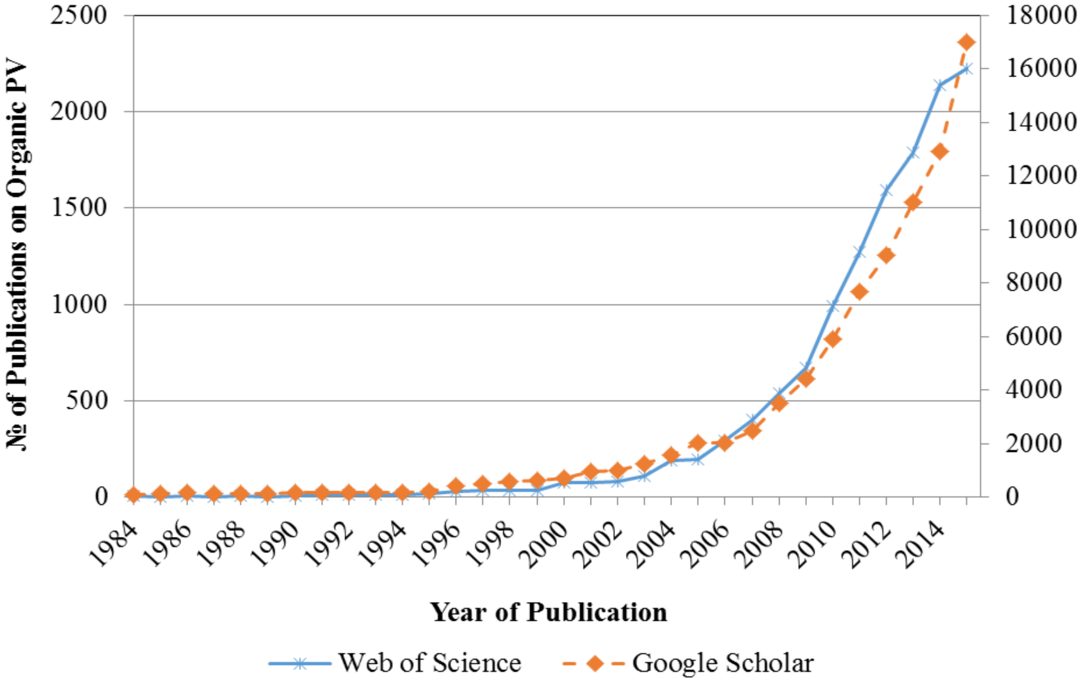

Figure 2.10. Number of Publications on Organic Photovoltaics

CHAPTER 3

THEORETICAL CONCEPT OF DSSC

3.1 History of Dye-Sensitized Solar Cells

Photovoltaic technology is grounded on the principle of charge separation at an interface of two materials of diverse transfer mechanism [101]. So far, the solid-state junction devices, typically made of silicon dominates the photovoltaic technology. This has led to increasing technological advancement, experiences, profits, and availability of materials from the semiconductor industry [101]. According to Grätzel [101], the inorganic solid-state junction devices (semiconductors) that dominants the photovoltaic technology are facing an industrial competition with the development of the third generational solar cells, constructed using nanocrystalline and conducting polymer films. This third generation of solar cells provides the potential of very low cost of fabrication coupled with attractive characteristics that facilitate its commercial access.

Nature makes use of light energy coming from the sun by a process called photosynthesis. Green plants have photosynthetic reaction centers that can be regarded as nature’s energy conversion and storage factory. Photosynthesis involves harvesting solar energy (photons coming from the sun) and using that energy to create a flow of electrons. As a result, the chemical energy generated is used to produce the food (sugar) required for life. Solar cells can be regarded as artificial photosynthetic devices that mimic the light absorption and electron flow of photosynthesis to generate electricity [102].

As a result of this, it is possible to deviate from the conventional solid-state cells which are substituted by devices centered on the interpenetrating network junctions, or by substituting the connection part to the semiconductor by a liquid, a gel, an electrolyte, or a solid, thus creating a photoelectrochemical cell [101, 103]. The outstanding development realized recently in the fabrication and characterization of nanocrystalline materials has opened up vast new opportunities for these systems. Contrary to expectation, devices based on interpenetrating networks of mesoscopic semiconductors have shown extremely high conversion efficiencies, which compete with those of conventional devices [101, 104]. Conventional-type of organic photovoltaic devices uses a donor and an acceptor type of organic materials, which form a heterojunction favouring the separation of the exciton into two carriers. The formed carriers are then transported to the electrodes by the same organic materials that are used for the generation of an exciton. A material for classical-type of organic photovoltaic devices in theory should have a characteristic of both good light harvesting properties and good carriers transporting properties which in practice is a difficult task to achieve. Conversely, the dye-sensitized solar cell technology separates the two requirements as the charge generation is done at the semiconductor-dye interface and the charge transport is done by the semiconductor and the electrolyte. In other words, the prototype of this family of dye-sensitized solar cell recognizes the optical absorption and the charge separation processes by the association of a sensitizer as light-absorbing material with a wide band gap semiconductor of nanocrystalline morphology [101, 104, 105]. The optimization of the spectral properties can be done by modifying the dye alone, whereas carriers transport properties can be improved by optimizing the semiconductor and the electrolyte composition [9].

In 1887, the first sensitization of photoelectrode was reported [106, 107]. Nonetheless, the mechanism of operating by injecting electrons from photoexcited dye molecules into the conduction band of a n-type semiconductor substrates dates back from 1960s where Tsubomura, Matsumura [108] and Gerischer, Michel-Beyerle [109] employed ZnO as a semiconductor and different dyes like rose Bengal used as photosensitizer [110]. In 1981, this concept was developed with the chemisorption of the dye on the surface of a semiconductor [9, 111] followed by the use of dispersed particles to provide sufficient interface area [112]. In 1991, O'Regan and Gratzel [105] first reported dye-sensitized nanocrystalline TiO_2 solar cells based on a fast regenerative photo-electrochemical mechanism. The energy conversion efficiency of dye-sensitized nanocrystalline TiO_2 solar cells was 7.1-7.9% under simulated solar light which is comparable to the efficiency of amorphous silicon solar cells [113].

Importantly, the mesoporous nature of the semiconductor layer is an essential feature in dye-sensitized solar cells, thus providing it with a high surface area. As a result, it increases the light harvesting efficiency of dye-sensitized solar cells. It is an important requirement for the cell since a planar surface covered with a monolayer of a strongly absorbing sensitizer cannot absorb more than 1% of the light [114].

3.2 Configuration of Dye-Sensitized Solar Cell

Different components make-up the dye-sensitized solar cell namely: a conducting glass substrate, a porous layer with semiconductor nanoparticles known as the photo anode, a sensitizer, an electrolyte with a redox couple and a counter electrode as shown in Figure 3.1. Figure 3.1 depicts the schematic representation of the DSSC Makeup.

The catalyst is deposited on the conducting glass which behaves as a counter electrode. Significantly, the catalyst speeds-up the charge transfer between the electrode and the liquid solution.

The photoanode is sensitized by a monolayer of dye molecules, liable to the absorption of light and the generation of photoelectrons. To achieve a relatively high light absorption and a higher photoconversion efficiency in the solar cell, the photoanode is made up of a nanostructure with a high specific surface area to ensure a greater attachment of a number of dye molecules to the surface.

The electrolyte with a redox couple infiltrates the pores of the nanostructured photoanode to have a close proximity with the molecules of the sensitizer. The electrolytic solution conducts holes via a redox couple and regenerate the oxidized dye molecules in order to close the electrical circuit [115].

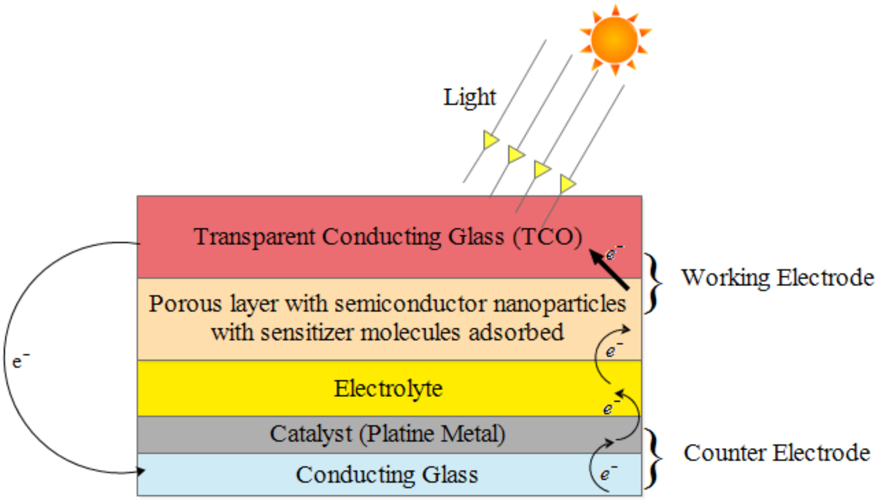

Figure 3.1. Schematic representation of the DSSC Makeup

3.3 The Working Electrode

The working electrode is made up of a mesoporous wide band-gap semiconductor layer mostly titanium dioxide. Compared to past studies in photo-electrochemical systems, a monolayer of semiconductor was employed, which could absorb limited light and only inject electrons into the semiconductor once is bounded to the surface. Using a mesoporous layer rather than a monolayer of semiconductor can enhance the surface area in a thousand fold. The inception of mesoporous layers can enhance the absorption of light photons. There is a similarity of mesoporous semiconductor layer in nature, where the surface area can be increased by piling the chlorophyll having thylakoid membranes to grana structures [66]. The nanoparticle must have an electrical conduction pathway to be more effective. The nanoparticle layer is about 10 μm thick and a size of 10-30 nm. The mesoporous layer is deposited on a transparent conducting oxide like fluorine-doped tin oxide, on either plastic or a glass substrate. Figure 3.2 presents the molecular structure of various semiconductors along with their energy band gap. The development of dye-sensitized solar cells in history has employed several semiconductors including; Gallium Arsenide (GaAs) with energy band gap of 1.4 eV, Gallium Phosphide (GaP) with an energy band gap of 2.25 eV, Cadmium Selenide (CdSe) with an energy band gap of 1.7 eV, Cadmium Sulphide

(CdS) with an energy band gap of 2.25 eV, Zinc Oxide (ZnO) with an energy band gap of 3.2 eV, Iron (III) Oxide (Fe_2O_3) with an energy band gap of 2.1 eV, Tungsten Trioxide (WO_3) with an energy band gap of 2.6 eV, Tin Dioxide (SnO_2) with an energy band gap of 3.8 eV, Silanyliumylidynemethanide (SiC) with an energy band gap of 3.0 eV and Titanium Dioxide (TiO_2) with an energy band gap of 3.2 eV [116].

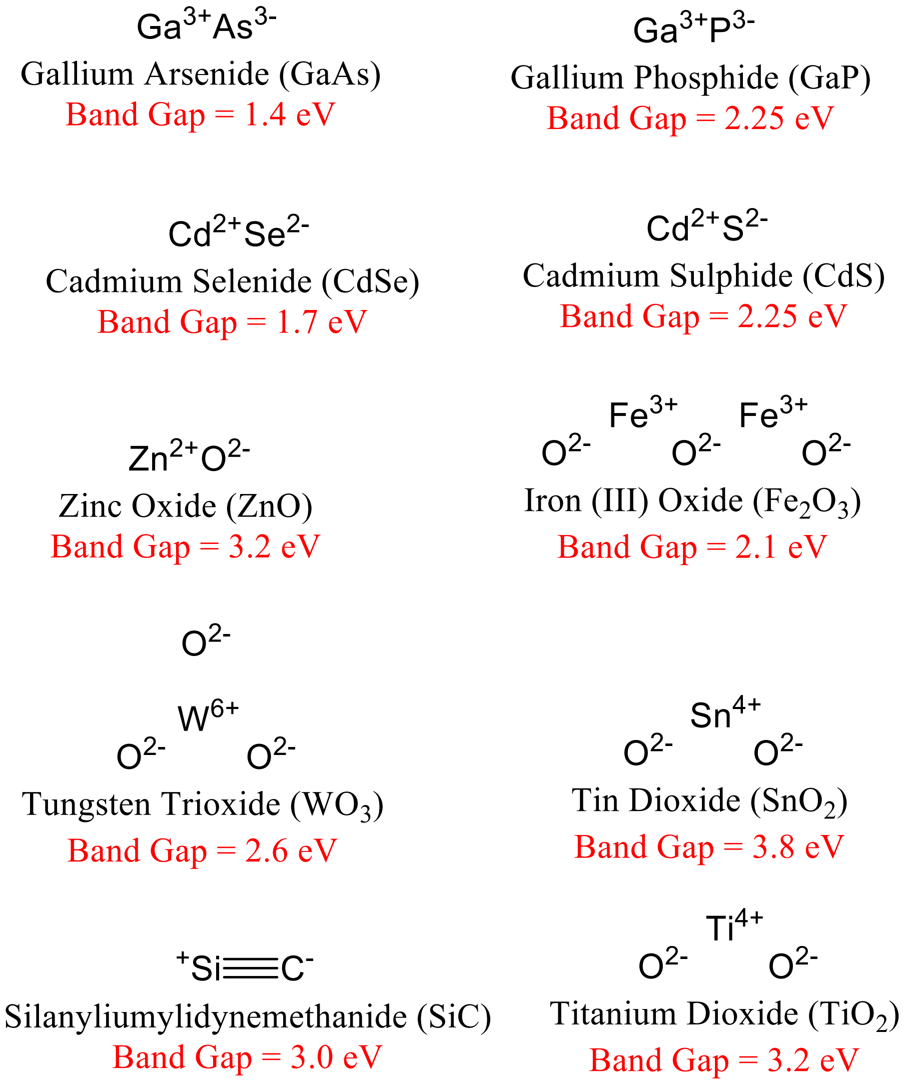

Figure 3.2. Molecular Structure and Band Gap of Semiconductors

3.4 Sensitizer

The sensitizer is the core of the dye-sensitized solar cell with a role of absorbing light photons and generating electrons which are then injected into the conduction band of the semiconductor, where it is chemisorbed. Significantly, the dye only affects the light harvesting efficiency and the overall photoelectric conversion efficiency of the solar cell.

Once the light photons have been absorbed, an electron is pushed from the fundamental state thus, the Highest Occupied Molecular Orbital (HOMO) to the excited state thus, the Lowest Unoccupied Molecular Orbital (LUMO). If the LUMO and the semiconductor conduction band are in favourable positions, the electron can move into the oxide material from the highest energetic orbital. It is important for the dye's excited state to be a bit higher in energy than the semiconductor conduction band of the oxide material to easily allow the injection of the excited electrons. For the efficient dye regeneration, the HOMO level of the dye must be at the lower energy than the redox potential of the electrolyte [117]. The aforementioned reasons make the selection of a dye-electrolyte and dye-semiconductor pairs of significance in the efficient dye-sensitized solar cell operation. A good sensitizer should have an absorption range property thus, the longer the absorption ranges, the higher the cell efficiency. The dye should have a light absorption spectrum range from the ultraviolet region to the infrared region, with an absorption peak in the visible region. Again, in order to obtain a stable chemical bond and a low charge transfer resistance in the dye-sensitized solar cell, the dye should be strongly anchored to the surface of the oxide material [118].

A sensitizer should have an easy synthesis for future large scale production, be low in toxicity, able to recycle, must have a high photo stability for at least 20 years and must block the recombination pathways in order to attain a long-lifetime of the injected electrons [119].

In order to increase the decay from the excited state to the fundamental state and subsequently reduce the electron injection into the semiconductor conduction band, the dye must not suffer in aggregation: as dyes tend to aggregate each other on the oxide material surface.

Integrating different groups into the dye molecule can alter the properties of the organic sensitizers. The performance of the solar cell can be improved by shifting the energy levels, fine-tuning the sensitizer to increase the long wavelength absorption property, and choosing the correct sensitizer design. Organic dyes are beneficial in the easily structural modification, higher extinction coefficients, and are less harmful to the environment compared to other transitional metal complexes. Nevertheless, Organic dyes have narrow absorption bands, stability problems and a higher propensity to aggregate compared to other transitional metal complexes [119]. Recent studies employ additives like chenodeoxycholic acid (CDCA) (see Figure 3.3) to serve as a co-adsorbent with the sensitizer to minimize dye aggregation thus, enhancing the electron injection which improves photo-voltage and current [120, 121].

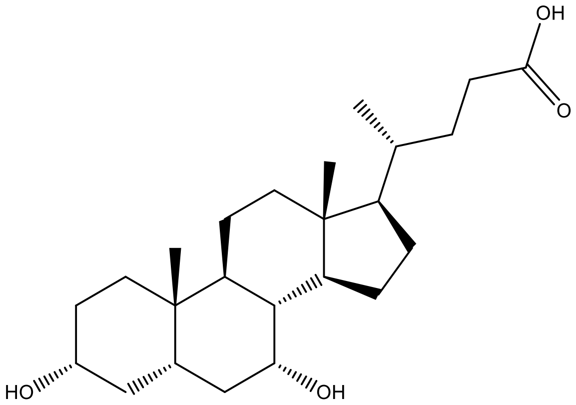

Figure 3.3. Molecular Structure of chenodeoxycholic acid (CDCA)

The Donor-Linker-Acceptor (D-π-A) strategy is the common way of designing organic dyes. Figure 3.4 shows a schematic representation of a sensitizer with the Donor-Linker-Acceptor design. In the D-π-A strategy design, the dye molecule consists of an electron donor, a conjugated linker and an electron acceptor, as shown in Figure 3.4.

Figure 3.4. Schematic of a Sensitizer with the Donor-Linker-Acceptor Design

Upon excitation, the structure of the dye molecule yields an intramolecular charge separation essential for the dye-sensitized solar cell operation. Many molecular structures have been utilized as organic dyes since the inception of the dye-sensitized solar cell. Such organic sensitizers include perylene [122, 123], carbazole [124], indoline [125], hemicyanine [126], triarylamine [127-129], and coumarine [130]. The conjugated linker in the D-π-A strategy design can either be an aromatic compound like thiophene [131] or some chains of methine units. On the other hand, 2-cyanoacrylic acid is the most common acceptor used in the D-π-A strategy design.

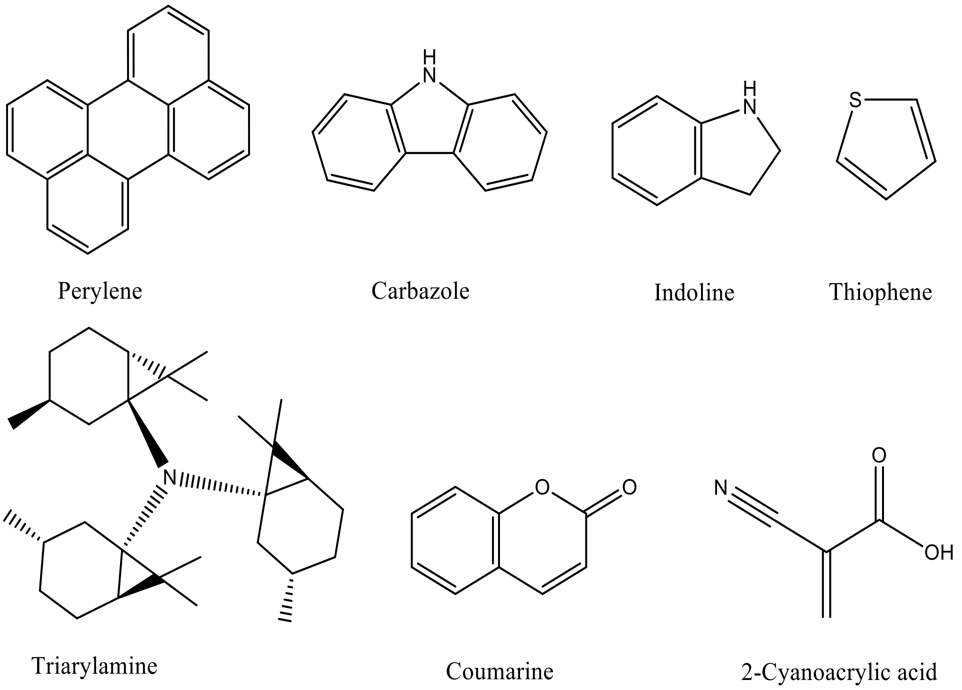

Perylene

Carbazole

Indoline

Thiophene

Triarylamine

Coumarine

2-Cyanoacrylic acid

Figure 3.5. Molecular Structure of Organic Sensitizers

In subsequent years, the development of sensitizers was mainly based on organometallic compounds. For example, ruthenium based sensitizers like N3, N719 and Black dyes were sensitized to increase their efficiencies more than 11% [132-135]. Metal-free organic dyes like C219 has 10% efficiency [136] while non-noble metal sensitizers like green coloured porphyrin dye YD-2 has an efficiency of 11% [137, 138].

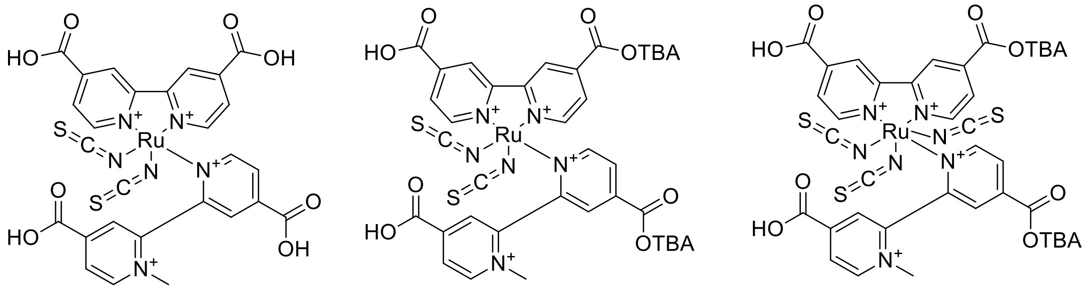

TBA=Tetra-butylammonium cation

Ruthenium N3 Ruthenium N719 Ruthenium Black dye

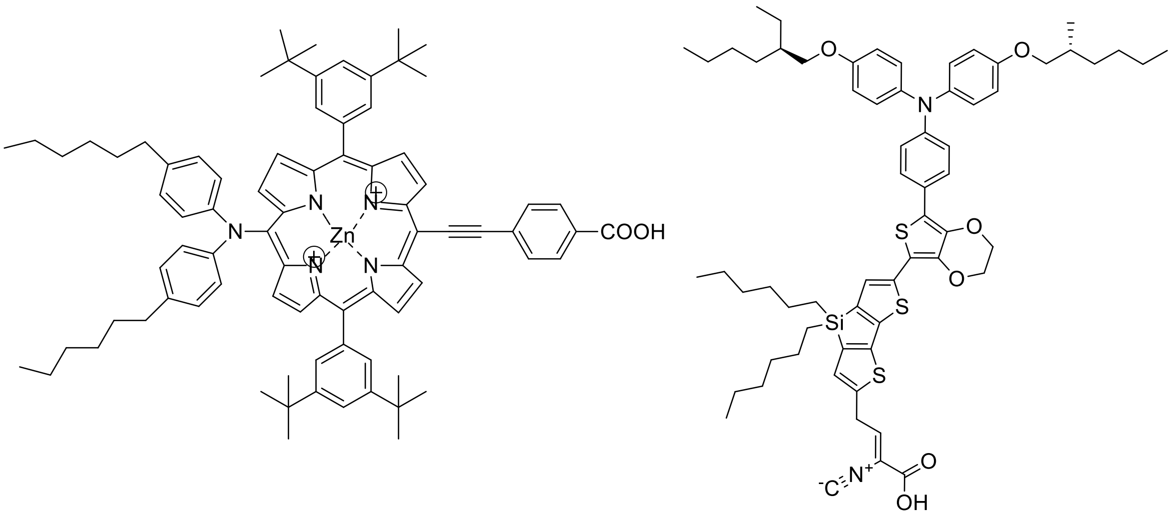

Porphyrin Dye YD-2 Organic Dye C219

Figure 3.6. Molecular Structure of Dyes

Some organic dyes from conjugated polymer like poly(3-thiophene acetic acid), carboxylated poly (p-phenylene ethynylene), and carboxylated polythiophene, have emerged with promising features such as easy deposition on various substrates, large absorption coefficient, multiple binding sites and tunable energy levels.

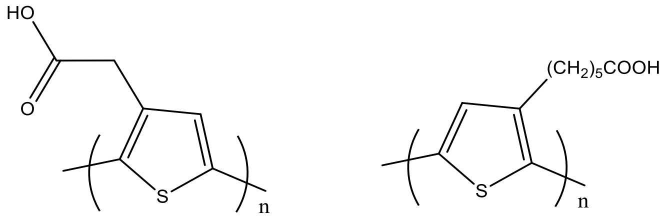

Poly(3-thiophene acetic acid)   Carboxylated polythiophene

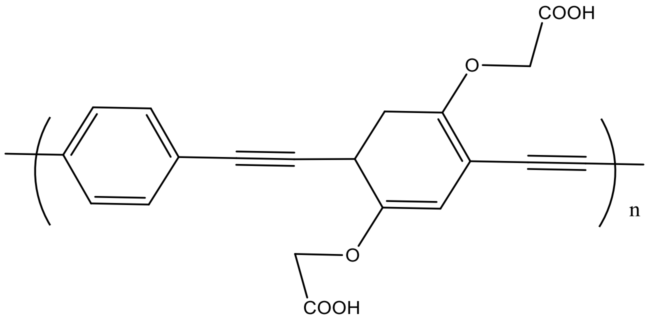

Carboxylated poly(p-phenylene ethynylene)

Figure 3.7. Molecular Structure of Organic Dyes

3.5 The Counter Electrode

The counter electrode is made up of a conducting layer on a plastic substrate or on a glass. The substrate is normally coated with a layer of platinum or carbon-based materials in order to increase the efficient regeneration of the redox couple. In addition, coating the substrate with a catalyst ensures adequately fast reduction kinetics at the transparent conducting glass-coated cathode [139]. Platinum is the commonly used catalyst in dye-sensitized solar cells due to its high values of current and voltage, and low counter electrode resistance [140]. However, platinum has been proven unstable in iodide-based electrolytes. Against the backdrop, a new platinum catalyst known as ‘platinum thermal cluster catalyst’ have been discovered to provide higher kinetic performance in relationship to conventional platinum deposition methods. The platinum thermal cluster catalyst reduces cost due to low platinum loading and exhibits a high mechanical stability and optical transparency of the counter electrode surface [115].

Apart from the outstanding role of platinum in catalytic action, platinum has a disadvantage of being expensive. The high cost of platinum has led to the discovery of a low cost catalyst like graphite as a counter electrode [141]. Other counter electrodes employed in dye-sensitized solar cells include polymers and carbon black [141-144].

3.6 Electrolyte

The electrolyte system plays a crucial role in the efficient transport of electrons in dye-sensitized solar cell operation. Electrolytes used in a dye-sensitized solar cell should meet the following criteria [115]:

1. In order to avoid issues pertaining to dye degradation from the oxide surface, the electrolyte must exhibit a long-term chemical, optical, thermal, and electrochemical stability property.
2. The electrode must have a carrier-transport function between the working electrode and the back electrode. The oxidized dye should regenerate and report to its ground state after the injection of the electrons into the conduction band of the oxide material.
3. The electrolyte must not show absorption properties in the visible range of light.
4. The electrolyte must safeguard the fast diffusion of the charge carrier into the solar cell device and create a good contact with the counter electrode and the porous nanocrystalline oxide layer.

Iodide-triiodide (I^-/I_3^-) is usually used as a redox couple in a liquid electrolyte like acetonitrile (CH_3CN) in mostly common hole-conducting medium in dye-sensitized solar cell operations. Due to the low boiling point (78℃) of acetonitrile, 3-methoxypropionitrile (MPN) [145] with a high boiling point (164℃) and low toxicity is a preferable candidate for long-term stability test in dye-sensitized solar cell operations. Some solvents used in dye-sensitized solar cells include gamma-butyrolactone, propylene carbonate, ethanol, acetonitrile, glutaronitrile, valeronitrile, 3-methoxypropionitrile, methoxyacetonitrile, water, and propionitrile. Nonetheless, Water, ethylene carbonate, propylene carbonate, and ethanol are the less used solvents [146].

Some limitations exist with volatile electrolytes as it leads to long-term stability concerns because of difficulties in sealing the operating device. Nevertheless, research has proven that a change from volatile electrolytes to non-volatile ionic liquids or gelification of the solvent provides the best stability whereas organic nitrile-based solvents provide the highest efficiencies [119, 139]. Apart from I^-/I_3^- couple, other redox systems have been proven successful. Among these successful couples include one-electron cobalt-based systems like polypyridyl cobalt (II/III) [53, 147] and cobalt (I/II) [148] coordination complexes, pseudohalides $\mathrm{SeCN^-/(SeCN)_2}$ and $SCN^-/(SCN)_2$, $\mathrm{SCN^-/(SCN)_3^-}$ [149], $\mathrm{Br^-/Br_3^-}$ [150], 1-ethyl-3-methylimidazolium selenocyanate $\mathrm{(EMISeCN)}, \mathrm{SeCN^-/(SeCN)_3^-}$, selenocyanate-based ionic liquid electrolytes provided an outstanding performance [151].

In addition, over 7% of device efficiency has been proven by using low-viscosity formulations like 1-ethyl-3-methylimidazolium thiocyanate, tricyanomethide, selenocyanate, and tetracyanoborate. With the exception of tetracyanoborate, all the other low-viscosity formulations are proven to be unstable under persistent thermal stress and light soaking [152]. Other organic based couples include 2,2, 6,6-tetramethyl-1-piperidinyloxy (TEMPO) [148] and N,N'-di-m-tolyl-N, N'-diphenylbenzidine (TPD) [153].

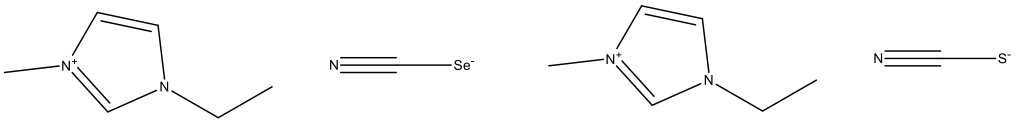

1-ethyl-3-methylimidazolium selenocyanate

1-ethyl-3-methylimidazolium thiocyanate

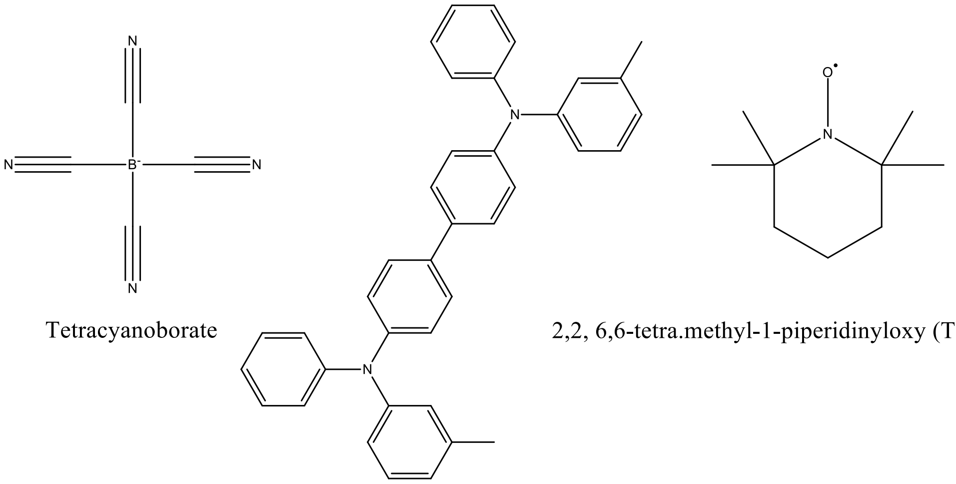

Tetracyanoborate

2,2, 6,6-tetra.methyl-1-piperidinyloxy (TEMPO)

N, N'-di-m-tolyl-N,N'-diphenylbenzidine (TPD)

Figure 3.8. Molecular Structure of Electrolytes (1)

The redox mediator in the dye-sensitized solar cell can be substituted by a solid-state organic-hole condctor such as 2, 2´,7, 7´-tetrakis-(N,N-di-p-methoxyphenylamine) 9,9´-spirobifluorene (spiro-OMeTAD) with almost 6% efficiency [23], poly (3,4-ethylenedioxythiophene) (PEDOT), poly(3-hexylthiophene) (P3HT) with 0.16% efficiency [154], polyaniline (PANI) with 0.10% efficiency [155], polypyrrole (PPy) with 0.10% efficiency [156], and poly[2-methoxy-5-(2-3thylhexyloxy)-1,4-phenylene-vinylene] (MEHPPV) with 0.51% efficiency [157]. In addition, the redox mediator in the dye-sensitized solar cell can be replaced by a solid-state inorganic p-type semiconductors like CuI [158] and $CuSCN$ [159]. The composition of the electrolyte can be further transformed with additives like 4-tert-butyl pyridine to improve the solar cell performance. Other additives include guanidinium thiocyanate (GuSCN) and Li cations. There is an increase in both current and voltage when guanidinium thiocyanate is added to liquid electrolytes due to a positive shift of the titanium dioxide/carbon-black composition (TiO_2/CB) and a reduction of charge recombination [160].

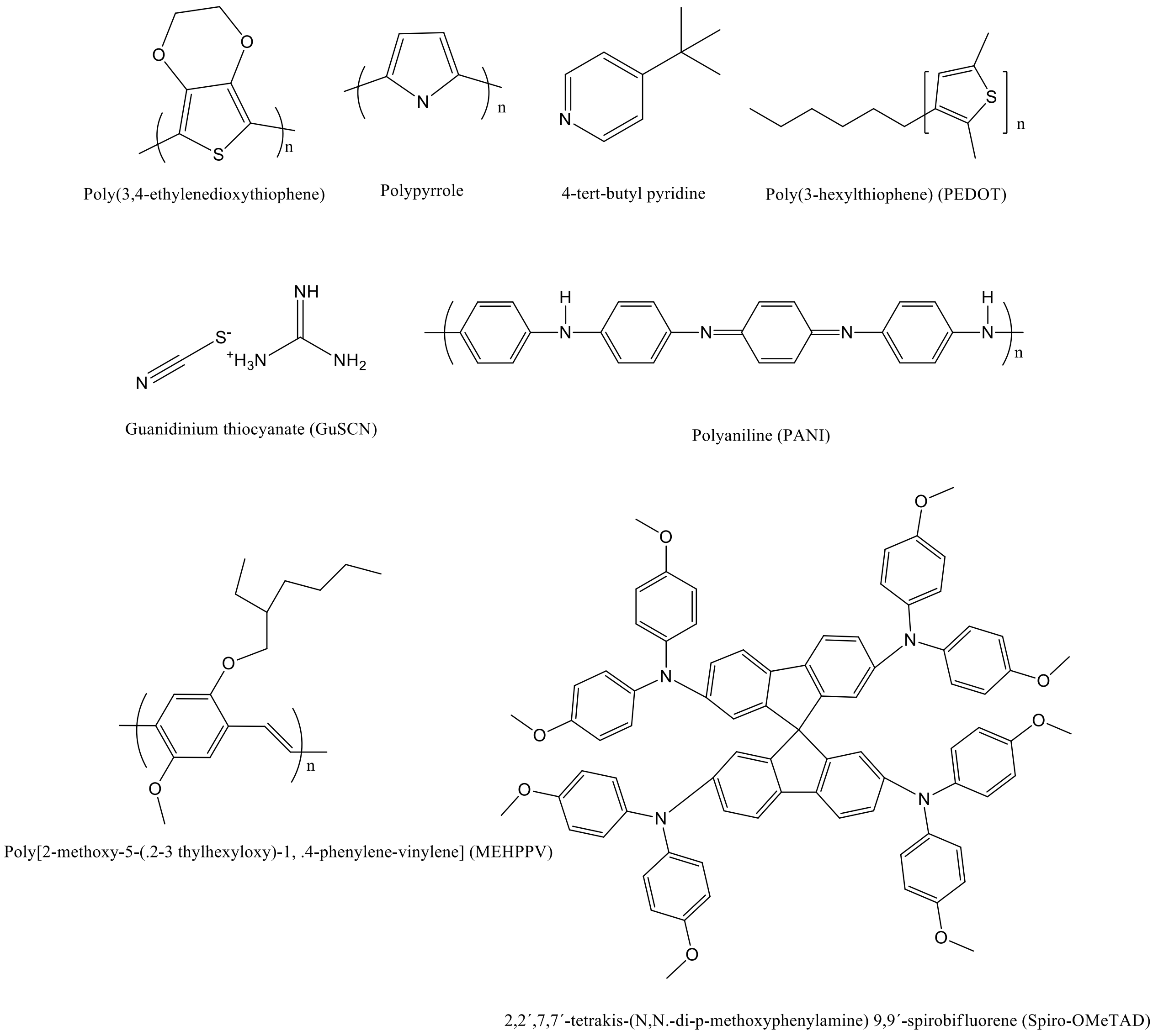

Poly(3,4-ethylenedioxythiophene)

Polypyrrole

4-tert-butyl pyridine

Poly(3-hexylthiophene) (PEDOT)

Guanidinium thiocyanate (GuSCN)

Polyaniline (PANI)

Poly[2-methoxy-5-(.2-3 thylhexyloxy)-1, .4-phenylene-vinylene] (MEHPPV)

2,2′,7,7′-tetrakis-(N,N.-di-p-methoxyphenylamine) 9,9′-spirobifluorene (Spiro-OMeTAD)

Figure 3.9. Molecular Structure of Electrolytes (2)

3.7 Working Principle

Dye-sensitised solar cell consists of five components namely: a mechanical support coated with transparent conducive oxides (TCO); the semiconductor film, typically titanium dioxide (TiO_2); a sensitizer adsorbed onto the surface of the semiconductor; an electrolyte containing a redox mediator; and a counter electrode that is able to regenerate the redox mediator like Platine [9]. Figure 3.10 shows a schematic representation of the dye-sensitized solar cell. Photoexcitation of the sensitizer is followed by electron injection into the conduction band of an oxide semiconductor film. The redox system regenerates the dye molecule, which is regenerated by itself at the counter-electrode by the electrons that passes through the load [103].

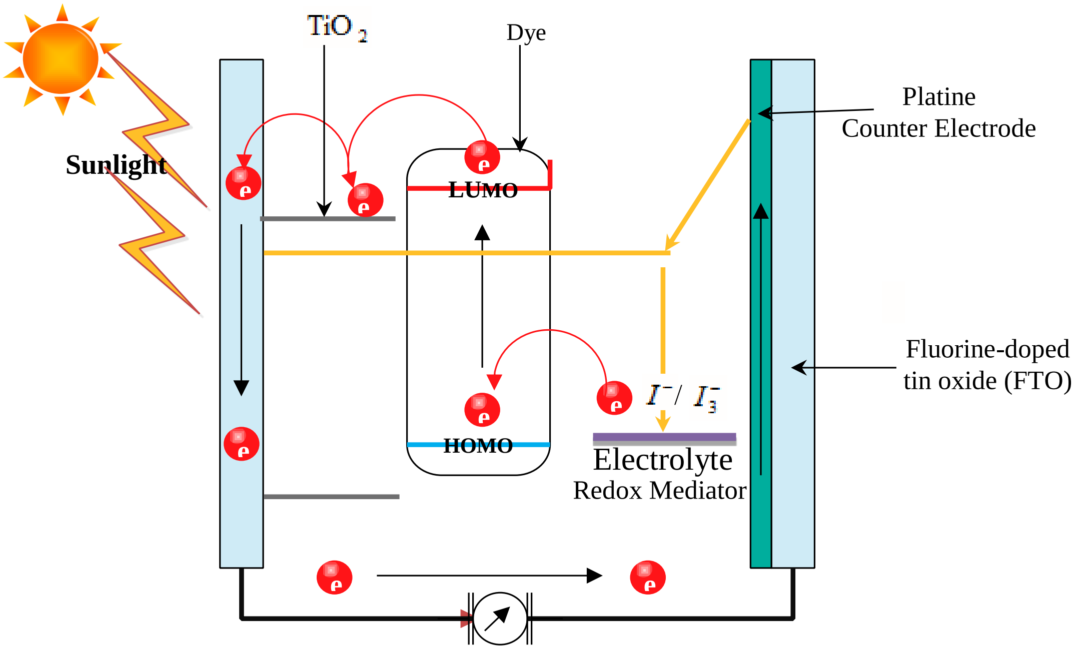

Figure 3.10. Schematic representation of the working DSSC

Figure 3.11 presents a schematic representation of the operation kinetics of a dye-sensitized solar cell. The order of the charge transfer processes responsible for the operation of a dye-sensitized solar cell is as follows [115, 161]:

1. The photosensitizer adsorbed on the semiconductor surface absorbs the incident photons and excites from the ground state (S) to the excited state (S^*), expressed in equation (3.1):
   $\mathrm{S + h\,v \rightarrow S^*}$ (3.1)

2. The excited electrons are injected into the conduction band of the semiconductor causing an oxidation of the sensitizer ($\mathrm{S^+}$), expressed in equation (3.2):
   $\mathrm{S^* \rightarrow S^+ + e^-_{CB}}$ (3.2)

3. The sensitizer that is oxidized ($\mathrm{S^+}$) is regenerated as a result of accepting electrons from the iodide ion ($\mathrm{I^-}$), expressed in equation (3.3):
   $\mathrm{S^+ + \frac{3}{2}I^- \rightarrow \frac{1}{2}I^-_3 + S}$ (3.3)

4. At this point, the triiodide redox mediator ($\mathrm{I^-_3}$) spreads to the counter electrode and is reduced to iodide ($\mathrm{I^-}$), expressed in equation (3.4):
   $\mathrm{I^-_3 + 2e^-_{CB} \rightarrow 3I^-}$ (3.4)

   It is noteworthy that the electron loss pathway must be considered alongside the forward electron transfer and the ionic transport processes, expressed in equations (3.5-3.7):

5. The decay of the dye from the excited state to the ground state, expressed in equations (3.5):
   $\mathrm{S^* \rightarrow S}$ (3.5)

6. The recombination of the injected electrons with the dye cations, expressed in equations (3.6):
   $\mathrm{S^+ + e^-_{CB} \rightarrow S}$ (3.6)

7. The recombination of the injected electrons with the triiodide redox mediator (I_3^-), expressed in equations (3.7):

$$I_3^- + 2e_{CB}^- \rightarrow 3I^- \tag{3.7}$$

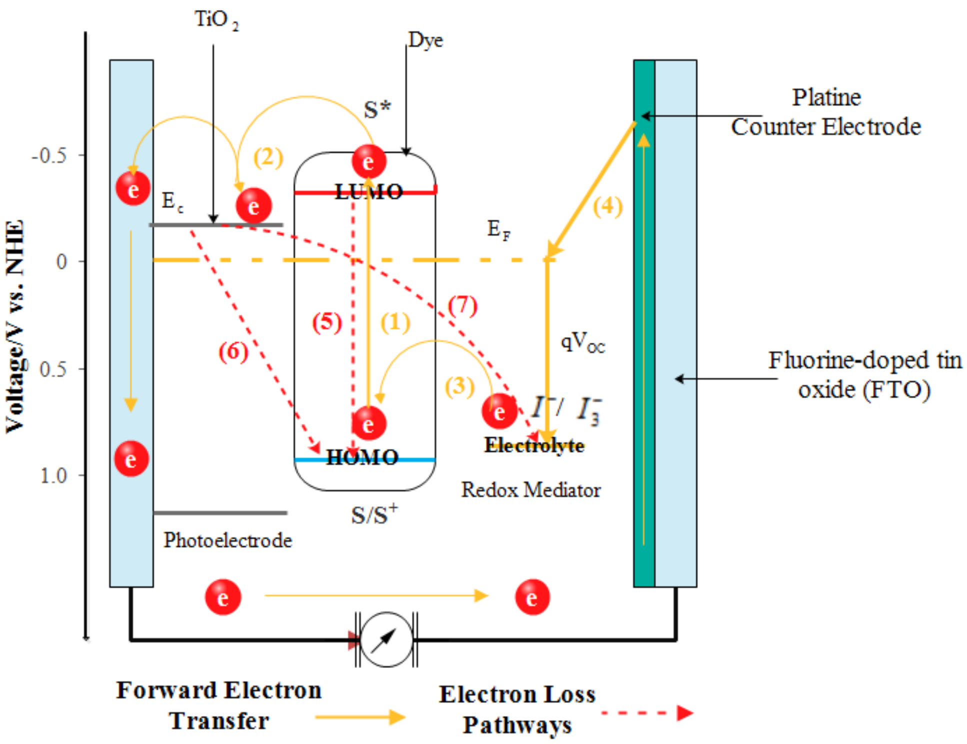

Figure 3.11. Schematic Representation of the Operation Kinetics of a DSSC

3.8 Parameters of a Solar Cell

The photovoltaic device employs the photoelectric effect to convert the incidence rays of sunlight into electrical energy. The ability of the PV device to produce voltage over an external load and current through the load at the same time is a necessity to generate electrical power under illumination. The performance of the dye-sensitized solar cell is dependent on the open circuit photovoltage (V_{oc}), the short circuit photocurrent (J_{sc}), the fill factor (FF) and the photo conversion efficiency (η). One of the fundamental measurements of dye-sensitized solar cell performance is the incident photon to current conversion efficiency (IPCE). The incident photon to current conversion efficiency describes the efficient conversion of the light of a specified wavelength to useful current (i.e. electrons-out/photons-in). The incident photon to current conversion efficiency can be mathematically represented as shown in equation (3.8) [119]:

$$IPCE(\%) = \frac{1240 \times J_{sc}}{\lambda \times \Phi_{in}} \times 100 \tag{3.8}$$

Where J_{sc} is the short-circuit current density, λ is the wavelength of incidence light, and Φ_{in} is the intensity of the incidence light. The factor that determines the incident photon to current conversion efficiency can be mathematically represented as shown in equation (3.9):

$$IPCE = LHE \times \Phi_{inj} \times \eta_{reg} \times \eta_{cc} \tag{3.9}$$

Where LHE is the light harvesting efficiency, Φ_{inj} is the quantum yield of the charge injected, η_{reg} is the dye regenerated, and η_{cc} is the charge collected efficiency.

3.8.1 Open Circuit Photovoltage

The open circuit photovoltage (V_{oc}) is maximum voltage generated by the solar cell when connected to an infinite resistance (i.e. when there is no flow of current). It is well defined as the potential difference between the two terminals (i.e. the conduction band of the titanium dioxide and the redox potential of the electrolyte) in the solar cell under illumination once the circuit is open. The process depends on the dark current level and the Fermi level of the semiconductor [115, 119].

3.8.2 Short Circuit Photocurrent

The short circuit photocurrent (J_{sc}) is the maximum current (i.e. the photocurrent per unit area) when an illuminated cell or the electrodes are short-circuited. The short circuit photocurrent is dependent on some factors which include the injection efficiency, the light absorption, the light intensity, and the regeneration of the oxidized dye [115, 119]. Figure 3.12 show a schematic representation of a typical Current-Voltage characteristic of a standard solar cell. The typical current-voltage characteristic of a standard solar cell illustrates the current-voltage characteristics of a solar cell under illumination with an external load going from a zero load (i.e. an open-circuit (V_{oc}) situation) to an infinite load (i.e. a short-circuit (J_{sc}) situation).

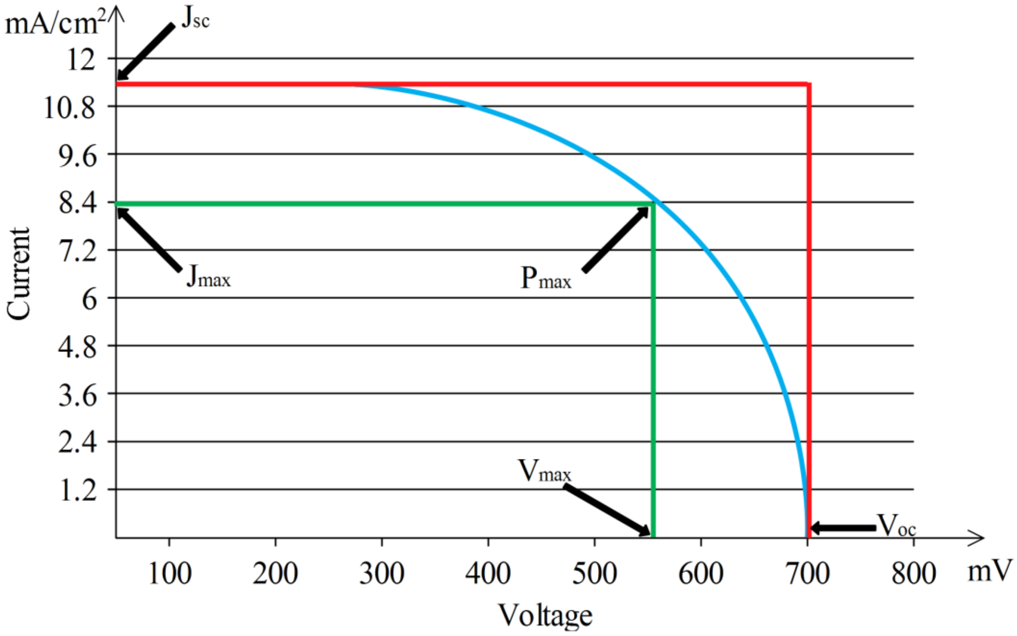

Figure 3.12. Typical Current-Voltage Characteristic of a Standard Solar Cell

3.8.3 Fill Factor

The fill factor (FF) measures the cell quality and is well defined as the relation of the maximum power output ($J_{max} \times V_{max}$) to the product of the short-circuit photocurrent (J_{sc}) and the open-circuit photovoltage (V_{oc}). The fill factor depends on the inner resistance thus; a higher inner resistance results in a low fill factor and the overall efficiency decreases [40, 115, 119]. It can be mathematically represented as equation (3.10):

$$FF = \frac{J_{max} \times V_{max}}{J_{sc} \times V_{oc}} \tag{3.10}$$

3.8.4 Photo Conversion Efficiency

The photo conversion efficiency (η) is the most essential parameter resulting from the classical current-voltage characteristic of a standard cell. The photo conversion efficiency (η) is well defined as the relation of the maximum output (P_{max}) of the solar cell to the power density of the incidence light in the cell. It is mathematically represented by the measured open-circuit photovoltage (V_{oc}), the short-circuit photocurrent (J_{sc}) photocurrent density, the fill factor (FF) and the intensity of the incidence light (P_{in}) in the cell as shown in equation (3.11):

$$\eta = \frac{P_{max}}{P_{in}} = \frac{J_{sc} \times V_{oc} \times FF}{W_{in}} \tag{3.11}$$

Where W_{in} is the optical incidence power density equals to 100 mW/cm^2 under a standard AM 1.5g condition (see Figure 2.3).

3.9 Perylene Diimides

Perylene-3,4,9,10-tetracarboxylic acid (Figure 3.13) diimide derivatives [162-166], popularly called the perylene diimides (PDIs) have been studied comprehensively as soluble dyes, colorants in the industry and insoluble pigments [167]. PDIs represents an outstanding class of organic compounds that has been utilized in an extensive collection of high industrial applications such as field effect transistors, logic gates, organic solar cells, sensors, organic light-emitting diodes, photosensitizers and optical switches, but not limited to them [168]. Due to its versatility and fascinating properties like exceptional electron acceptor, fictionalization, high molar extinction coefficient in visible region and high fluorescence quantum yields, PDIs are used as building blocks for many applications [169].

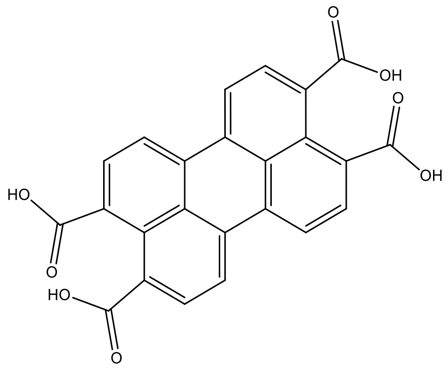

Figure 3.13. Molecular Structure of Perylene-3,4,9,10-tetracarboxylic acid

Figure 3.14 shows the functionalized perylene core positions. There are twelve functionalized positions in the perylene core namely; 3,4,9,10 (known as *peri*), 2,5,8,11 (known as *ortho*) and 1,6,7,12 (known as *bay*). Figure 3.15 shows the developmental stages of perylene imides within the past centuries. Three generational stages of perylene imides exist as shown in Figure 3.15. The first generation of the perylene imides (i.e. 3,4,9,10-diimides substitutions) was discovered and developed in the 1910s. The second generation of the perylene imides (i.e. additional or exclusive 1,6,7,12-decoration and asymmetric perylene monoimides or monoanhydride) was discovered and developed extensively in the 1970-1980s to improve the orbital and colour tuning, and the solubility for solution-fabricated devices (i.e. bulk heterojunction solar cell). In terms of copolymers, perylene diimides with halogenated bay positions are the preferred candidate capable of merging with other compounds like oligothiophenes to form donor-acceptor copolymers employed in single material solar cells.

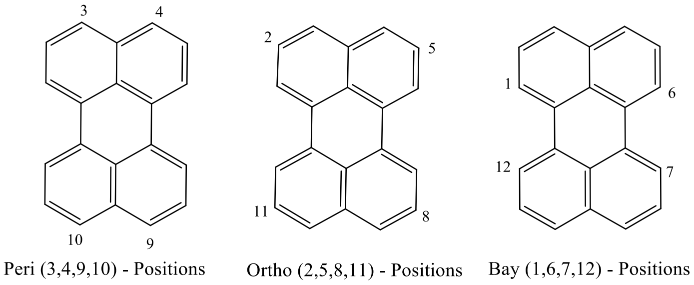

Figure 3.14. Functionalized Positions of Perylene Core

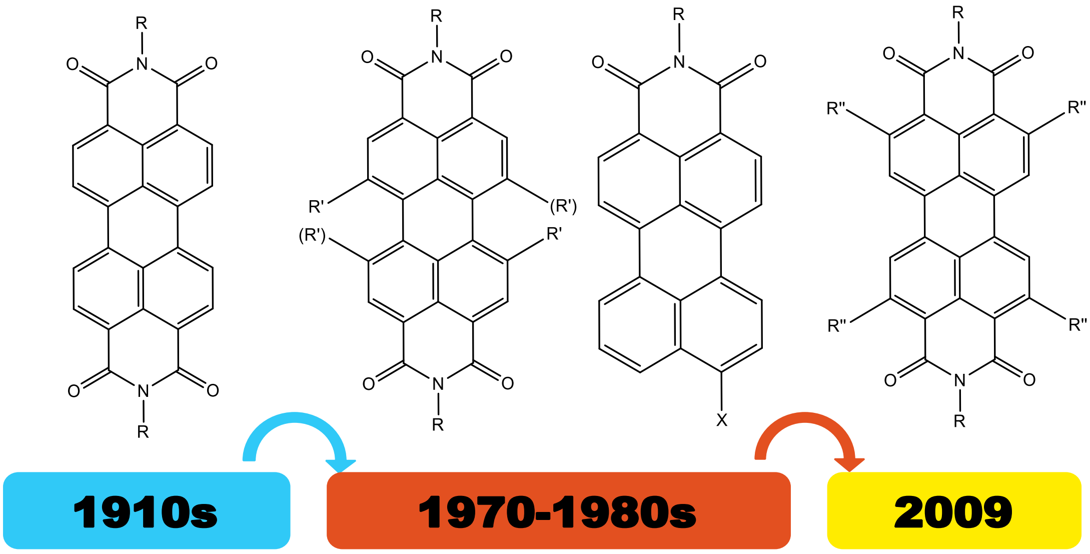

Figure 3.15. Developmental Stages of Perylene Imides

Böhm, Arms [170] discovered bay-site-bromination of Perylene-3,4,9,10-tetracarboxylic dianhyride (PTCDA) in the early nineties to yield 1,7-dibromoperylene-3,4,9,10-tetracarboxylic. In 2004, Würthner, Stepanenko [171] reconsidered the procedure adopted by Böhm, Arms [170] and discovered that the dibromination reaction was not regioselective, but rather produces a regioisomeric mixture of 1,7- and 1,6- dibromoperylene dianhyride as well as tribrominated isomers. As a result, the subsequent imidization of cyclohexyl amine yielded a regioisomeric mixture of 1,7-dibromoperylene diimides and 1,6-dibromoperylene diimides. The successful separation and characterization of regioisomerically pure N, N’-1,7-dicyclohexyl-1,7-dibromoperylene diimides from the regioisomeric mixture was done through a mechanism called repetitive recrystallization, which has being used till date [172, 173]. Significantly, bay-region substitutions are the most decorative synthetic approach to fine-tune the optoelectronic properties [167, 174]. The third generation of the perylene imides (i.e. 2,5,8,11-diimides substitutions) was discovered and developed in the 1990-todate (see Figure 3.15) [99].

3.9.1 Synthesis of Perylene Imides

In order to tune the electrochemical and optical properties of perylene imides, there is the need to attach the perylene core with different substituents via various synthetic methods presented in Figure 3.16 to Figure 3.20. A number of organic reactions which include saponification, metal-catalyzed coupling, imidization, nucleophilic substitution and cyclo-dehydrogenation, have been used in the chemistry of perylene imides since the inception of the perylene imides in solar cell application [167, 175, 176].

Figure 3.16 presents the synthesis of perylene imides in the peri-position. The synthesis of perylene imides begins with the use of perylene dianhydride (**A1**) as a starting material. A simple imidization reaction to **A1** using aromatic or aliphatic amines leads to a soluble or insoluble perylene dye (perylene diimide) **A2**. The introduction of aryl or alkyl substituents is essential to achieve a soluble perylene diimide [177]. The functionalization of **A1** with aromatic diamines using adjacent amino groups is able to tune the absorption behaviour of the perylene diimide to form **A3** (perylene diamindine) [99, 167, 175, 176].

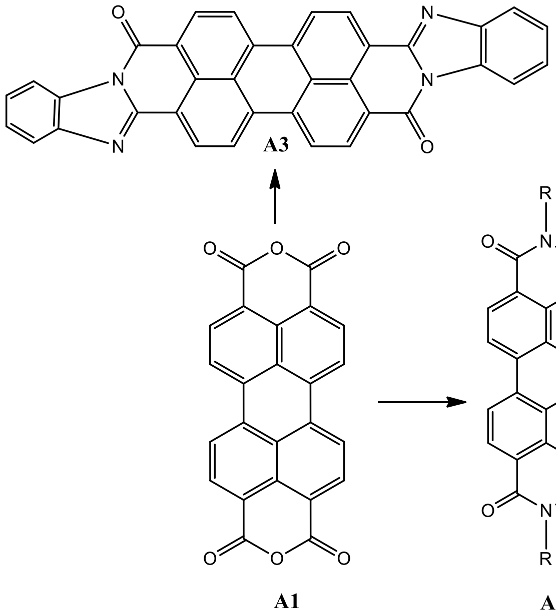

Figure 3.16. Synthesis of Perylene Imides in the Peri-Position

Figure 3.17 presents the synthesis of perylene imides in the ortho-position. Using arylboranates/alkenes as a starting material in the perylene diimide (**B2**) with a subsequent introduction of aryl/alkyl substituents to the ortho-position forms perylene **B4** using a regioselective reaction by ruthenium catalysis [178]. Perylene **B4** has both higher solid-state fluorescence and solubility than bay-substituted perylene diimide (**C5**) while perylene **B3** (tetraboronated perylene diimides) provides three choices (**B5**, **B6** and **B7**) of functionalizing the perylene diimide in a copper (II) catalyzed reaction conditions. A subsequent functionalization of **B5** using amination leads to perylene **B8** [179].

Figure 3.18 presents the synthesis of perylene imides in the bay position. Perylene dianhydride (**C1**) is halogenated with amines under acid coupling to synthesize 1, 6, 7, 12-tetrachloro dianhydride or 1, 6, (7)-dibromoperylene dianhydride (**C2**, **C3**) which is currently the essential building block in perylene chemistry [180]. Nucleophilic substitution and metal-catalyzed reactions can be performed after the bay-halogenation of the perylene diimides [167]. In order to improve the solubility of perylene diimides, the phenol is reacted with a base in a process known as phenoxylation.

The tetrachloro-perylene diimide (**C4**) through a one-step palladium-catalyzed Migita-Kosugi-Stille coupling reaction forms perylene diimides (**C6**) with an expanded-bay region by two-Sulphur bridges forming a strong hypsochromic shift in absorption [99]. In the same vein, using dibromo-perylene diimides (**C7**) as precursors, the bay-region can be expanded with coronene diimides (i.e. n = 0), dibenzocoronene diimides (i.e. n = 1), and dinaphtocoronene diimides (i.e. n = 2) forms perylene diimide (**C9**) [181]. The pathway of the bromo-substituted-perylene diimides (**C7**) is by nucleophilic substitution using phenol (phenoxylation) [182], potassium fluoride (fluorination) [183], cyano copper (I) (cyanation) [184], and pyrrolidine (amination) [185]. Perylene diimides (**C8**) are under investigations in the field of organic solar cells and organic field effect transistors [167].

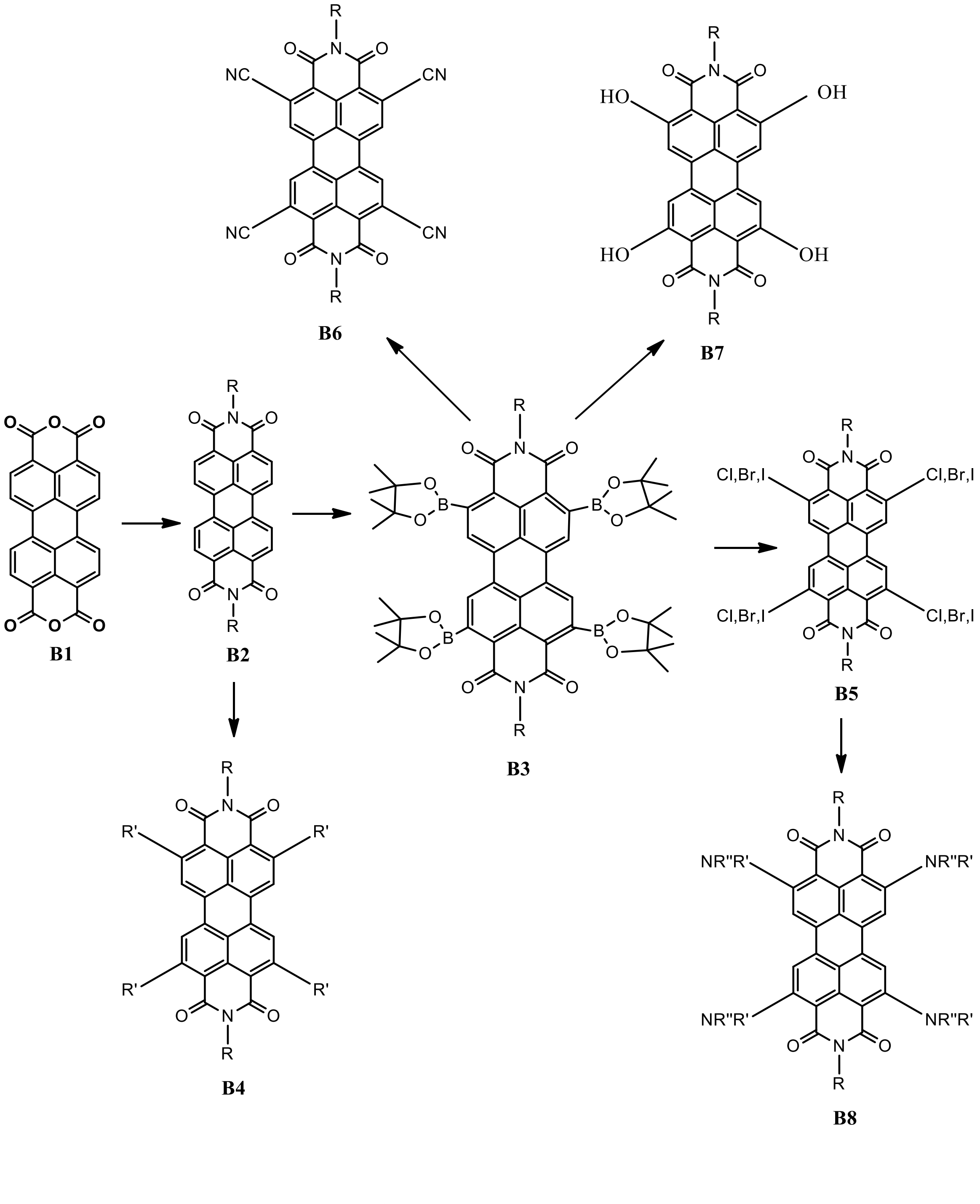

Figure 3.17. Synthesis of Perylene Imides in the Ortho-Position

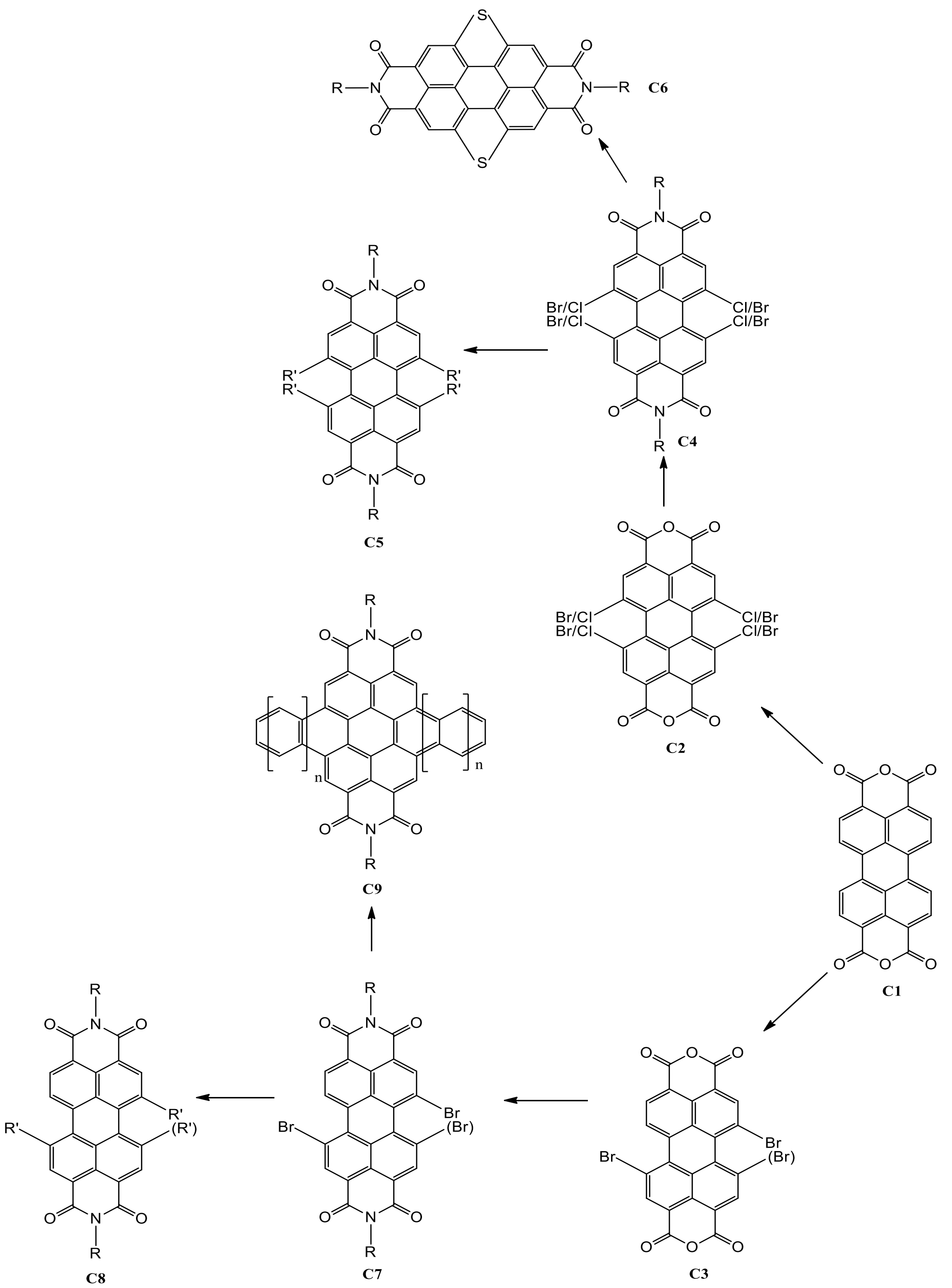

Figure 3.18. Synthesis of Perylene Imides in the Bay-Position

Figure 3.19 presents the synthesis of perylene imides in the bay+ortho-position. The bay-ortho positions of the perylene diimides (**D2**) can be functionalized to form 1,2,5,6.7,8,11,12-octacholoro- perylene diimides (**D3**) used as an organic field effect transistors (OFET) material application [186].

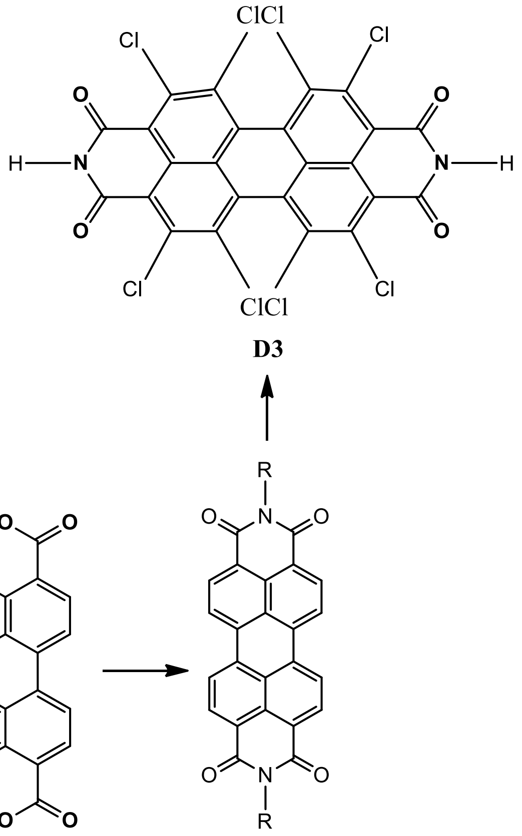

D3

D1

D2

Figure 3.19. Synthesis of Perylene Imides in the Bay + Ortho-Position

Figure 3.20 presents the synthesis of perylene imides in the bay+peri-position. The asymmetric perylene monoimides (**E3**) can be monobrominated in acetic acid as the reaction solvent to form mono-bromo-perylene monomides (**E4**) or tribrominated in chloroform as the reaction solvent to form tri-bromo-perylene monomides (**E5**). Mono-bromo-perylene monomides (**E4**) can be fuctionalized by palladium-catalyzed reaction (i.e. Buchwald-Hartwig amination/Suzuki C-C coupling). Terrylene diimides (**E7** i.e. m = 1) are formed when the mono-bromo-perylene monoimides (**E4**) is reacted with four functionalized naphthalene monoimides followed by a treatment with a base (for example, Potassium carbonate for cyclodehydrogenation). The tri-bromo perylene monoimides (**E5**) allows for the decoration of the 1,6-positions before the peri (9)-position leading to perylene monoimide (**E8**). It is noteworthy that the 1,6-position is essential for fine-adjustment while the peri (9)-position is necessary for changing the optical and electronic properties of the perylene monoimides [99, 187, 188].

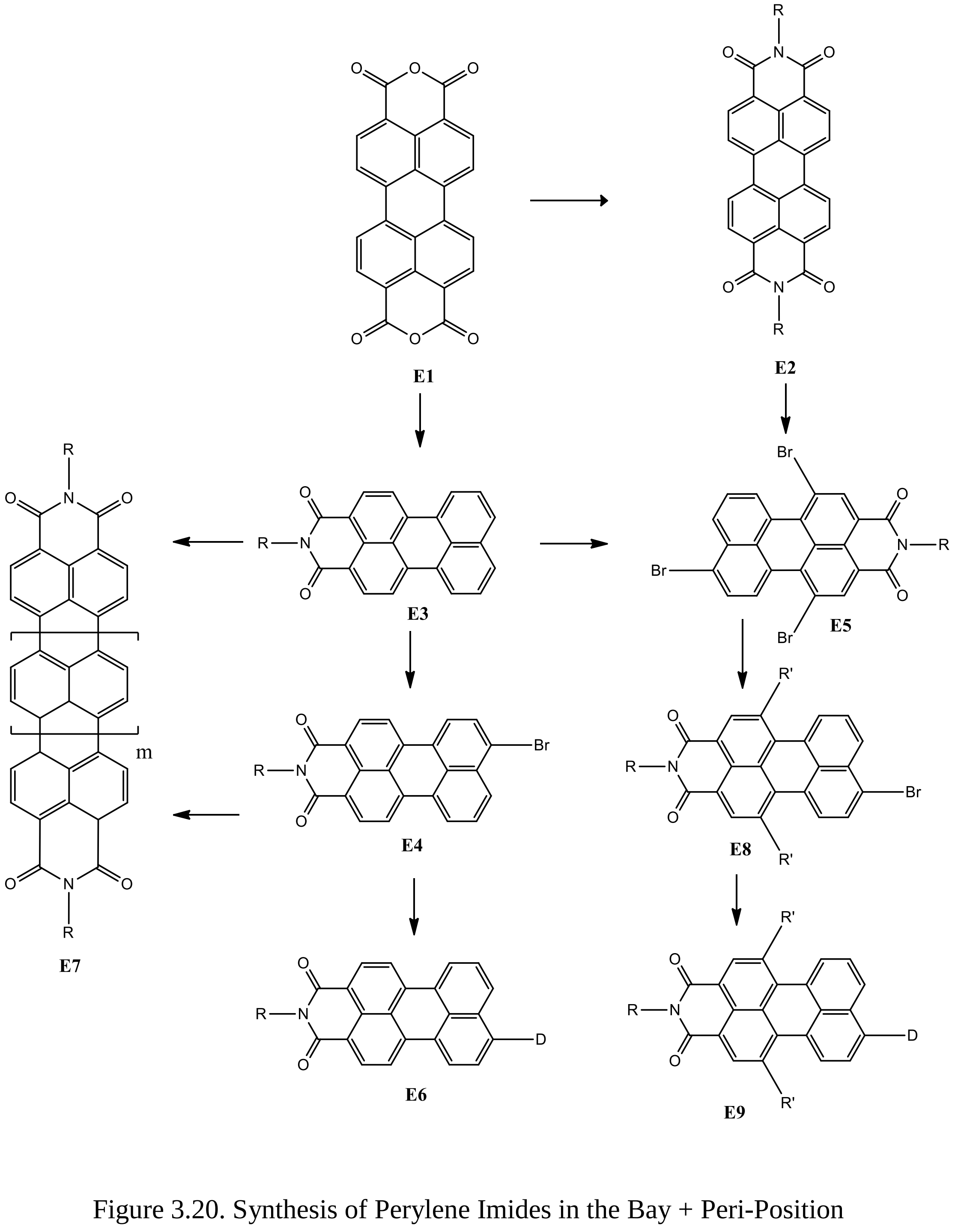

Figure 3.20. Synthesis of Perylene Imides in the Bay + Peri-Position

3.9.2 Perylene Diimides Derivatives for DSSC

The emergence of perylene-3,4,9,10-tetracarboxylic dianhydride in organic compounds have played a versatile role in different technological applications that include electro photographic devices, organic solar cells, optical power limiters, sensors, dye lasers, organic field effect transistors (OFET), fluorescent solar collectors, optical switches, logic gates, photosensitizers, organic light emitting diodes, etc. [173]. The first perylene-3,4,9,10-tetracarboxylic dianhydride was discovered in 1913 by Kardos in the industrial sector as colorants (i.e. as pigments and dyes) due to their outstanding thermal, chemical, photo and weather stability [176, 189]. In 1913, the first industry pigment based on perylene diimides called Pigment Red-179 (Figure 3.21) was discovered and used as a pigment in industrial applications resulting from the work of Harmon Colours that describes the conversion of vat dyes to pigments.

Due to its versatility, perylene-3,4,9,10-tetracarboxylic dianhydride derivatives are currently used in the automobile and manufacturing industry for high-grade industrial paints and carpet fiber manufacturing [176]. Ab initio, the Photostability and the high quantum yield of perylene-3,4,9,10-tetracarboxylic dianhydride derivatives were hidden till 1959 and was mostly centered on industrial pigment manufacturing due to its poor solubility in organic solvents [190]. Nevertheless, there has been an enormous discovery of the perylene-3,4,9,10-tetracarboxylic dianhydride applications in electronics and organic photovoltaics [190].

Perylene-3,4,9,10-tetracarboxylic dianhydride, aka perylene diimides, has been used as sensitizers in dye-sensitized solar cell applications due to its ability to be functionalized with an anhydride or carboxylic groups, which functions as a fix position for attachment onto the inorganic surfaces of the semiconductor. The perylene imides allow the measurements of charge injection rate by facilitating time correlated emission experiments [99]. Figure 3.21 presents the molecular structure of the three most essential industry pigments based on perylene diimides. Perylene diimides have different colours such as red, violet and shades of black [191]. Perylene diimides exhibit outstanding migration stability in plastics, chemically inert, easy-over-coating in paints and higher thermal stability [169, 176]. From 1950, numerous perylene diimide derivative like Pigment Red-179, Pigment Red-149 and Pigment Red-178 (Figure 3.21) have been used in manufacturing scale production and applications [176].

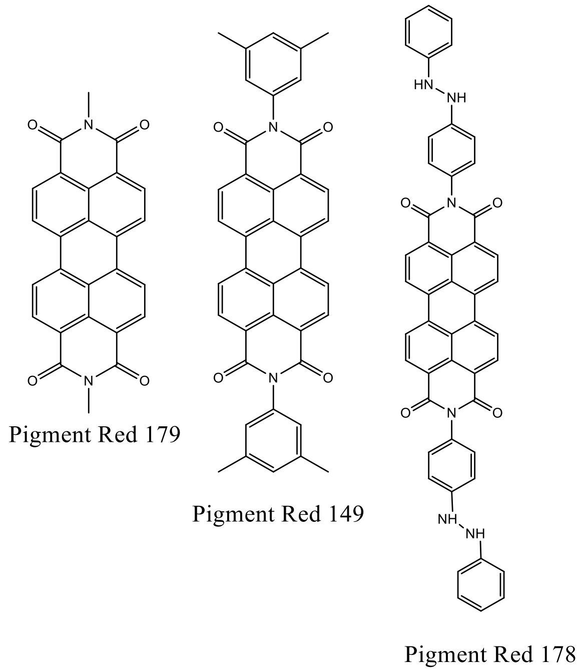

Pigment Red 179

Pigment Red 149

Pigment Red 178

Figure 3.21. Molecular Structure of Industry Pigments based on PDI

Figure 3.22 shows the molecular structure of PDI derivatives for DSSC applications. Perylene imides with carboxylic acid groups to fix onto tin (IV) oxide (SnO_2) in Figure 3.22 (**a**) and (**b**) were the first dye semiconductor coordination employed as sensitizers in the first reported photovoltaic application [150]. A nanoporous tin (IV) oxide film on a fluorine-doped tin oxide glass with a thickness of 2.5 μm containing the dye and a platinum-coated fluorine-doped tin oxide glass substrate was revealed. A DSSC device containing the sensitizer in Figure 3.22 (**a**) could attain a maximum incident photon-to-current efficiency of almost 30% at a wavelength region between 458 and 488 nm and a total power conversion efficiency of almost 0.89%. Even though the power conversion efficiency of 0.89% is lower in this era of technological advancement nonetheless, it was proven in that era, the potentials of perylene diimide derivatives in DSSC applications [99, 150].

A continual research in perylene diimide derivatives led to the inception of sensitizers reported in Figure 3.22 (**b**) and (**c**) which were examples of the reported perylene diimide derivatives in titanium dioxide nanocrystalline films [192]. As reported, a bromine-doped titanium dioxide nanocrystalline films might improve the maximum incident photon-to-current efficiency of the sensitizer in Figure 3.22 (**c**) to almost 40% in a wavelength region between 440 and 530 nm. The advancement of research in perylene diimide derivatives led to the inception of sensitizers reported in Figure 3.22 (**d**), (**e**), (**f**), (**g**) and (**h**) with anhydride groups as anchor were synthesized [193]. Evidence from the reported sensitizers in Figure 3.22 (**d**), (**e**), (**f**), (**g**) and (**h**) shows that the photovoltaic performance in DSSC is influenced by the variations of the imide groups in perylene monoimides monoanhydride. A scrutiny of the sensitizer reported in Figure 3.22 (**d**) with a 1-pentyl-hexyl at the amide position showed the highest efficiency of 1.61% under air mass (AM) 1.5 solar light compared to the sensitizers in Figure 3.22 (**e**), (**f**), (**g**) and (**h**) [99]. Notwithstanding, the power conversion efficiencies of the sensitizers reported in Figure 3.22 (**d**), (**e**), (**f**), (**g**) and (**h**) are too low for industrial applications. Obviously, these low power conversion efficiencies may be due to lack of intermolecular push-pull effect in the sensitizers in Figure 3.22 (**d**), (**e**), (**f**), (**g**) and (**h**) since they are all deficient in donor groups. The aforementioned sensitizers are limited with ordinary chromophore anchor group that limits the efficiency of the dye-conduction band electron transfer of the metal oxide [99].

Later on, donor groups were introduced in subsequent research in perylene diimide derivatives as showed in Figure 3.22 (**i**), (**j**), (**k**) and (**l**) [194]. The 1,6-Pyrrolidinone perylene monoimides monoanhydride derivatives in Figure 3.22 (**i**), (**j**), (**k**) and (**l**) are thought to exhibit certain advantages. These advantages include; improved light harvesting efficiency in the red-to-near infrared region and a more improved exothermic electron injection from the excited singlet state to the conduction band of titanium dioxide electrode. The aforementioned advantages are due to the strong ability of the pyrrolidinone groups that shift the first oxidation and the first reduction potentials in the positive direction. In addition, the bay-substituents of the 1,6-pyrrolidinone perylene monoimides monoanhydride derivatives in Figure 3.22 (**i**), (**j**), (**k**) and (**l**) suppress the dye aggregation on the surface of the titanium dioxide leading to a delayed intermolecular charge recombination. The performance of perylene monoimides monoanhydride derivatives in Figure 3.22 (**i**) and (**j**) outweighed the perylene diimide derivatives in Figure 3.22 (**k**) and (**l**). The reason has been that the phenylcarboxy acid groups in Figure 3.22 (**k**) and (**l**) which serves as anchors keep the chromophores at a far distance from the surface of the titanium dioxide, a condition that is unfavorable for the charge transport mechanism [99].

Subsequently, the same concept was applied to examine how the nature of electron donating substituents (phenoxy/piperidine) affect the perylene core, the effect of the anchoring group positions, and how the existence of a fused benzimidazole moiety affect the performance of DSSCs [195]. It was reported that DSSCs with sensitizers in Figure 3.22 (**m**), (**n**) and (**o**) got efficiencies between 0.2% and 2.3%. Evidence from the study shows that both the phenoxy and piperidine groups exhibit the same behaviour at the bay position of the perylene core, however, the phenoxy group at the bay-position has a lower propensity to aggregate thus, exhibits a slightly higher performance. In addition, the position of the anchoring groups can influence the electron injection efficiency and a bathochromic shift of the absorption spectrum occurs as the sensitizer is functionalized with benzimidazole moiety [99].

Another study presented a perylene monoimides monoanhydride derivative in Figure 3.22 (**p**) with a piperidine-substituent anchoring through the anhydride [196]. The complexity of the sensitizer in Figure 3.22 (**p**) makes it able to selectively bind lithium ions in DSSCs thereby producing higher voltages but lower photocurrents. The later results in a shift of the titanium dioxide conduction band due to the formed dipole at the surface of the semiconductor resulting from the complexation of lithium with aza crown ether [99].

The absorption properties of perylene monoimides monoanhydride moiety and ruthenium complexes were improved by incorporating them into the ligand in Figure 3.22 (**q**) [197]. Notwithstanding, the strong electron withdrawing nature of the amide groups weakens the intramolecular charge transfer thus, resulting in a low efficiency (3.08%) of the dye in DSSCs. In summary, due to the outstanding light-harvesting abilities of perylene diimide derivatives, they have a good potential for dye-sensitized solar cell applications.

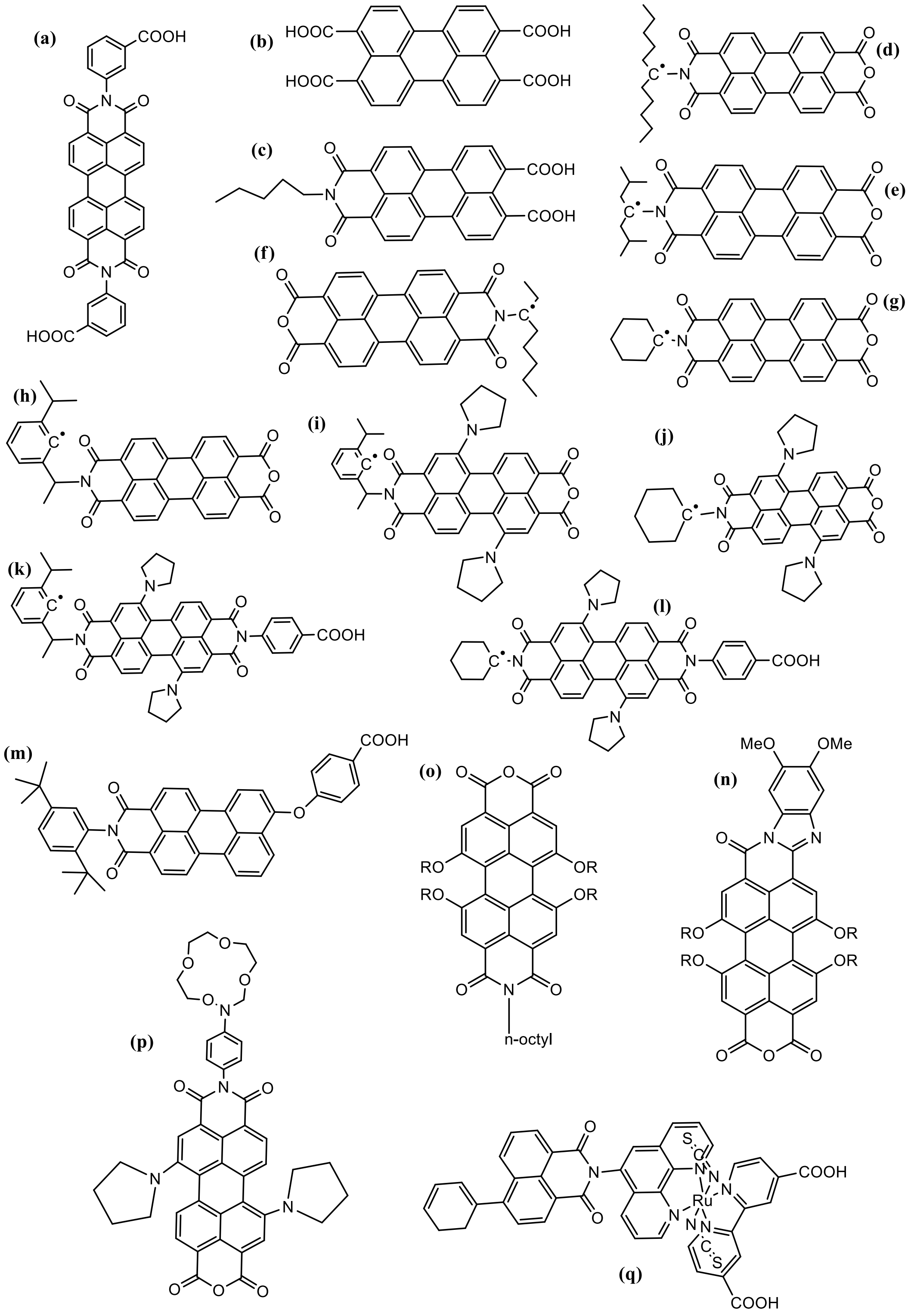

Figure 3.22. Molecular Structure of Perylene Diimide Derivatives for DSSC

3.9.3 Preparation of Perylene Diimides Derivatives

Perylene-3,4,9,10-tetracarboxylic dianhydride is the principal starting material for the synthesis of perylene diimide derivatives. High yields of perylene diimide derivatives are achieved when there is a condensation reaction between the perylene-3,4,9,10-tetracarboxylic dianhydride and an aniline/alkyl amine. Scheme 1.1 and Scheme 1.2 show the imide substituent positions of the perylene diimide preparations. A large manufacturing scale of the synthesis of perylene-3,4,9,10-tetracarboxylic dianhydride begins with the air oxidation of acenaphthene to produce a naphthalic anhydride, with a subsequent treatment with ammonia to produce the 1,8-naphthalene dicarboxylic acid imide. In order to obtain perylene-3,4,9,10-tetracarboxylic diimide, the 1,8-naphthalene dicarboxylic acid imide is fused with caustic alkali (i.e. potassium hydride) between a temperature of 190-220°C with a subsequent oxidation of the molten reaction mixture by air. The hydrolysis of the perylene-3,4,9,10-tetracarboxylic diimide solid with a concentrated sulphuric acid at a temperature of about 220°C produces the perylene-3,4,9,10-tetracarboxylic dianhydride synthesis. At this juncture, the reaction between the perylene-3,4,9,10-tetracarboxylic dianhydride and different aromatic aniline/aliphatic amines leads high isolated yields of insoluble and symmetrical organic perylene diimides with high melting points (see Scheme 1.1) [198].

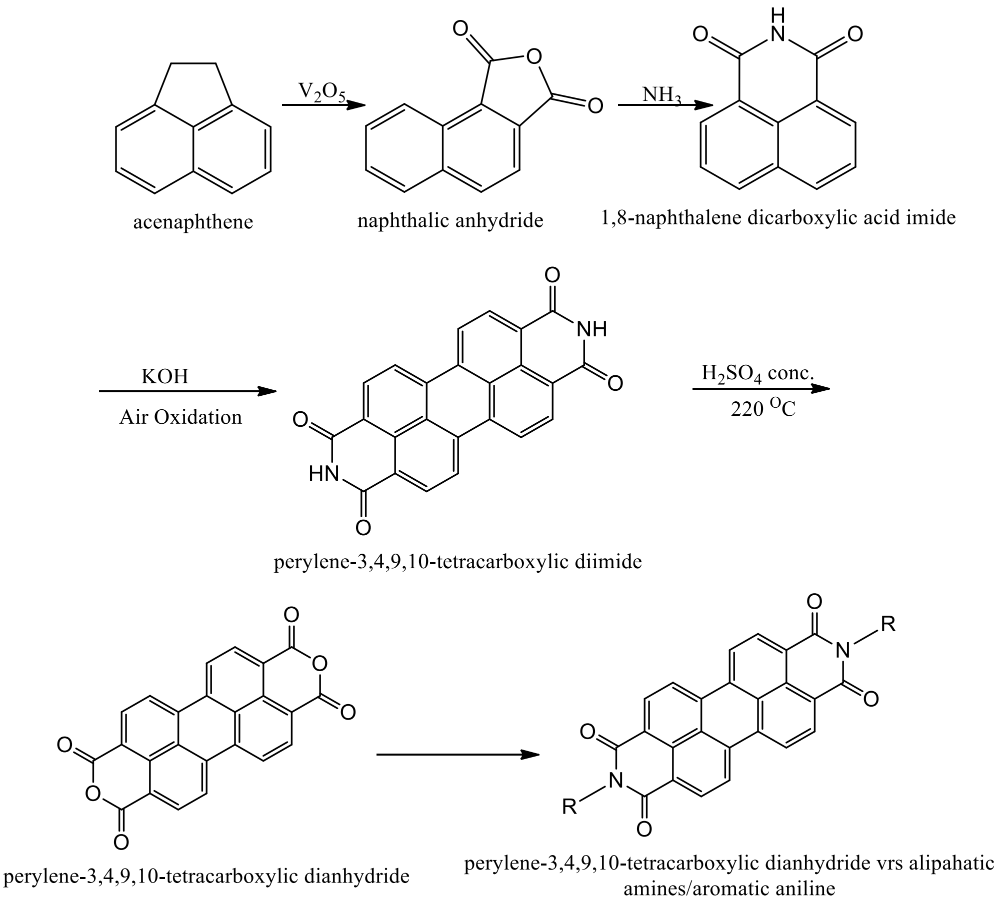

Scheme 1.1. Imide Substituent Positions of PDI Preparations (1)

From Scheme 1.2, the attachment of the imide positions with substituents makes it easy to obtain a soluble perylene diimide dye. The condensation reaction of the perylene-3,4,9,10-tetracarboxylic dianhydride with primary amines and aromatic aniline in a high boiling point solvent like quinoline/imidazole with a boiling point above 160°C and a subsequent addition of anhydrous zinc acetate [$Zn(OAc)_2$] as a catalyst is the commonly used procedure in synthesizing symmetrical perylene diimide derivatives. With a simple purification procedure, the isolated yield of the aforementioned reaction normally approaches 95% [177]. Another way of synthesising symmetrical perylene diimide is treating the perylene-3,4,9,10-tetracarboxylic dianhydride with a reactive amine in hot alcohol like *n*-butanol, a carboxylic acid like propionic acid and acetic acid or by mixing water and alcohol with the isolated yields above 90%. In addition, a condensation reaction of the perylene-

3,4,9,10-tetracarboxylic dianhydride with the *o*-phenylenediamine derivatives lead to the achievement of perylene benzoimidazole derivatives. A subsequent benzoimidazole derivatives synthesis produces two regioisomers however, employing purification methods like recrystallization and column chromatography is very thought-provoking to separate the two regioisomers [198].

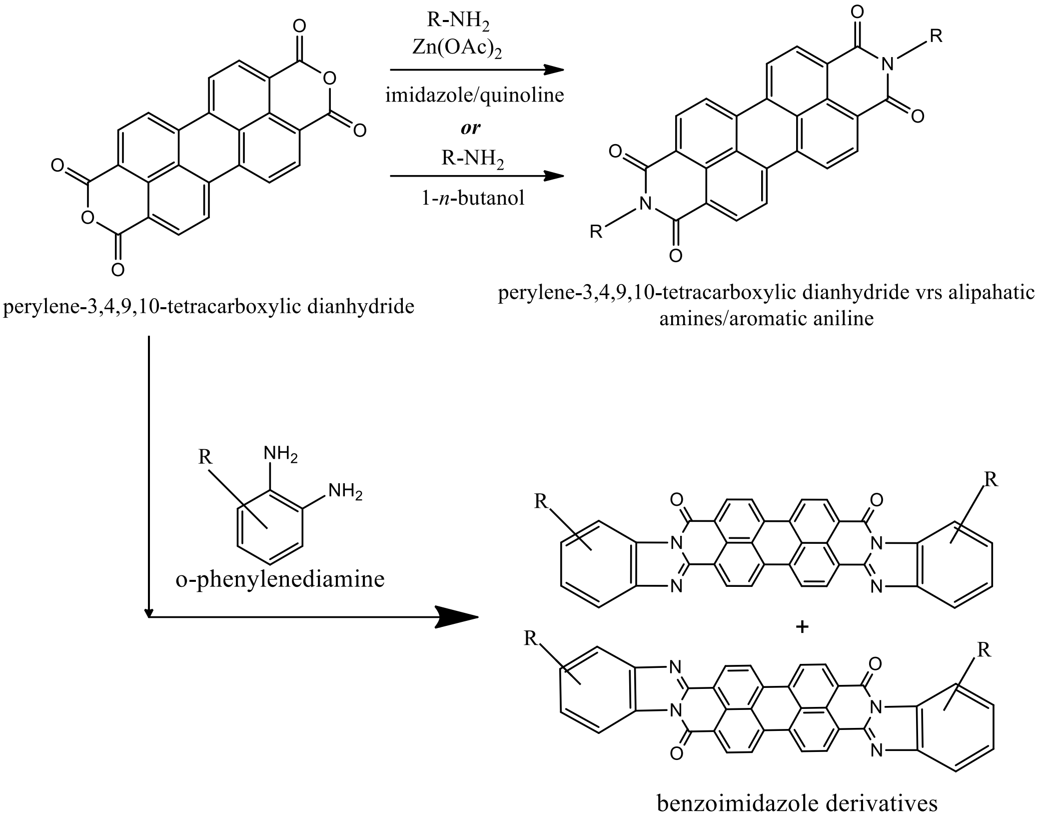

Scheme 1.2. Imide Substituent Positions of PDI Preparations (2)

Scheme 1.3 shows the imide substituent positions of asymmetric PDI preparations. Two methods of perylene diimide synthesis with diverse substituents on the imide position through a multi-step organic synthesis exist from Scheme 1.3. The preparation of the individual symmetrical perylene diimide dyes becomes the first step of the first synthetic method for asymmetrical perylene diimide. Almost 50% yield of the individual perylene monoimides monoanhydride compounds are due to hydrolysis of symmetrical perylene diimide. A subsequent imidization reaction of the perylene monoimides monoanhydride derivatives with a second aniline/amine introduces other substituents to create the anticipated asymmetrical perylene diimides. It is noteworthy that a direct synthesis of the perylene monoimides monoanhydride derivatives from the perylene-3,4,9,10-tetracarboxylic dianhydride with the primary amine is very challenging due to the difficulty in ensuring a one-site-condensation reaction. The aforementioned method has been employed in the synthesis of perylene imide benzoimidazole [198].

Another method for the synthesis of asymmetrical perylene diimides begins with the hydrolysis of the perylene-3,4,9,10-tetracarboxylic dianhydride to form the perylene monoimides monoanhydride salt and subsequently introducing functionalization reactions like imidization (see Scheme 1.3) [199].

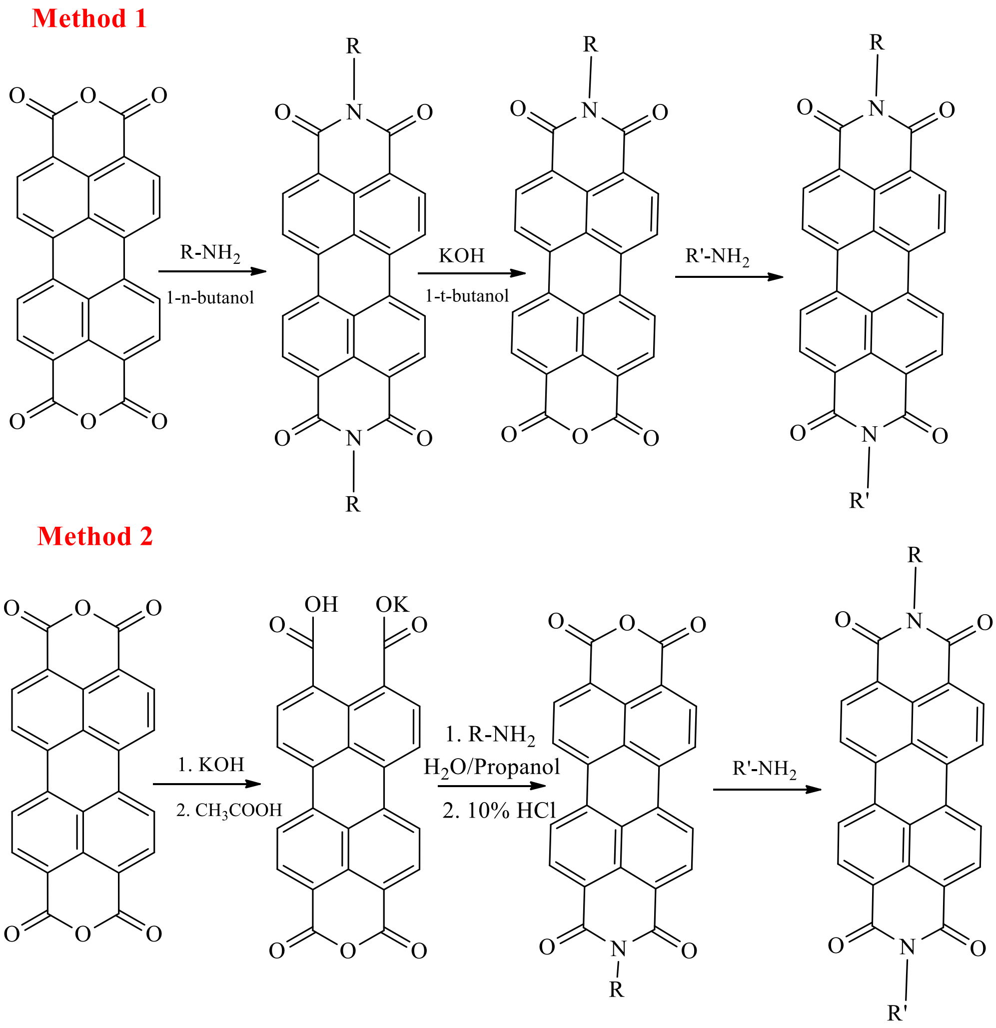

Scheme 1.3. Imide Substituent Positions of Asymmetric PDI Preparations

3.9.4 1,7-Di-Substituted Derivatives

Perylene bisimides are a class of outstanding organic dyes receiving much attention in both industrial and academic research. Their enormous physical properties like photo and thermal stability, optical, chemical robustness, and electronic properties make them a potential candidate for industrial colorants, n-type semiconductors (photovoltaic and organic electronics), and fluorescent sensors [200].

Perylene tetracarboxylic acid derivatives with modified optical and electrochemical properties while preserving good solubility, outstanding stability and high fluorescence quantum yields are shown in Figure 3.23. The absorption and emission spectra of **A1** [201], **B1** [202], **C1**, and **D1** [201] compounds in Figure 3.23 shift bathochromically and increases electron deficiency from left to right. The structure of **A1-D1** can be modified by attaching the peri positions (3,4,9,10-tetracarboxylic acid) or the bay positions (1,6,7,12) with different functional groups. It has emerged that, additional alteration in the electrochemical and optical properties may arise at the bay positions, due to insensitivity to the substituent changes at the carboxylic acid positions [200]. Due to this, bay-brominated derivatives (**A2**, **B2**, **C2**, and **D2**) can participate in a different substitution reactions with their bromine atoms to produce highly valued and multipurpose intermediates for bay-functionalized chromophore synthesis with tunable optical and electronic properties.

Substitution at the bay position normally consist of two or four substituents, with a prior halogenation of perylene-3,4,9,10-tetracarboxylic bisanhydride to yield 1,7-dibromoperylene-3,4,9,10-tetracarboxylic bisanhydride [170] or 1,6,7,12-tetrachloro perylene-3,4,9,10-tetracarboxylic bisanhydride [203]. An isomerically impure mixture of 1,7- and 1,6-isomers, from a substitution at the bay position of 1,7-dibromoperylene-3,4,9,10-tetracarboxylic bisanhydride are produced. Recent studies have demonstrated that the electrochemical and optical properties of 1,7- and 1,6-substituted perylene bisimides can be distinctly different [168]. In this way, an isomeric purity of the aforementioned compounds is highly significant.

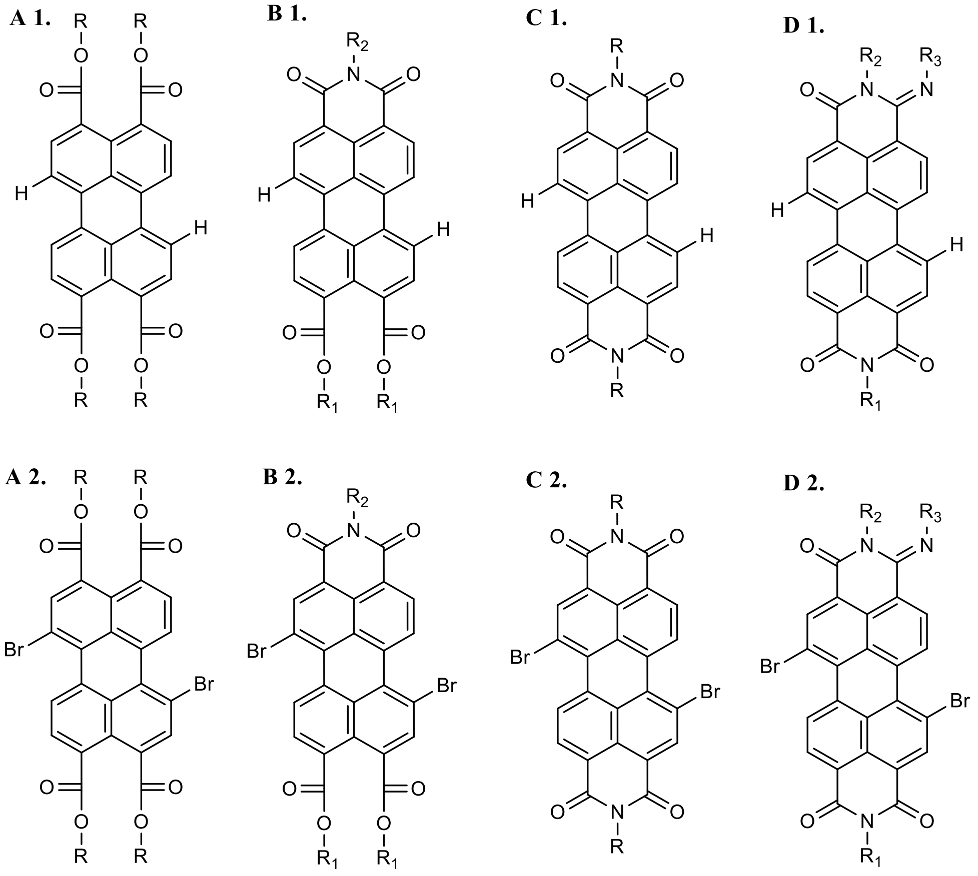

Figure 3.23. Perylene tetracarboxylic acid derivatives

Apart from 1,7-dibromoperylene-3,4,9,10-tetracarboxylic bisanhydride and perylene bisimides, the synthesis of 1,7-dibromoperylene-3,4,9,10-tetracarboxylic tetraesters have been reported in literature [204]. However, the isomerically pure form of 1,7-dibromoperylene-3,4,9,10-tetracarboxylic tetraesters have not been obtained. Various techniques like chromatography, repetitive recrystallization or solubility difference dependent separation have been used to improve the isomeric purity of 1,7-substituted products from a mixture of 1,7- and 1,6-isomers of dibromoperylene-3,4,9,10-tetracarboxylic bisanhydride and perylene-3,4,9,10-tetracarboxylic tetraesters [171, 173, 205]. However, due to the limitation to specific compounds, sensitivity to structural changes of the molecules and the limited efficiency of the aforementioned techniques, they are not suitable for extensive synthesis of regioisomerically pure derivatives.

Against the backdrop, Sengupta, Dubey [200] reported the first synthesis of regioisomerically pure dibromoperylene-3,4,9,10-tetracarboxylic derivatives, as shown in Scheme 2.1 and Scheme 2.2 (**3**-**8**). The synthesized compounds in Scheme 2.2 (**4**, **5** and **8**) with one or more anhydride functionality and 1,7 bromo substituted products, permit a nearly unlimited attachment of the substituents at the bay and peri-positions.

The synthesis of compounds shown in Scheme 2.1 and Scheme 2.2 (**3**-**8**) begun with a commercially existing perylene-3,4,9,10-tetracarboxylic bisanhydride (Scheme 2.1 (**1**)), which was synthesized into perylene-3,4,9,10-tetrabutylester (Scheme 2.1 (**2**)) with a subsequent dibromination in dichloromethane (DCM) at room temperature. The preferred pure 1,7 isomer (Scheme 2.1 (**3**)) was derived from a mixture of dibromides (Scheme 2.1 (**3** and **3a**)) via crystallization from an ACN/DCM mixture. 1,7 isomer (Scheme 2.1 (**3**)) was converted to Scheme 2.2 (**4**) by an acid-catalyst to remove two ester moieties in heptane at a temperature 90 degrees. An excess of *p*-TsOH.H_2O in toluene at a temperature 100 degrees is used to convert 1,7 isomer (Scheme 2.1 (**3**)) to bisanhydride (Scheme 2.2 (**5**)). Anhydrides (Scheme 2.2 (**4** and **5**)) are imidized with 2,6 dissopropylaniline in NMP and acetic acid, resulting in compounds in Scheme 2.2 (**6** and **7**). Compound in Scheme 2.2 (**6**) was treated with *p*-TsOH.H_2O in excess toluene at a temperature 100 degrees to yield compound in Scheme 2.2 (**8**).

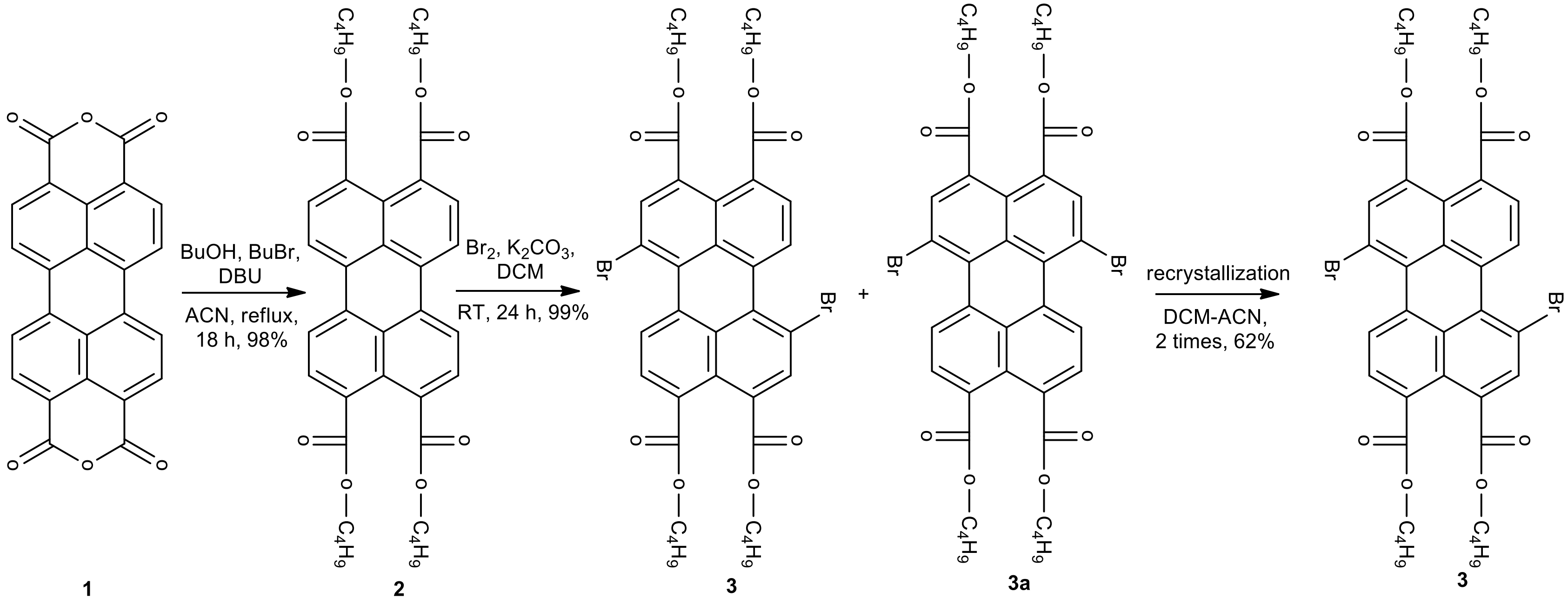

Scheme 2.1. Synthesis of 1,7-Dibromoperylene-3,4,9,10-tetracarboxy Tetrabutylester (**3**) from PBA (**1**)

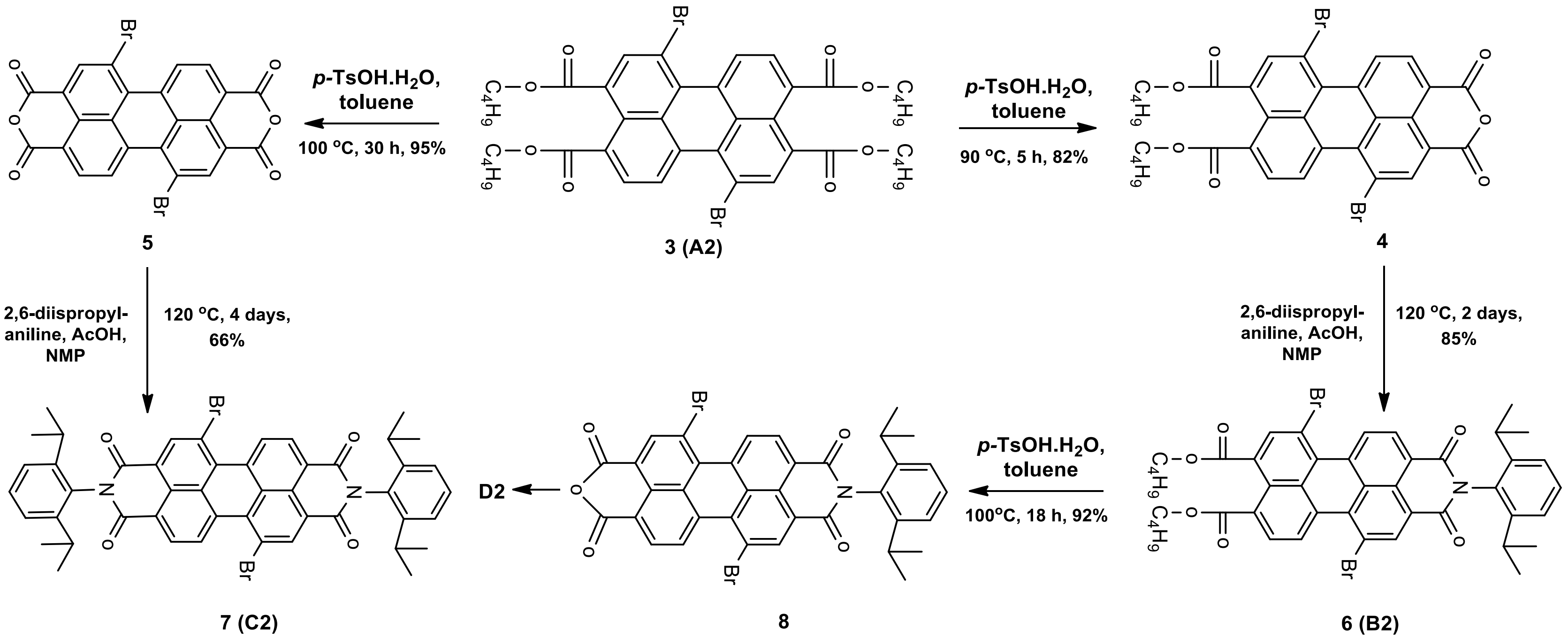

Scheme 2.2. Synthesis of 1,7-Dibromo-Substituted Compounds (4-8) from 3

CHAPTER 4

EXPERIMENTAL

4.1 Materials and Instruments

The commercially available chemicals and solvents employed in the study were purchased from either Merck Millipore or Sigma-Aldrich and were reagent grade purity. Chemicals and reagents were used as received, without further purification unless otherwise stated. Solvents used for chromatographic separations were purified according to standard purification methods [206]. Moisture/air-sensitive reactions were performed under argon (Ar) atmosphere. N-Methyl 2-pyrrolidone (NMP) was dried over molecular sieves. Chromatographic purification was done with silica gel pore size 60 Å, 70-230 mesh, 63-200 μm, for column chromatography and thin layer chromatography (TLC) was performed on aluminium TLC plate, silica gel coated with fluorescent indicator F254. Melting points were determined with Mel-Temp® capillary melting point apparatus and were uncorrected. Nuclear magnetic resonance (NMR) spectra were measured and recorded on a Bruker Avance 400 MHz NMR spectrometer. FTIR spectra were recorded with a Varian-660 IR spectrometer in the 4000–400 cm^{-1} spectral range in the transmittance mode. Solid samples were recorded as KBr pellets. UV-visible measurements were recorded either on a PG-Instruments T80+ or on Shimadzu UV-2450 spectrophotometer. Fluorescence emission spectrums were recorded on a Shimadzu RF-5301PC Spectrofluorophotometer Spectral data were processed into graphs with Microsoft Excel™; spectral data were analyzed via curve fitting procedures using nonlinear regression analysis with the help of OriginLab® software and Spectragryph optical spectroscopy software [207] in order to determine molar absorptivity coefficients at the selected wavelengths and quantum yields. All solvents employed for spectral measurements were of a spectroscopic grade.

4.2 Synthetic Procedures

4.2.1 Synthesis of perylene-tetracarboxylic tetrabutyl ester (P-1)

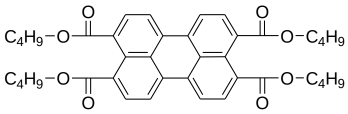

A mixture of PDA (0.980 g, 1 equivalent), 1,8-Diazabicyclo[5.4.0]undec-7-ene (DBU) (4 equivalent), n-butanol (1.5 g, 8 equivalent) in 500 ml of N,N-Dimethylmethanamide (DMF) was stirred at 60°C for 0.5 hour. 1-bromobutane (2.74 g, 8 equivalent) was added to the mixture and a subsequent addition of another 9 ml of DMF, and further stirred for 3 hours. After cooling the resulting mixture to room temperature, the solvent was poured into water (100 ml) and stirred for 15 minutes, after which it was filtered. The crude residue after the filtration process was subjected to column chromatography on silica gel, eluting with dichloromethane (CH_2Cl_2), to produce compound (P-**1**) in a golden-orange solid (yield, 1.54 g). Characterization data for P-**1**: IR (KBr): 3247, 2964, 2330, 1730, 1587, 1447, 1304, 1034, 810, 737, 606 cm^{-1}; $\lambda_{\max\,\mathrm{CHCl_3}}$= 472 nm (ε = 63593, Pearson's r = 0.99 and R^2 = 0.98) and 443 nm (ε = 51863, Pearson's r = 0.99 and R^2 = 0.98); $\lambda_{\max\,\mathrm{DMF}}$ = 469 nm (ε = 46069, Pearson's r = 1.00 and R^2 = 1.00), and 441 nm (ε = 38616, Pearson's r = 1.00 and R^2 = 1.00); and, ^1H NMR ($CDCl_3$, 400 MHz): 1.04 (t, 12H), 1.55 (m, 8H), 1.83 (m, 8H), 4.37 (t, 8H), 7.80 (d, 4H), 7.85 (d, 4H); ^{13}C NMR ($CDCl_3$, 100 MHz): 13.8, 19.3, 30.7, 65.3, 121.1, 128.3, 128.5, 130.1, 132.4, 168.5. The ^1H NMR and ^{13}C NMR Spectrum of P-**1** are presented in Figure 4.1 and Figure 4.2.

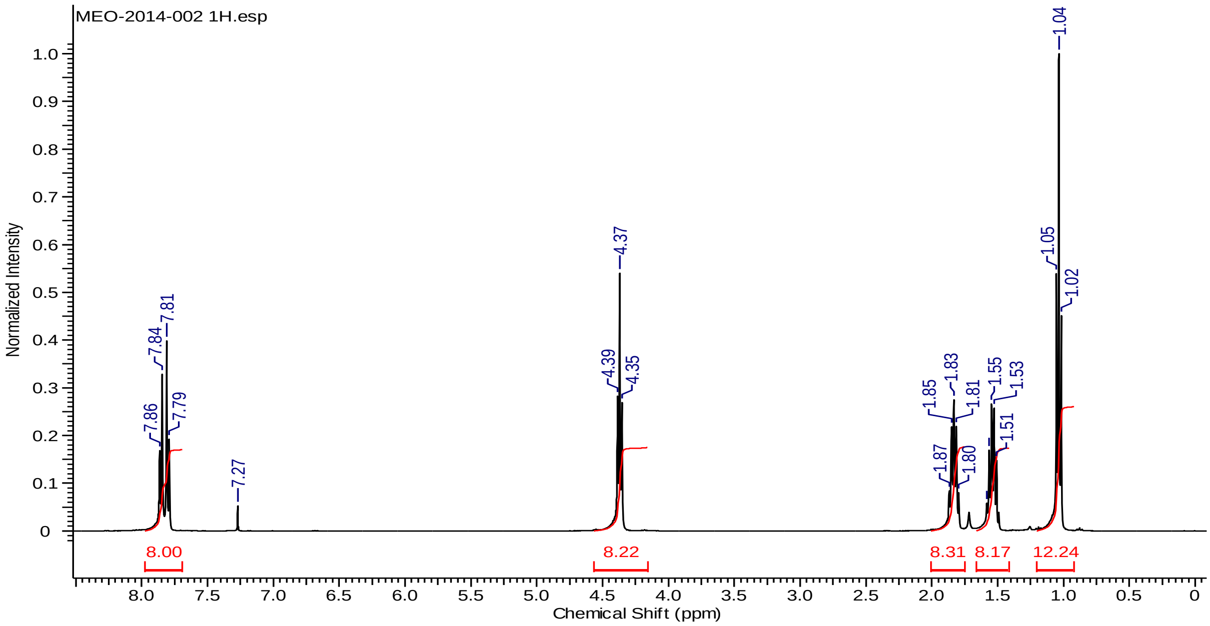

Figure 4.1. ^{1}H NMR Spectrum of P-**1**

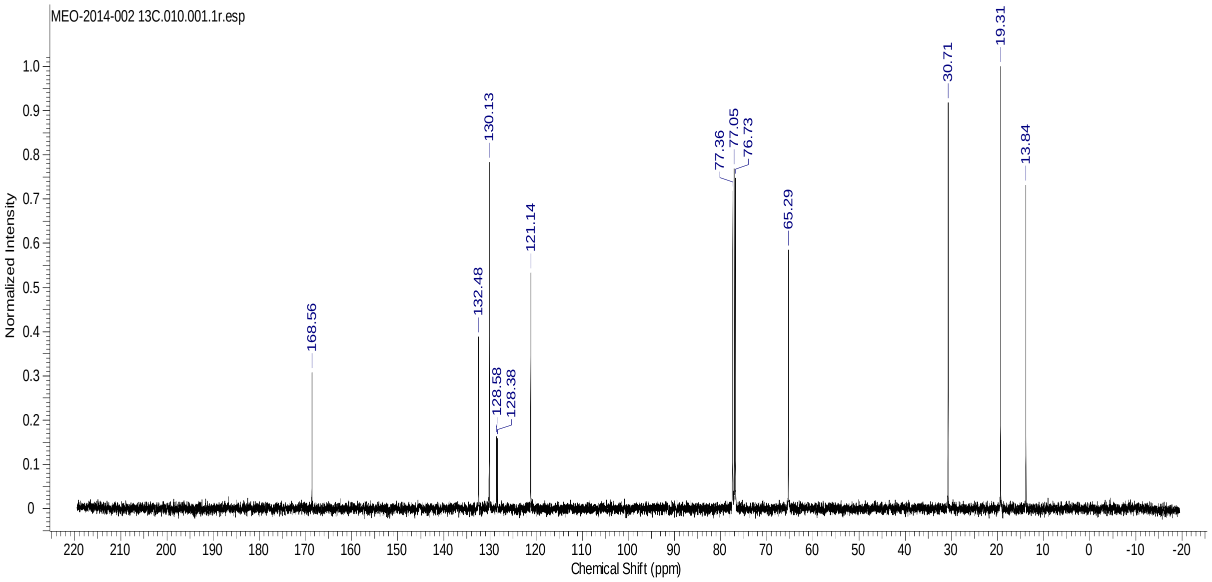

Figure 4.2. ^{13}C NMR Spectrum of P-**1**

4.2.2 Synthesis of 1,7-dibromoperylene-3,4,9,10-tetracarboxyl tetrabutylester (P-2)

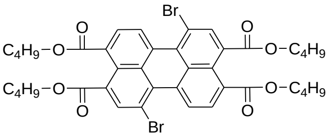

A mixture of perylene tetrabutylester 5 (0.5 g, 0.766 mmol) and K_2CO_3 (0.25 g, 1.81 mmol) were taken into a 50 mL round-bottom flask, with a subsequent addition of CH_2Cl_2 (10 mL). Drop wise, bromine (0.5 mL, 9.70 mmol) was added to the resulting mixture and stirred for 24 hours at room temperature. Afterwards, an aqueous solution of sodium metabisulphite ($Na_2S_2O_5$) was added drop wise to the reaction mixture while stirring. The organic layer of the reaction mixture was washed with several portions of water and dried over sodium sulphate (Na_2SO_4). The solvent was then removed by rotary evaporation giving crude product (0.597 g) consisting of a mixture of 1,7- and 1,6-dibromo isomers. The isolation of the regioisomerically pure 1,7- dibromo was accomplished by a double crystallization from dichloromethane / acetonitrile. Characterization data for P-**2**: IR (KBr): 3577, 3328, 2952, 2870, 2511, 2331, 2086, 1944, 1731, 1589, 1454, 1385, 1303, 1168, 1051, 951, 816, 740, 603 cm^{-1}; $\lambda_{\mathrm{max\ CHCl_3}}$= 468 nm (ε = 32363, Pearson's r = 1.00 and R^2 = 1.00) and 443 nm (ε = 28719, Pearson's r = 1.00 and R^2 = 1.00); $\lambda_{\mathrm{max\ DMF}}$ = 466 nm (ε = 31509, Pearson's r = 1.00 and R^2 = 1.00), and 441 nm (ε = 28249, Pearson's r = 1.00 and R^2 = 1.00); and, ^1H NMR ($CDCl_3$, 400 MHz): 1.00 (t, 12H), 1.60-1.46 (m, 8H), 1.81-1.77 (m, 8H), 4.34 (t, 8H), 8.08 (d, 2H), 8.28 (s, 2H), 8.91 (d, 2H); ^{13}C NMR ($CDCl_3$, 100 MHz): 13.8, 19.2, 30.6, 65.6, 65.8, 118.7, 126.5, 127.6, 129.0, 130.4, 131.1, 131.7, 136.7, 167.1, 168.0. Figure 4.3 and Figure 4.4 depict the ^1H NMR and ^{13}C NMR Spectrum of P-**2**.

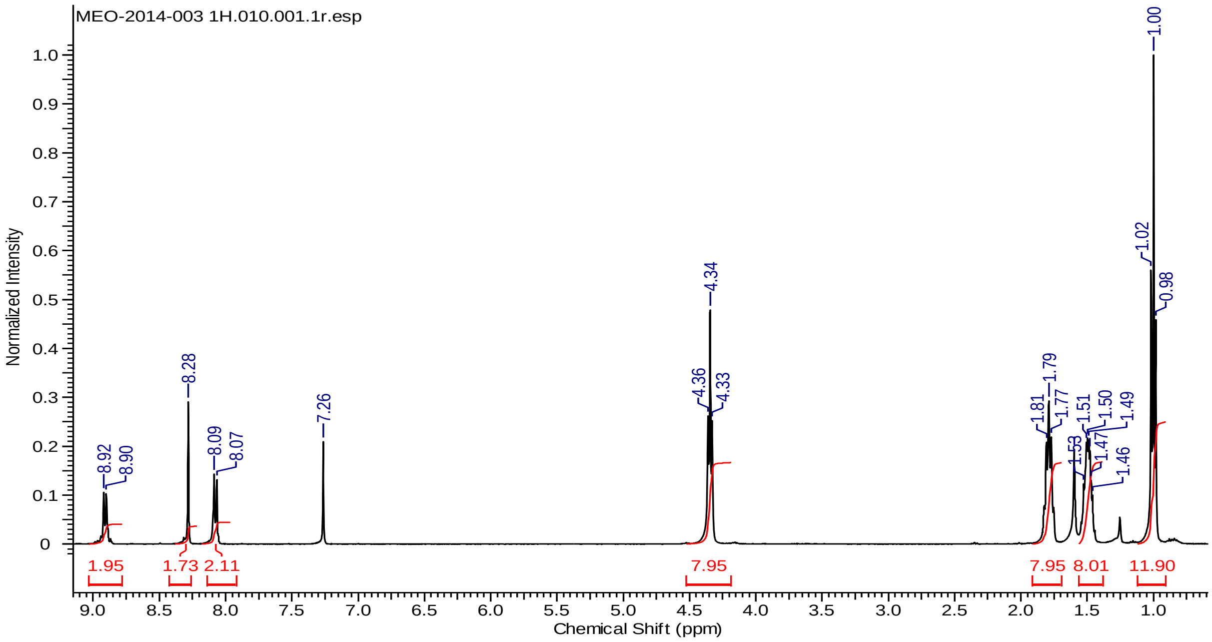

Figure 4.3. ^{1}H NMR Spectrum of P-**2**

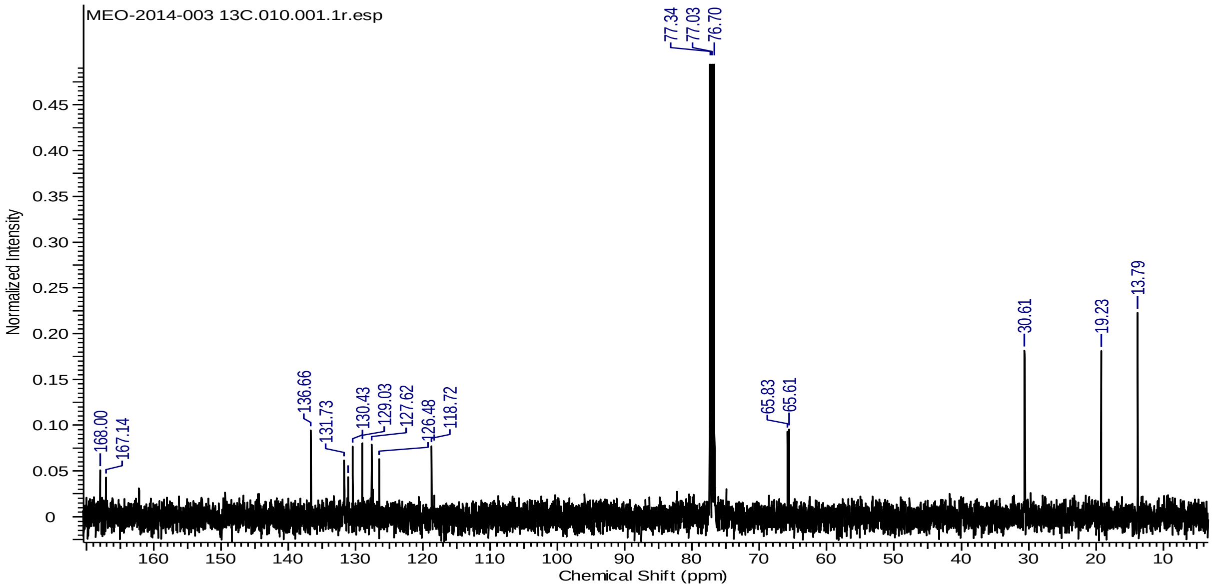

Figure 4.4. ^{13}C NMR Spectrum of P-**2**

4.2.3 Synthesis of 1,7-Dibromoperylene-3,4,9,10-tetracarboxy monoanhydride Dibutylester (P-3)

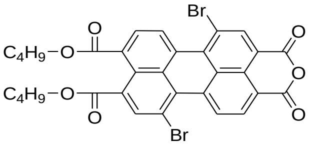

Regioisomerically pure P-**2** (1 g, 1.23 mmol) and p-toluenesulfonic acid monohydrate (p-TsOH·H_2O) (305 mg, 1.60 mmol) were taken in 3 mL of n-heptane. The reaction mixture was stirred at 90 °C for 5 hours. The product (P-**2**) begun to precipitate from the reaction mixture within a period. The reaction mixture was cooled to room temperature after 5 hours, and the product was filtered off and washed with some few portions of methanol and water. The dried orange precipitate was subsequently taken in methanol (200 mL) and refluxed for 2 hours. The refluxed mixture of compounds was cooled to room temperature and filtered to remove the starting compound. The residue was the monoanhydride compound (P-**3**), whereas the remaining was the starting material (P-**2**) soluble in methanol. Finally, the dried residue was dissolved in a little amount of dichloromethane (DCM) and filtered to remove the insoluble bisanhydride. The solvent was then evaporated to produce the crude product. Purification by column chromatography, using chloroform, gave 0.254 g of the product (32% yield). Characterization data for P-**3**: IR (KBr): 3454, 3058, 2943, 2871, 2727, 2510, 2364, 1782, 1706, 1602, 1458, 1379, 1271, 1168, 1019, 806, 695 cm^{-1}; $\lambda_{\max\,\mathrm{CHCl_3}}$= 505 nm (ε = 41209, Pearson's r = 1.00 and R^2 = 1.00) and 484 nm (ε = 34093, Pearson's r = 1.00 and R^2 = 1.00); $\lambda_{\max\,\mathrm{DMF}}$ = 497 nm (ε = 32017, Pearson's r = 1.00 and R^2 = 1.00), and 469 nm (ε = 26757, Pearson's r = 1.00 and R^2 = 1.00); Melting point: 205 °C (literature 202 °C); ^1H NMR (400 MHz, $CDCl_3$): δ = 9.27 (d, J = 8.0 Hz, 1H), 9.24 (d, J = 8.1 Hz, 1H), 8.89 (s, 1H), 8.68 (d, J = 8.0 Hz, 1H), 8.34 (s, 1H), 8.15 (d, J = 8.0 Hz, 1H), 4.39−4.33 (m, 4H), 1.85−1.78 (m, 4H), 1.54−1.48 (m, 4H), 1.04−1.00 ppm (m, 6H). Figure 4.5 shows the ^1H NMR spectrum of compound (P-**3**) in $CDCl_3$.

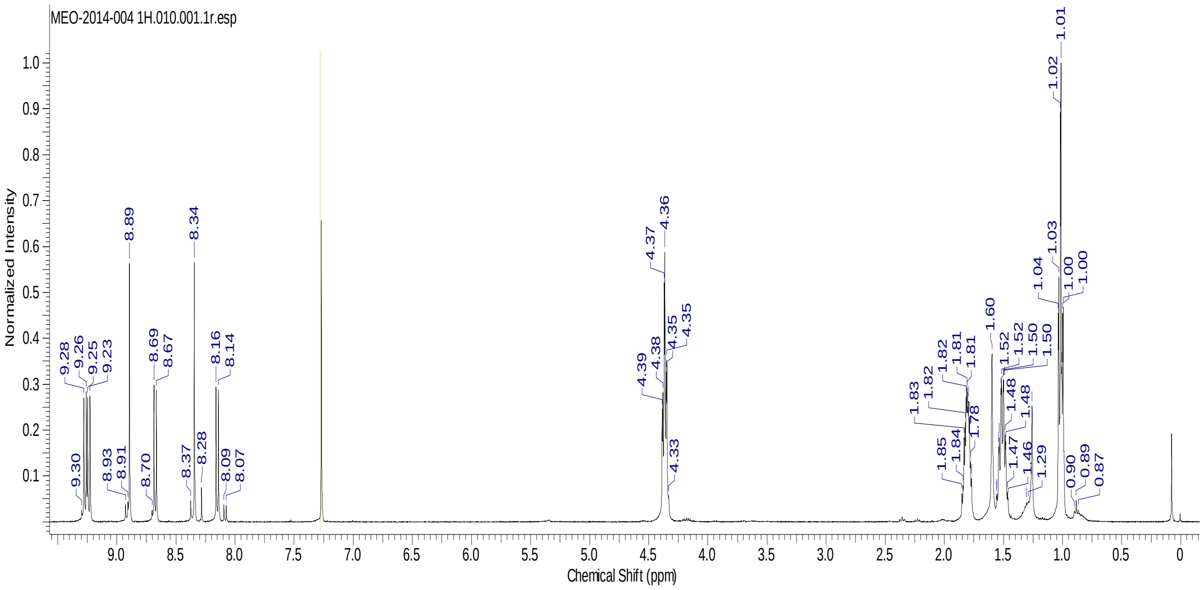

Figure 4.5. ^{1}H NMR spectrum of P-**3** in $CDCl_3$

4.2.4 Synthesis of 1,7-Dibromoperylene-3,4,9,10-tetracarboxylic bisanhydride (P-X)

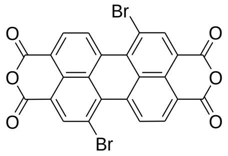

In 20 ml of toluene, regioisomerically pure tetrabutylester (P-**2**) (0.5 g, 0.618mmol), and p-toluenesulfonic acid monohydrate (3.09mmol, 0.6g) were mixed and the resulting mixture was stirred at 100°C for 30 hrs. After cooling to room temperature, resulting red precipitate was filtered and washed with methanol (3 × 25 ml) and water (3 × 25 ml), and resulting solid was dried at 100°C in a vacuum oven. The crude product was taken into 100 ml of chloroform and refluxed for 3 hrs. After cooling to RT, filtered, washed with chloroform and dried at 65°C in a vacuum oven to afford 0.322 g of brown/red solid product. (95% yield). Because of the low solubility of this product, NMR-spectrum were not recorded and used without further purification.

4.2.5 Synthesis of 1,7-Dibromo-N,N’-Bis[2-(diethylamino)ethyl]-3,4,9,10-perylene- tetracarboxylic Diimide (P-4)

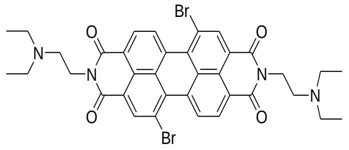

In a 50 ml of round-bottom flask, 1,7-Dibromoperylene-3,4,9,10-tetracarboxylic bisanhydride (P-**X**) (0.518 g, 0.93mmol) synthesized at the previous step was suspended in 15 ml of water / 2-propanol (1:1 v/v) mixture. To this, N,N-diethylene diamine (0.312 g, 2.7 mmol) and glacial acetic acid (0.327 g, 5.5 mmol) was added via syringes. Resulting mixture was stirred at 80°C under argon atmosphere for 40 hrs. After cooling to room temperature, solvent removed under reduced pressure. Resulting solid residue was dissolved in dichloromethane (50 ml) and filtered to remove unreacted starting material. After removing the solvent under reduced pressure, resulting crude product was chromatogramed on silica, eluting with dichloromethane / methanol (10:1) to afford 0.34 g of pure product, after removal of solvent. (Red solid, R_f = 0,36) (49.5 % yield). Characterization data for P-**4**: IR (KBr): 3561, 3313, 3237, 3237, 3162, 3054, 2950, 2802, 2582, 2468, 2327, 2106, 1927, 1685, 1602, 1347, 1237, 1168, 1092, 947, 871, 796, 692 cm^{-1}; $\lambda_{\max \mathrm{CHCl_3}}$= 526 nm (ε = 57019, Pearson’s r = 1.00 and R^2 = 0.99) and 491 nm (ε = 40512, Pearson’s r = 1.00 and R^2 = 0.99); $\lambda_{\max \mathrm{DMF}}$ = 523 nm (ε = 38811, Pearson’s r = 1.00 and R^2 = 0.99), and 488 nm (ε = 27925, Pearson’s r = 1.00 and R^2 = 0.99); ^{1}H NMR (400 MHz, $CDCl_3$): δ = 9.38 (d, J = 8.3 Hz, 2H), 8.83, (s, 2H), 8.61 (d, J = 8.2 Hz, 2H), 8.61 (d, J = 7.3 Hz, 2H), 4.31 (t, J = 7.3 Hz, 4H), 2.81 (t, J = 7.2 Hz, 4H), 2.67 (q, J = 7.3 Hz, J = 7 Hz, 8H), 1.09 (t, J = 7 Hz, 12H). Figure 4.6 shows the ^{1}H NMR spectrum of compound (P-**4**) in $CDCl_3$.

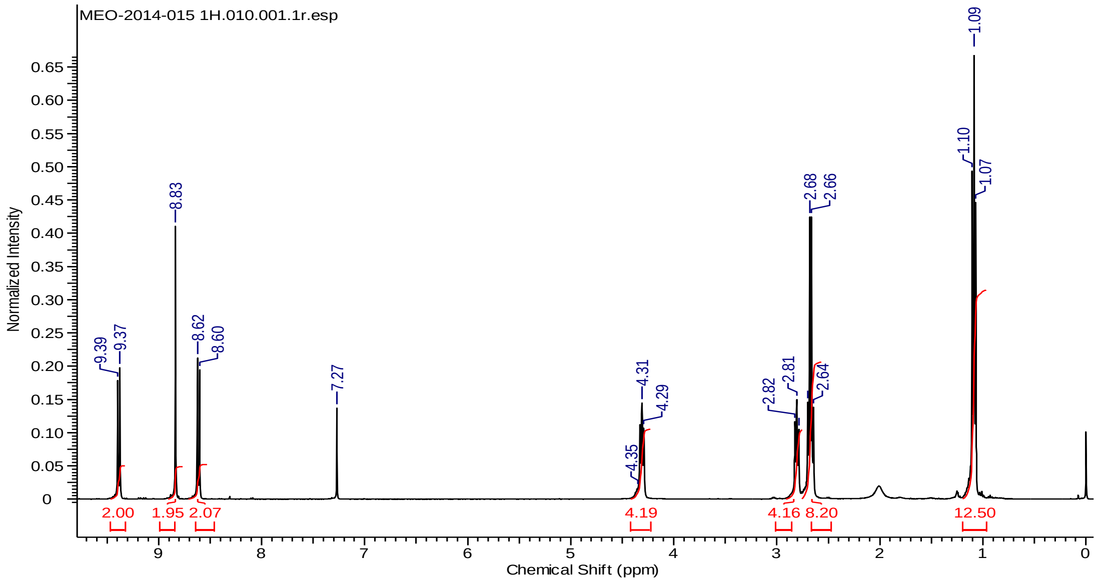

Figure 4.6. ^{1}H NMR spectrum of P-**4** in $CDCl_3$

4.2.6. Synthesis of 1,7-Di(4-tert-butylphenoxy)-N,N'-bis[2-(diethylamino)ethyl]-3,4,9,10-perylene- tetracarboxylic diimide (P-5)

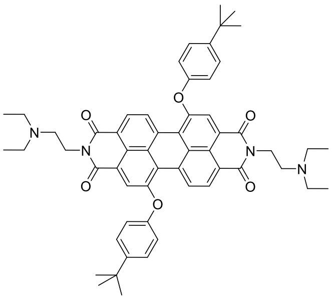

4-tert-butylphenol (59 mg, 3 eq.), K_2CO_3 (108 mg, 6 eq.), and 18-crown-6 (409 mg, 12 eq) was dissolved in 10 ml of dry toluene, and stirred for 20 min. under argon atmosphere. To this was added 1,7-Dibromo-N,N'-bis[2-(diethylamino)ethyl]-3,4,9,10-perylene- tetracarboxylic diimide (P-**4**) (100 mg, 1 eq) and resulting mixture was stirred at 90 °C under argon for 40 hrs. After cooling down the reaction mixture to RT., solvent removed under reduced pressure. Resulting solid was washed with water, dried and crude product was purified by flash column chromatography on silica, eluting with $CHCl_3$ / Methanol (100:5, v/v) to give 80 mg dark red solid product. (69 % yield, R_f = 0.28). Characterization data for P-**5**: $\lambda_{\mathrm{max}\ \mathrm{CHCl_3}}$= 548 nm (ε = 53394, Pearson's r = 1.00 and R^2 = 1.00) and 512 nm (ε = 35820, Pearson's r = 1.00 and R^2 = 1.00); $\lambda_{\mathrm{max\ DMF}}$ = 541 nm (ε = 35052, Pearson's r = 1.00 and R^2 = 1.00), and 508 nm (ε = 24658, Pearson's r = 1.00 and R^2 = 1.00); ^{1}H NMR (400 MHz, $CDCl_3$): δ = 9.53 (d, J = 8.5 Hz, 2H), 8.52 (d, J = 8.5 Hz, 2H), 8.31, (s, 2H), 7.47 (d, J = 8.5 Hz, 4H), 7.10 (d, J = 8.8 Hz, 4H), 4.25 (t, J = 7.5 Hz, 4H), 2.78 (t, J = 7.5 Hz, 4H), 1.39 (s, 18H), 1.09 (t, J = 7 Hz, 12H). Figure 4.7 shows the ^{1}H NMR spectrum of compound (P-**5**) in $CDCl_3$.

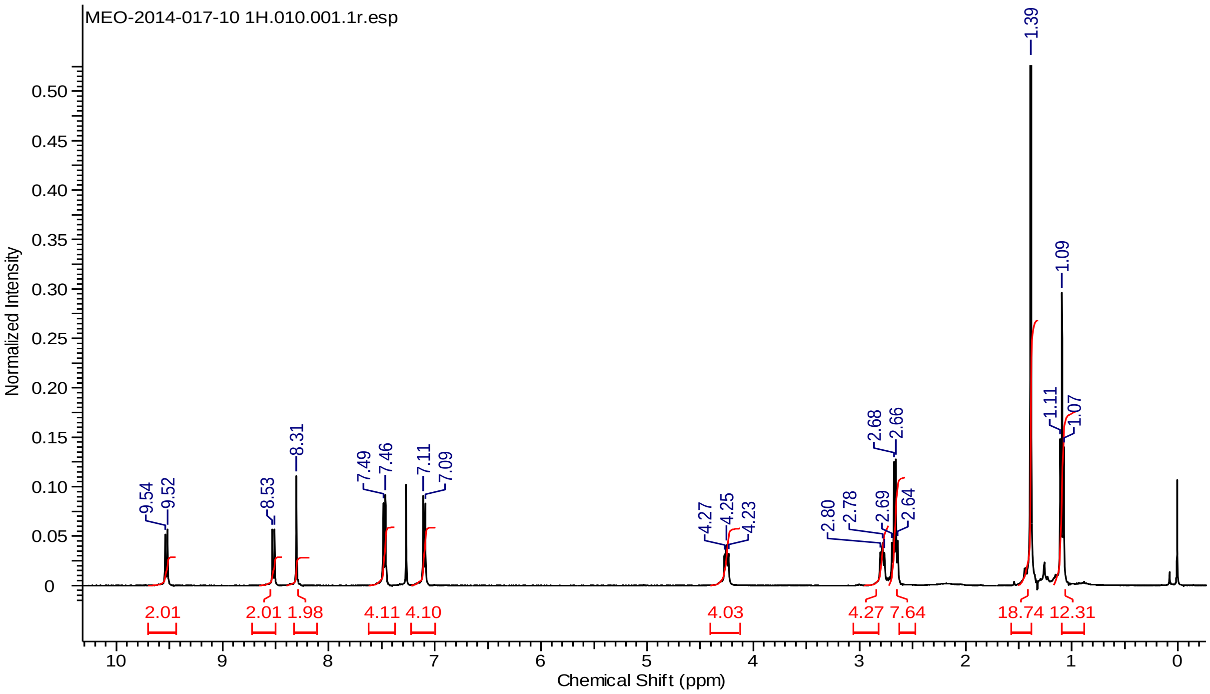

Figure 4.7. ^{1}H NMR spectrum of P-**5** in $CDCl_3$

4.2.7. Synthesis of 1,7-Di(pyrrolidinyl)-N,N'-bis[2-(diethylamino)ethyl]-3,4,9,10-perylene- tetracarboxylic diimide (P-6)

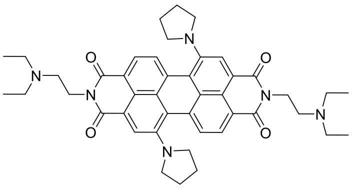

1,7-Dibromo-N,N'-bis[2-(diethylamino)ethyl]-3,4,9,10-perylene- tetracarboxylic diimide (P-**4**) (76 mg, 1 eq) was dissolved in 4 ml of pyrrolidine and stirred under argon atmosphere at 60°C for 24 hrs. After cooling to RT., solvent removed under reduced pressure. The resulting green crude product was purified by flash-column chromatography on silica, eluting with CH_2Cl_2 / Methanol (10:1, v/v) giving 50 mg of green pure product. (70 % yield, R_f = 0.23). Characterization data for P-**6**: $\lambda_{\max\ CHCl_3}$ = 704 nm (ε = 32485, Pearson's r = 1.00 and

R^2 = 1.00) and 436 nm (ε = 14843, Pearson's r = 1.00 and R^2 = 1.00); $\lambda_{\mathrm{max\ DMF}}$ = 704 nm (ε = 27057, Pearson's r = 1.00 and R^2 = 1.00), and 433 nm (ε = 12764, Pearson's r = 1.00 and R^2 = 1.00); ^{1}H NMR (400 MHz, $CDCl_3$): δ = 8.45 (s, 2H), 8.40 (d, J = 8 Hz, 2H), 7.66, (d, J = 8 Hz, 2H), 4.35 (t, J = 6 Hz, 4H), 3.74 (bm, 4H), 2.88-2.72 (m, 16H), 2.09-1.97 (m, 8H), 1.16 (t, J = 7 Hz, 12H). Figure 4.8 shows the ^{1}H NMR spectrum of compound (P-**6**) in $CDCl_3$.

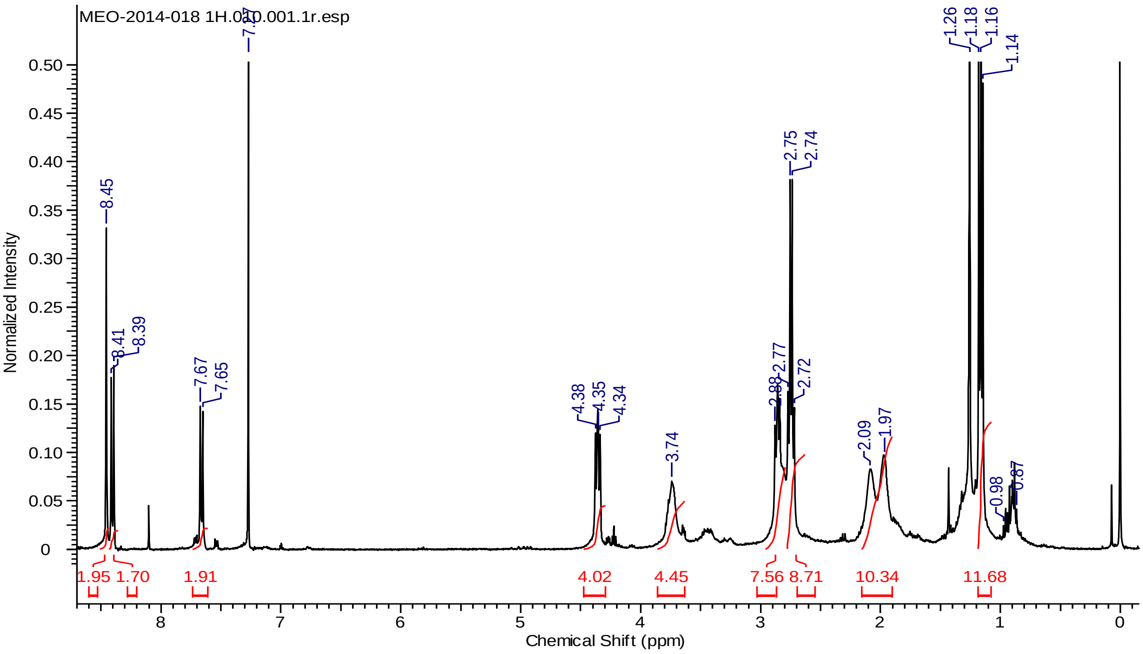

Figure 4.8. ^{1}H NMR spectrum of P-**6** in $CDCl_3$

4.3 Data and Calculations

4.3.1 Maximum Extinction Coefficient (ε_{max})

The maximum extinction coefficient measures the strength of light absorption by a chemical special at a given wavelength. According to Beer Lambert's law, the maximum extinction coefficient is a linear relationship between the absorbance and concentration and path length of light. The mathematical representation of the maximum extinction coefficient is:

$$\varepsilon_{max} = \frac{A}{cl} \tag{5.1}$$

Where ε_{max} is the maximum extinction coefficient at a certain absorption wavelength ($L \cdot mol^{-1} \cdot cm^{-1}$), A is absorbance, c is the concentration ($mol \cdot L^{-1}$) and l is the path length of light (cm).

4.3.2 Absorption and Emission Properties

Based on the Beer Lambert's law in equation (5.1), the molar absorptivity coefficient was calculated from the plot of absorbance versus concentration. A minimum of five concentrations of the selected compounds' solution was prepared and their corresponding absorbance for each of the two wavelength peaks was recorded and analyzed. The analysis revealed the slope (ε), intercept, Pearson's correlation coefficient and R-squared between the plots of absorbance versus concentration. The output analysis of the data presents a plot of the actual spectra, the absorbance versus concentration plot of the compounds at each of the two peaks for different concentrations in different solvents ($CHCl_3$ and DMF). The absorbance versus concentration plot of the compounds at each of the two peaks for the selected concentrations is presented in Figure 4.9 - Figure 4.44. The normalized absorption and emission spectra are presented in Figure 4.45 - Figure 4.56.

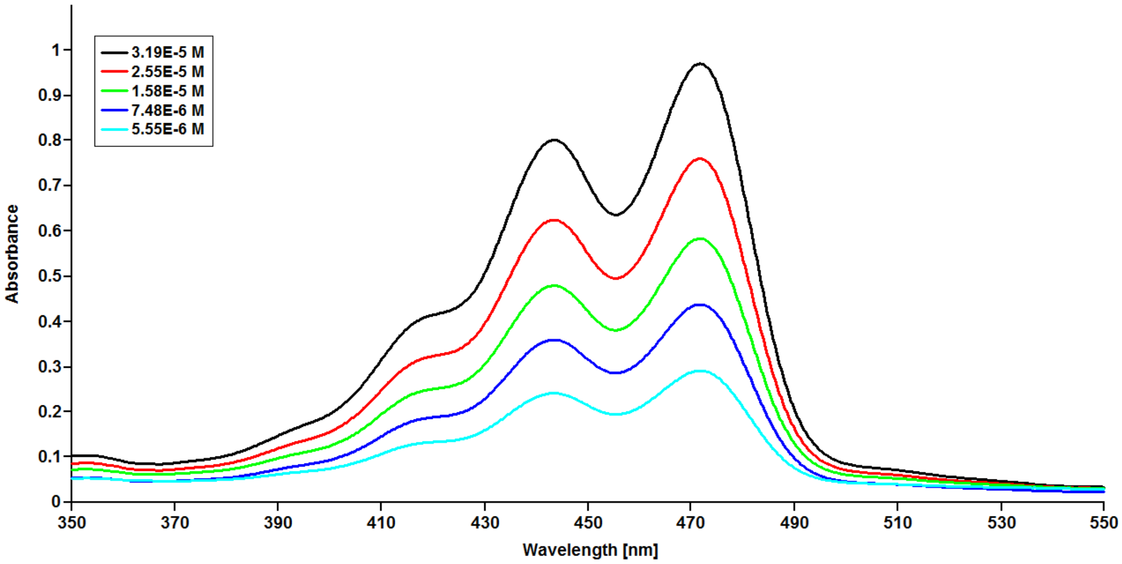

Figure 4.9. Absorption spectra of P-**1** in $CHCl_3$

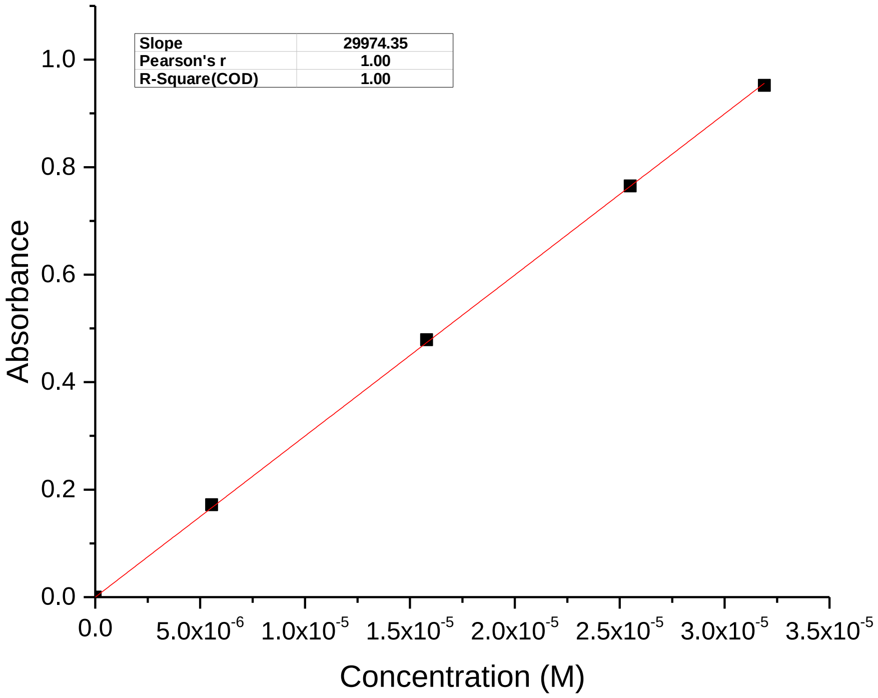

Figure 4.10. Absorbance versus Concentration plot of P-**1** at 472 nm in $CHCl_3$

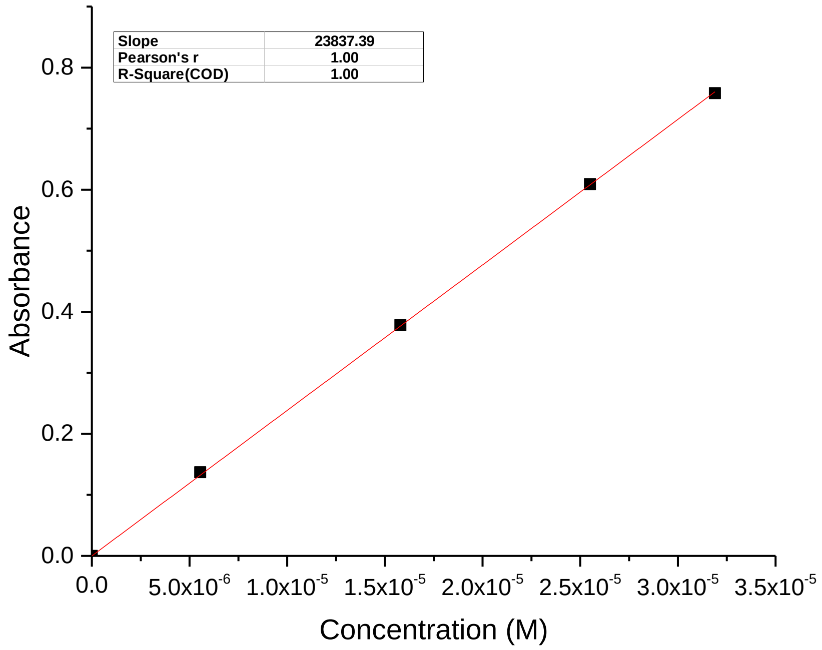

Figure 4.11. Absorbance versus Concentration plot of P-**1** at 443 nm in $CHCl_3$

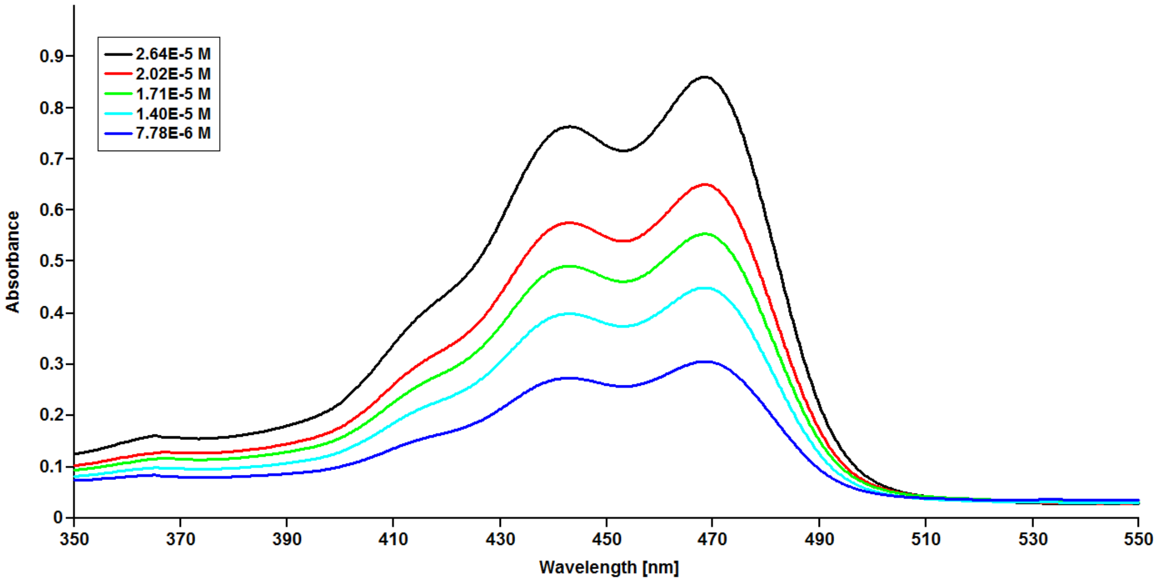

Figure 4.12. Absorption spectra of P-**2** in $CHCl_3$

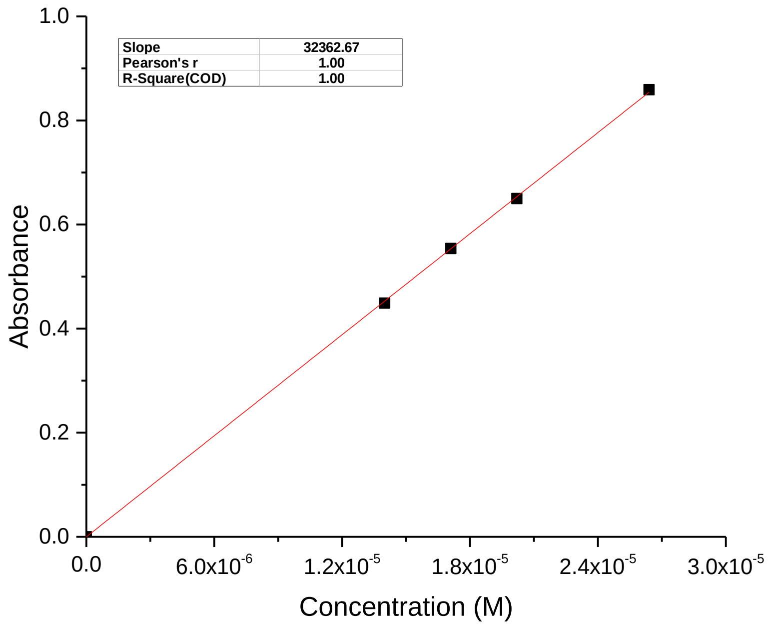

Figure 4.13. Absorbance versus Concentration plot of P-**2** at 468 nm in $CHCl_3$

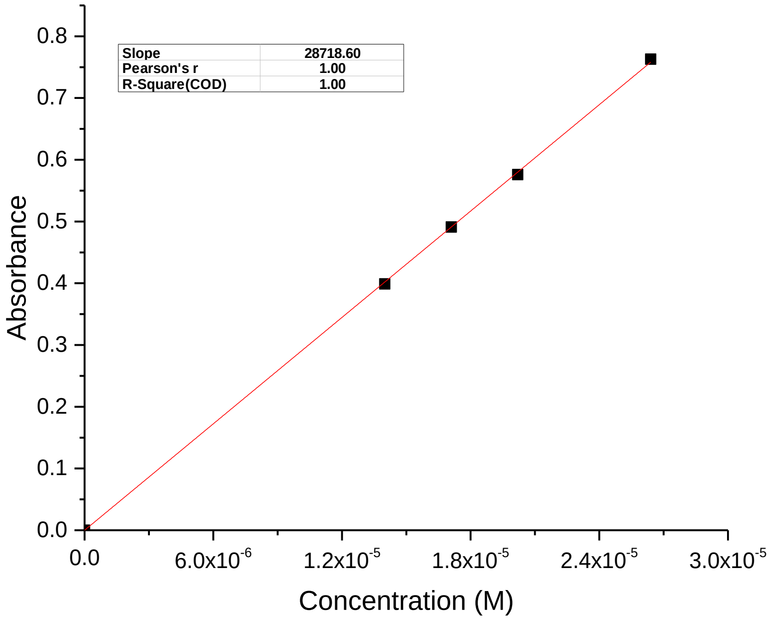

Figure 4.14. Absorbance versus Concentration plot of P-**2** at 443 nm in $CHCl_3$

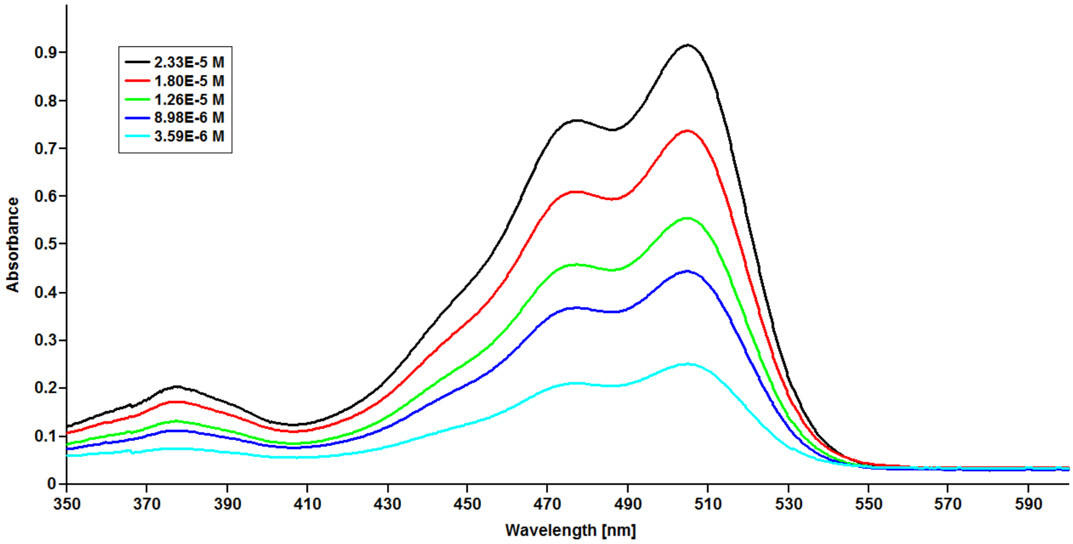

Figure 4.15. Absorption spectra of P-**3** in $CHCl_3$

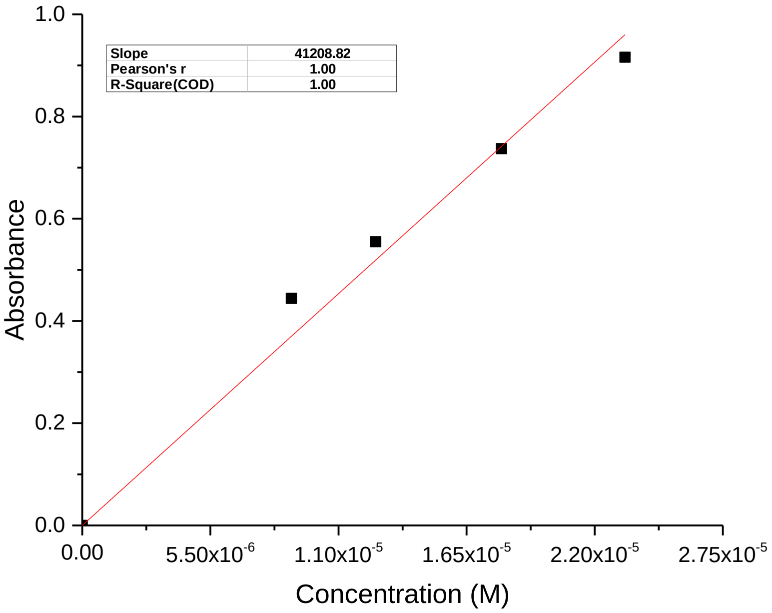

Figure 4.16. Absorbance versus Concentration plot of P-**3** at 505 nm in $CHCl_3$

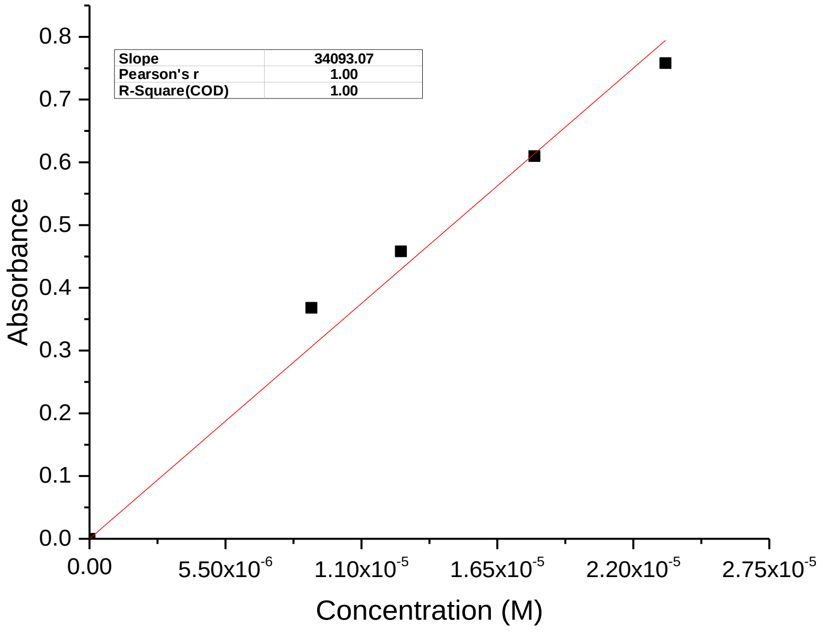

Figure 4.17. Absorbance versus Concentration plot of P-**3** at 484 nm in $CHCl_3$

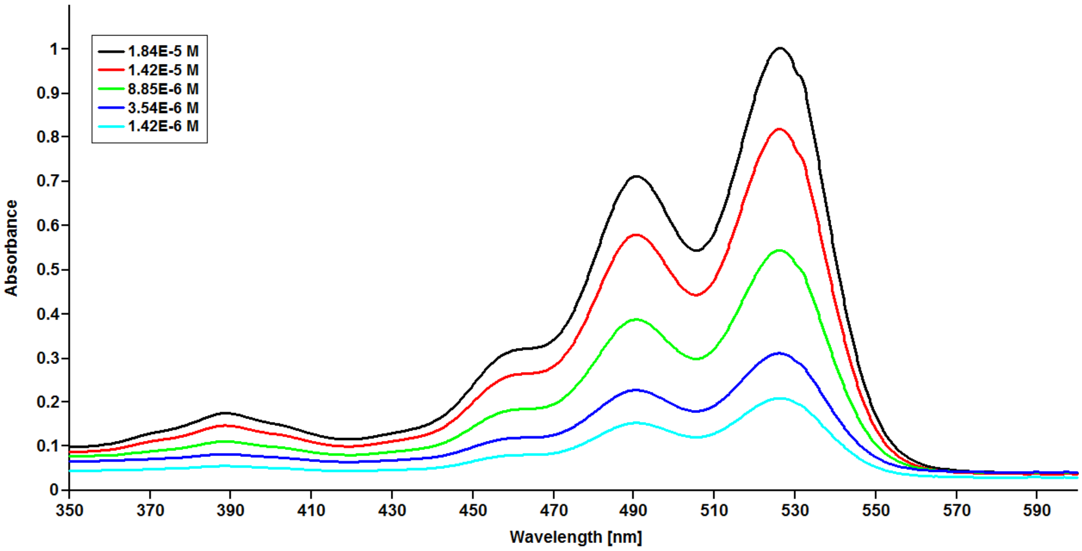

Figure 4.18. Absorption spectra of P-**4** in $CHCl_3$

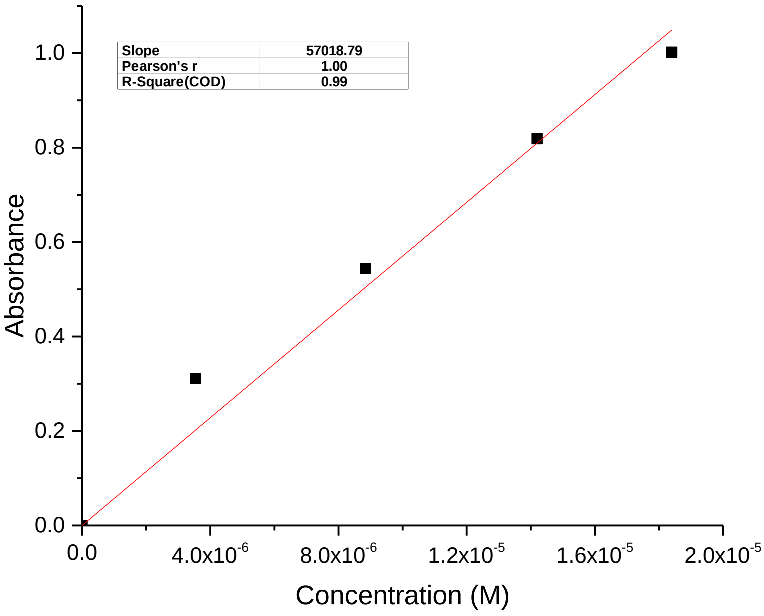

Figure 4.19. Absorbance versus Concentration plot of P-**4** at 526 nm in $CHCl_3$

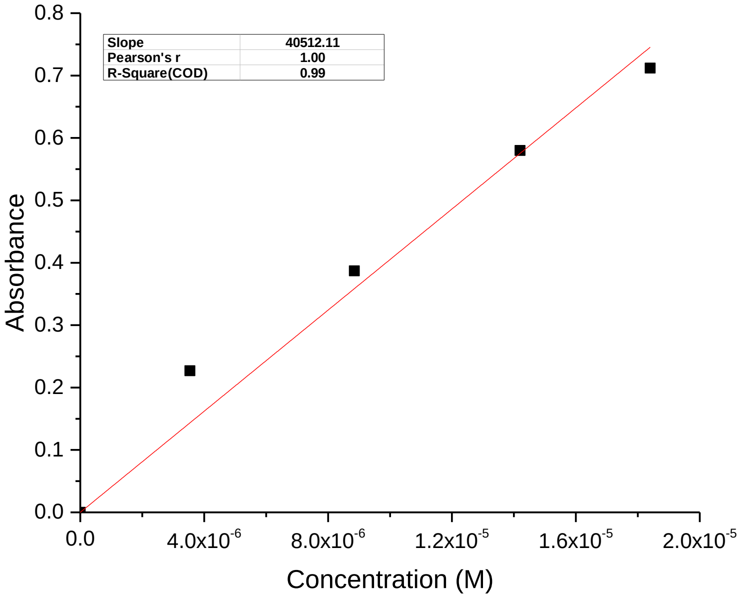

Figure 4.20. Absorbance versus Concentration plot of P-**4** at 491 nm in $CHCl_3$

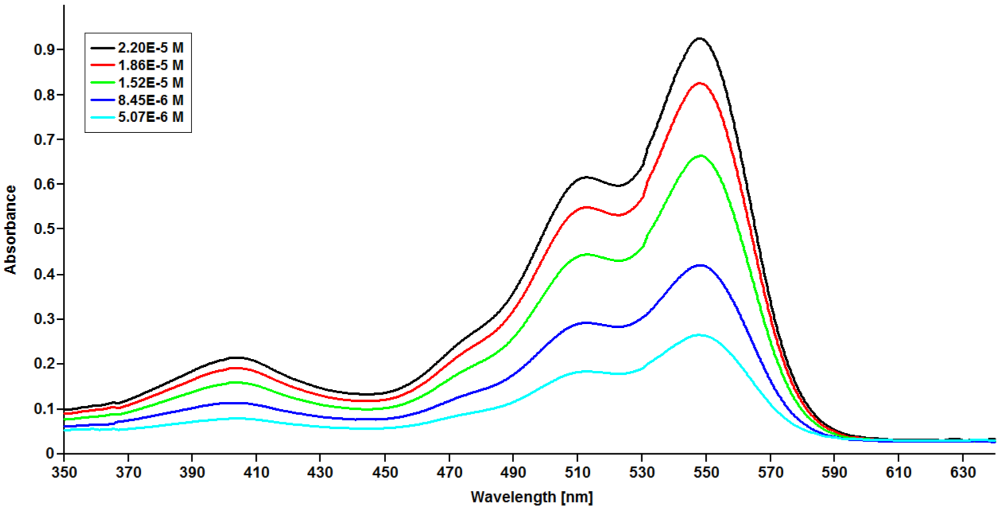

Figure 4.21. Absorption spectra of P-**5** in CHCl$_3$

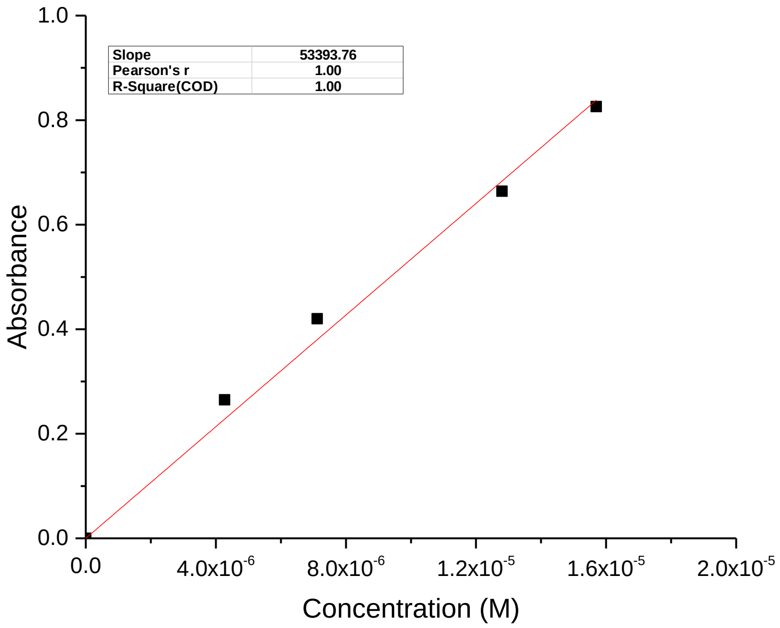

Figure 4.22. Absorbance versus Concentration plot of P-**5** at 548 nm in CHCl$_3$

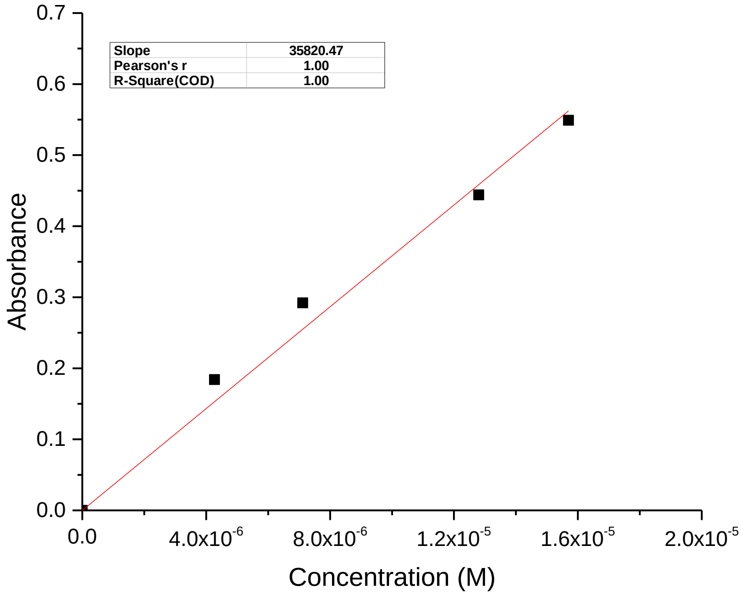

Figure 4.23. Absorbance versus Concentration plot of P-**5** at 512 nm in $CHCl_3$

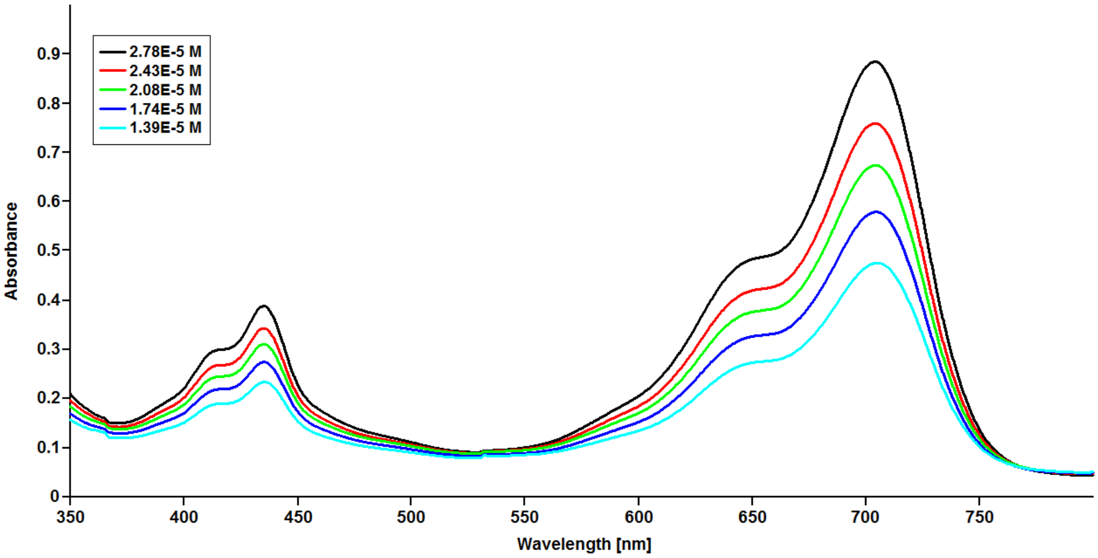

Figure 4.24. Absorption spectra of P-**6** in $CHCl_3$

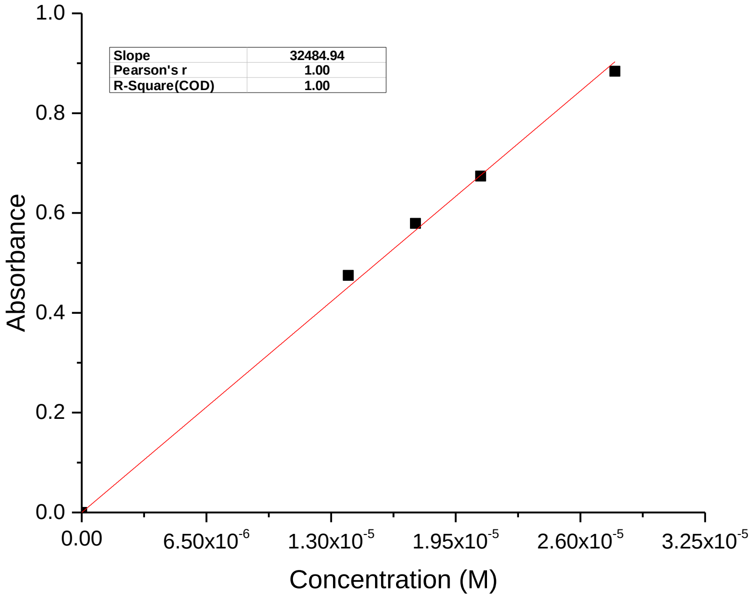

Figure 4.25. Absorbance versus Concentration plot of P-**6** at 704 nm in $CHCl_3$

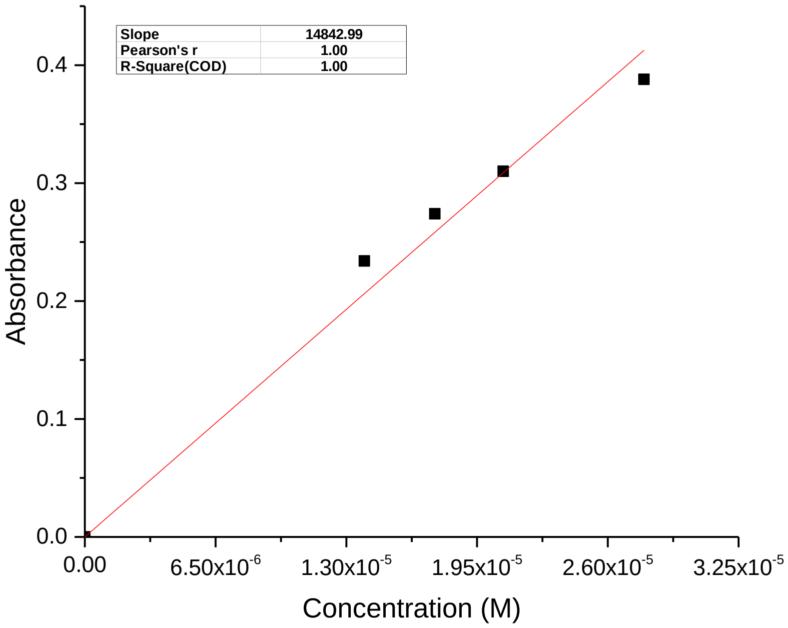

Figure 4.26. Absorbance versus Concentration plot of P-**6** at 435.6 nm in $CHCl_3$

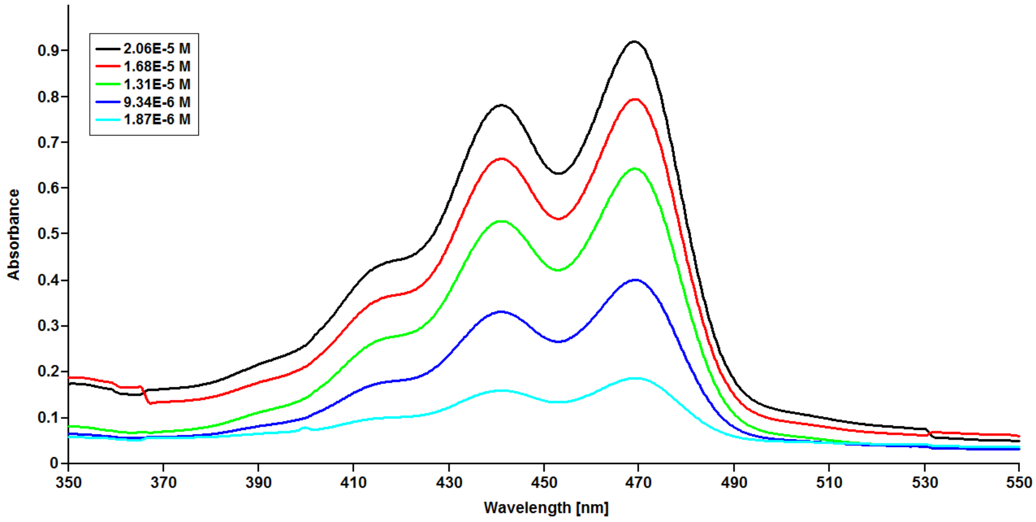

Figure 4.27. Absorption spectra of P-**1** in DMF

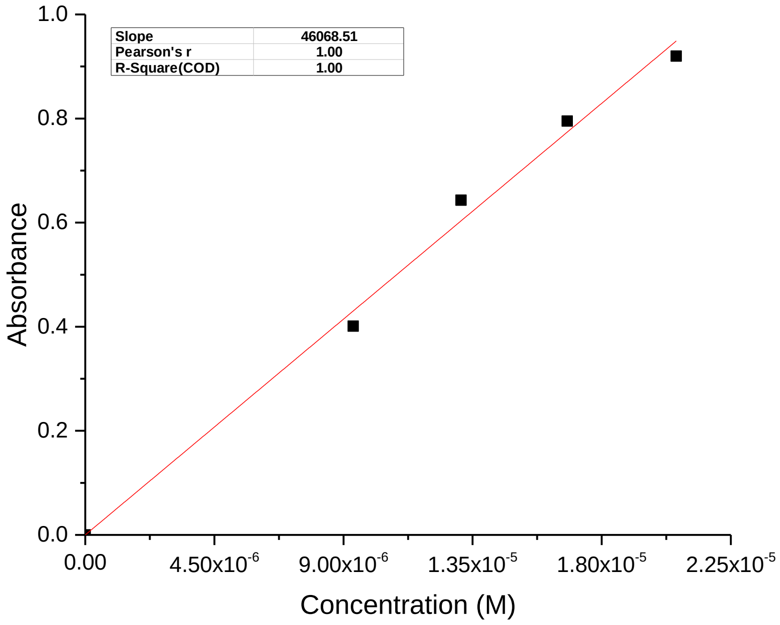

Figure 4.28. Absorbance versus Concentration plot of P-**1** at 469 nm in DMF

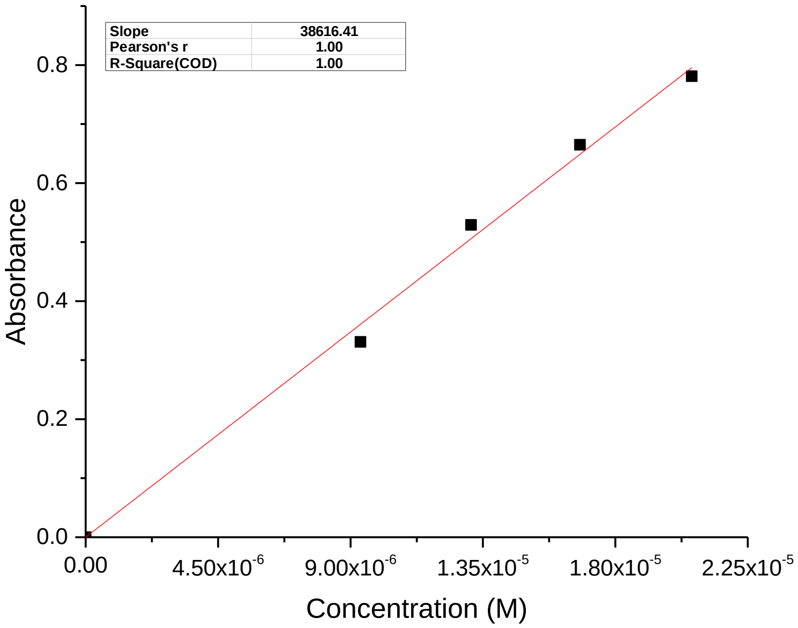

Figure 4.29. Absorbance versus Concentration plot of P-**1** at 441 nm in DMF

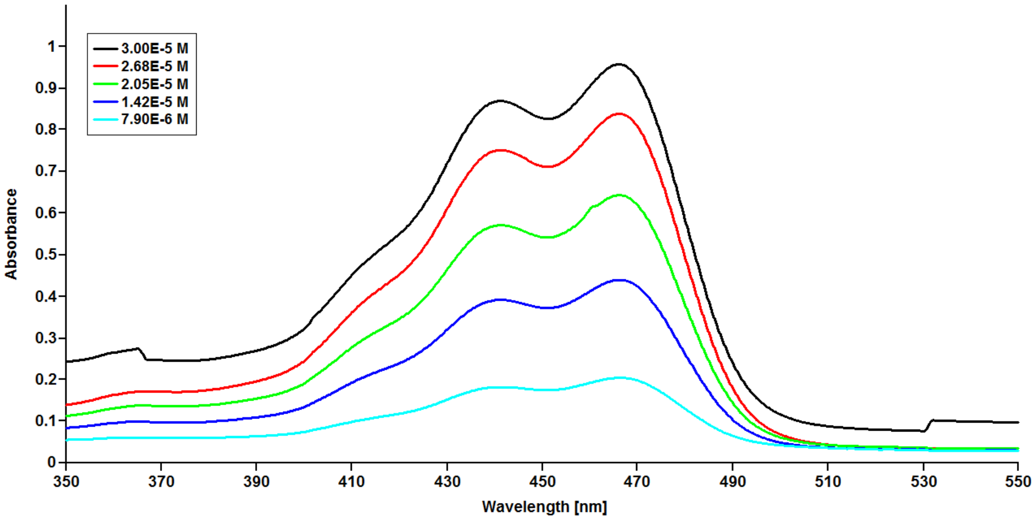

Figure 4.30. Absorption spectra of P-**2** in DMF

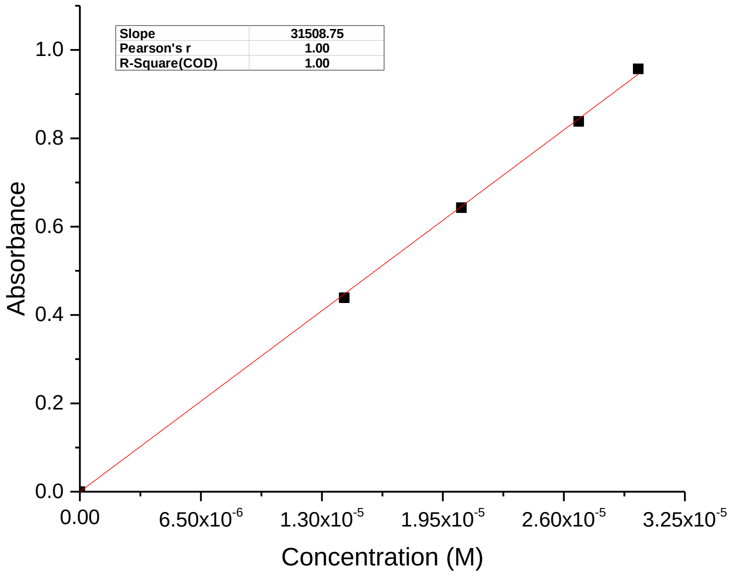

Figure 4.31. Absorbance versus Concentration plot of P-**2** at 466 nm in DMF

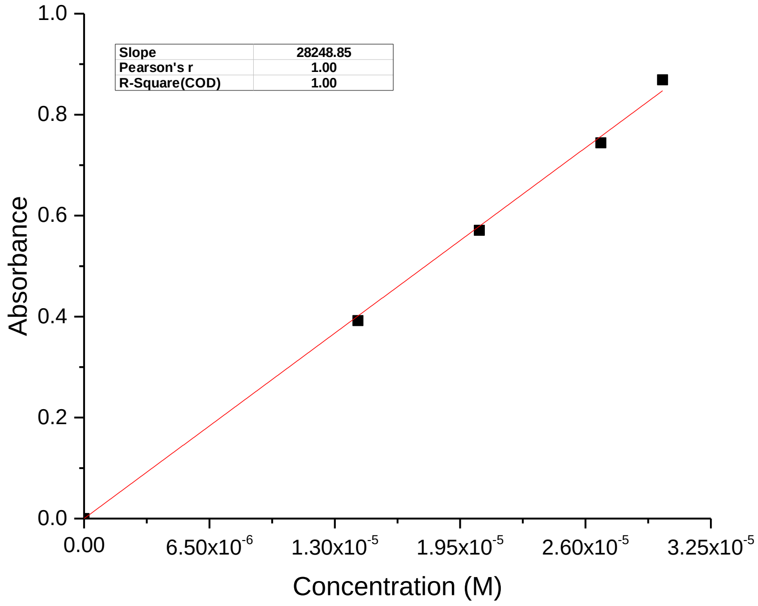

Figure 4.32. Absorbance versus Concentration plot of P-**2** at 441 nm in DMF

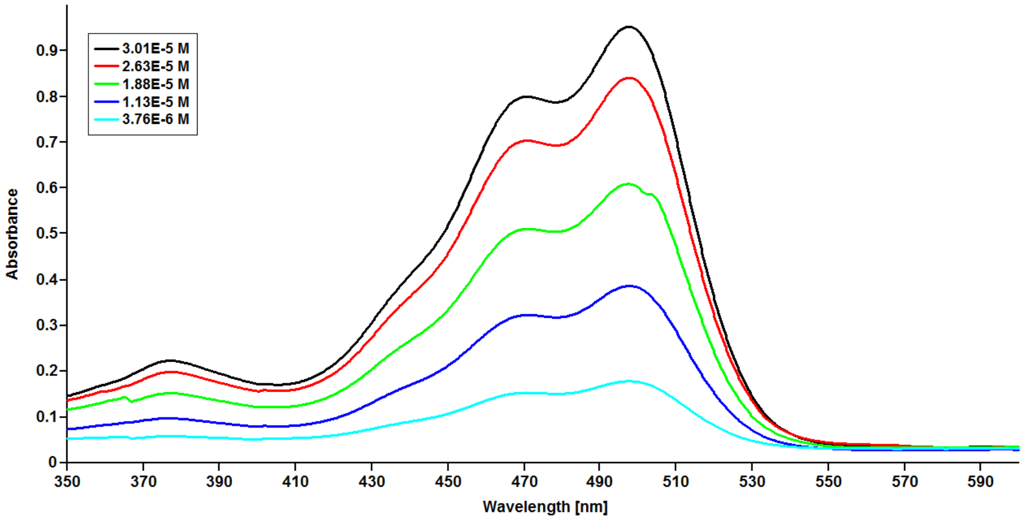

Figure 4.33. Absorption spectra of P-**3** in DMF

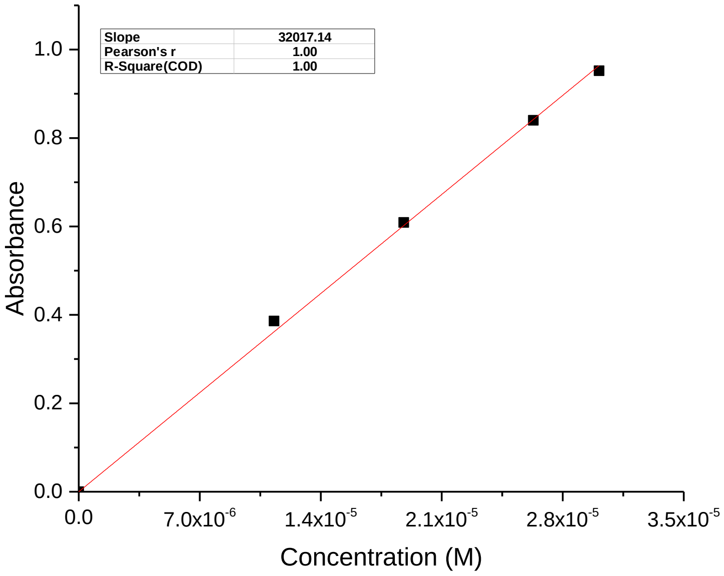

Figure 4.34. Absorbance versus Concentration plot of P-**3** at 497 nm in DMF

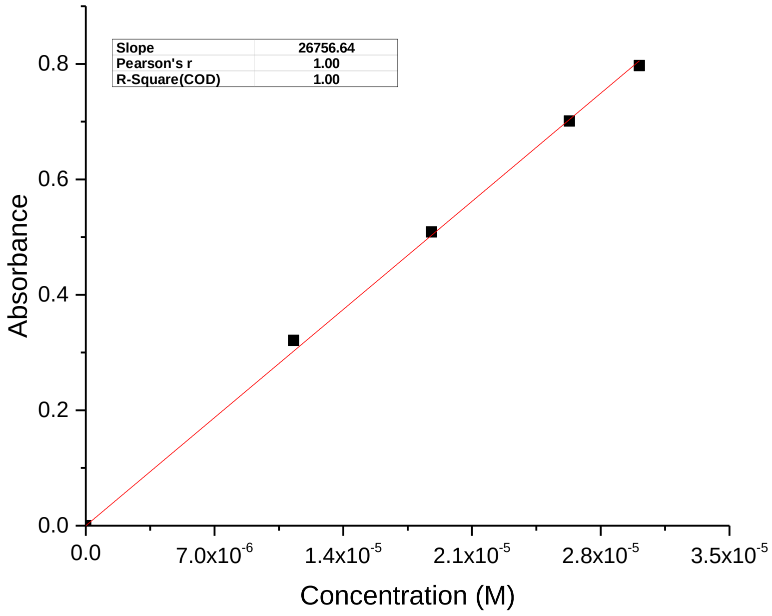

Figure 4.35. Absorbance versus Concentration plot of P-**3** at 469 nm in DMF

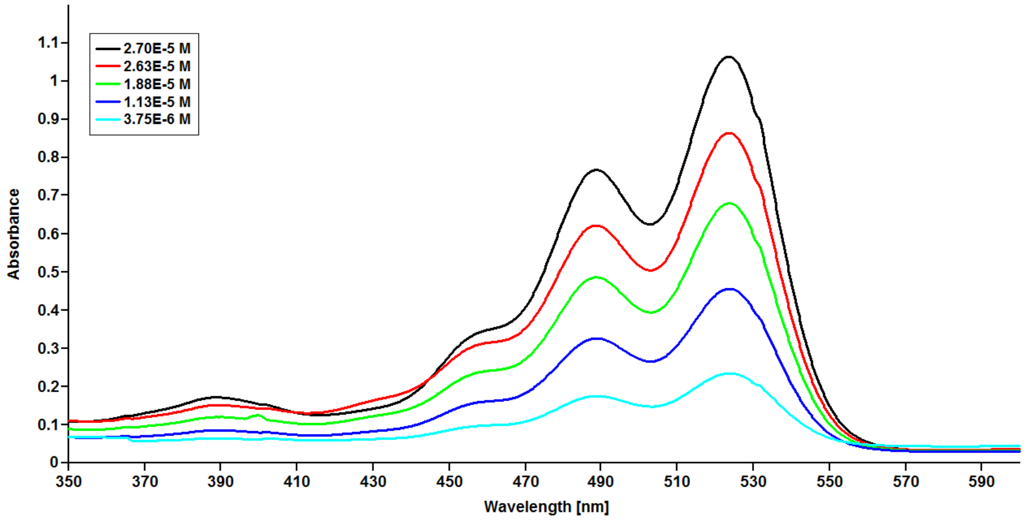

Figure 4.36. Absorption spectra of P-**4** in DMF

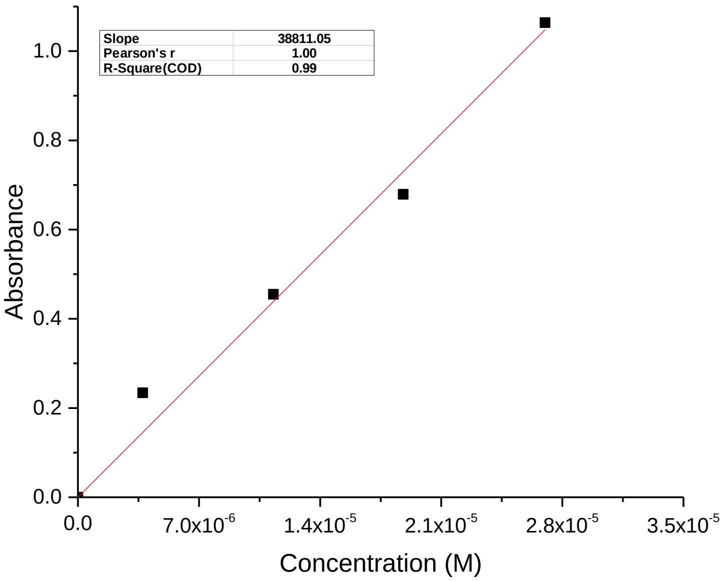

Figure 4.37. Absorbance versus Concentration plot of P-**4** at 523 nm in DMF

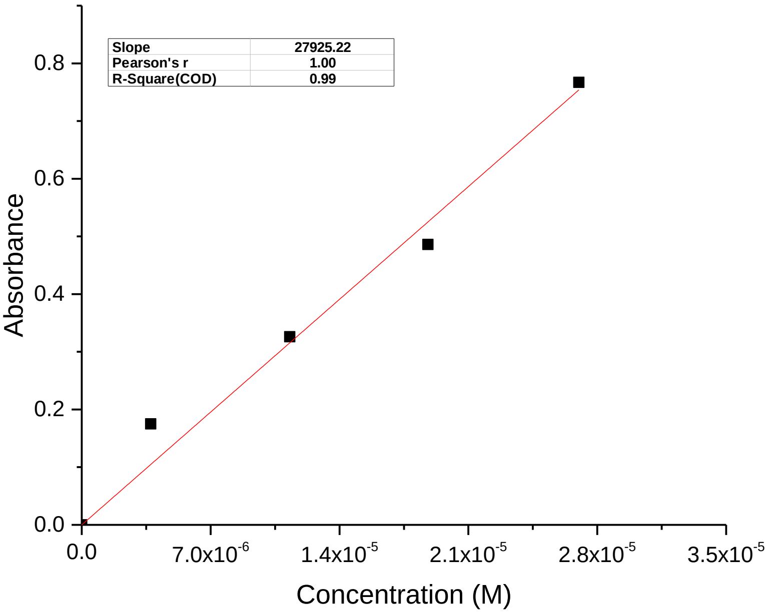

Figure 4.38. Absorbance versus Concentration plot of P-**4** at 488 nm in DMF

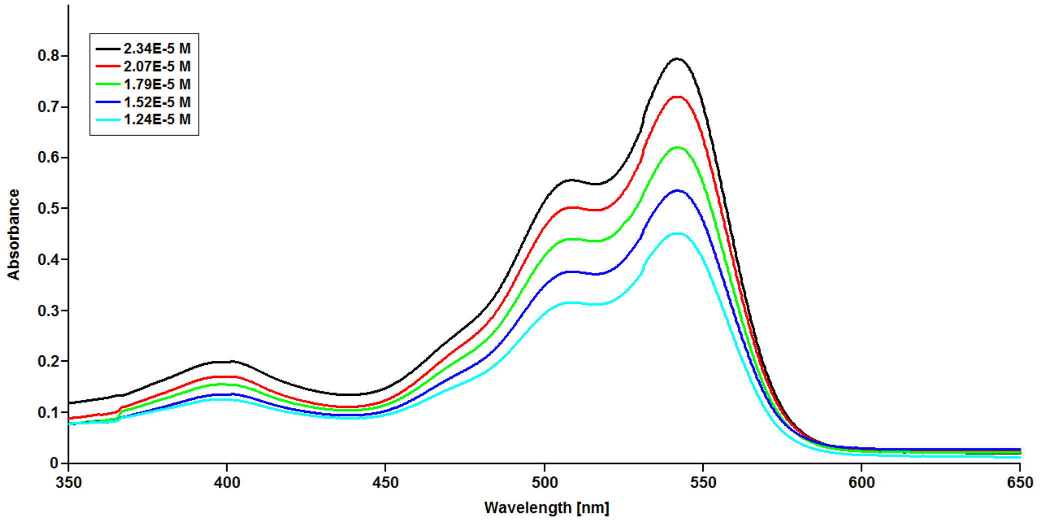

Figure 4.39. Absorption spectra of P-**5** in DMF

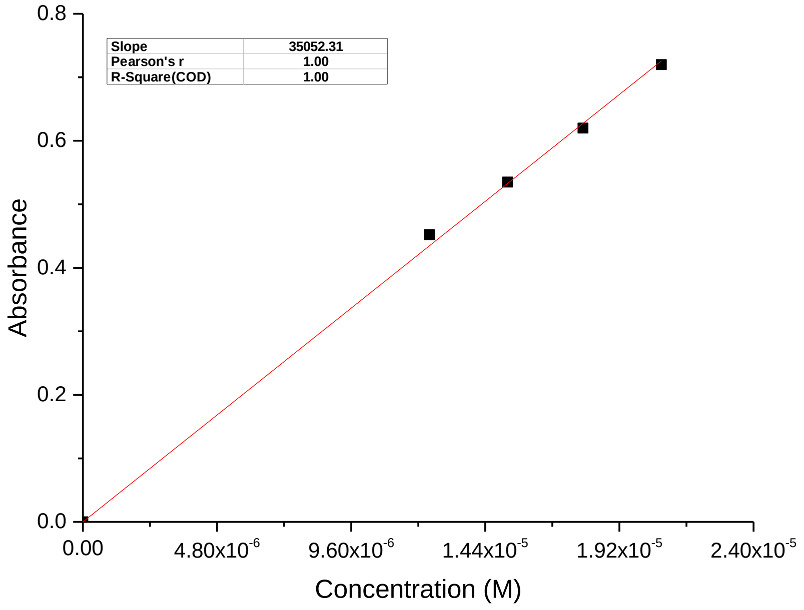

Figure 4.40. Absorbance versus Concentration plot of P-**5** at 541 nm in DMF

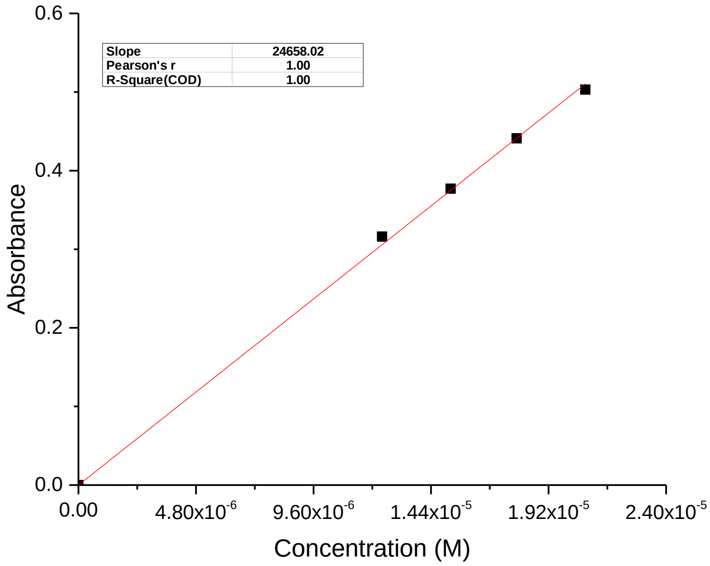

Figure 4.41. Absorbance versus Concentration plot of P-**5** at 508 nm in DMF

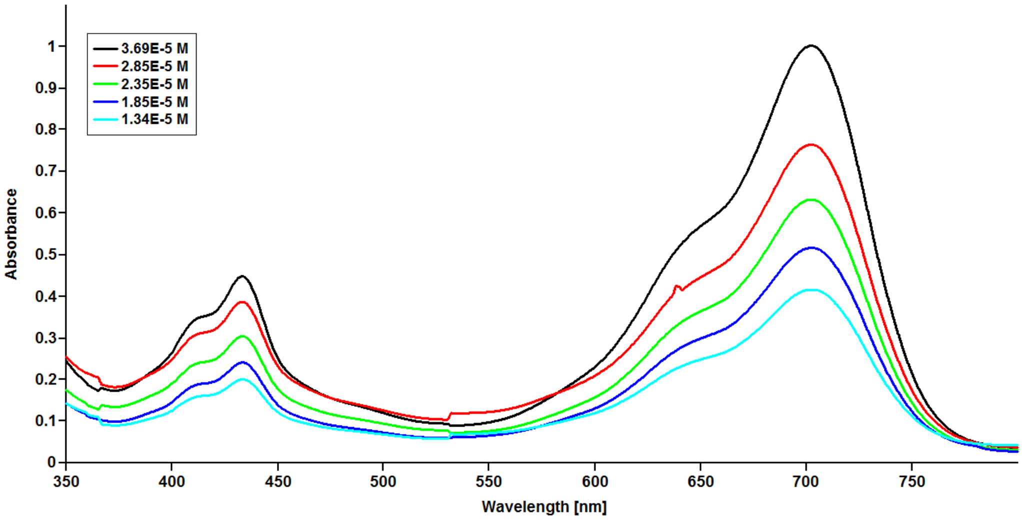

Figure 4.42. Absorption spectra of P-**6** in DMF

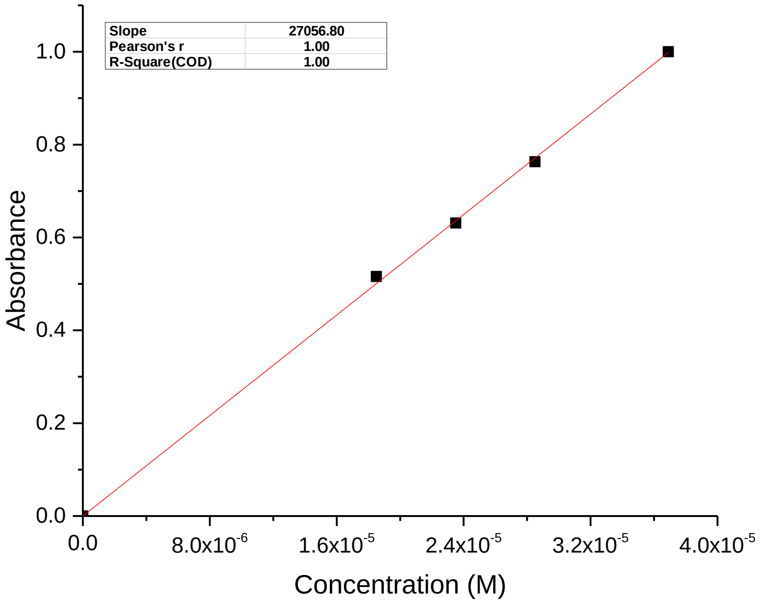

Figure 4.43. Absorbance versus concentration plot of P-**6** at 704 nm in DMF

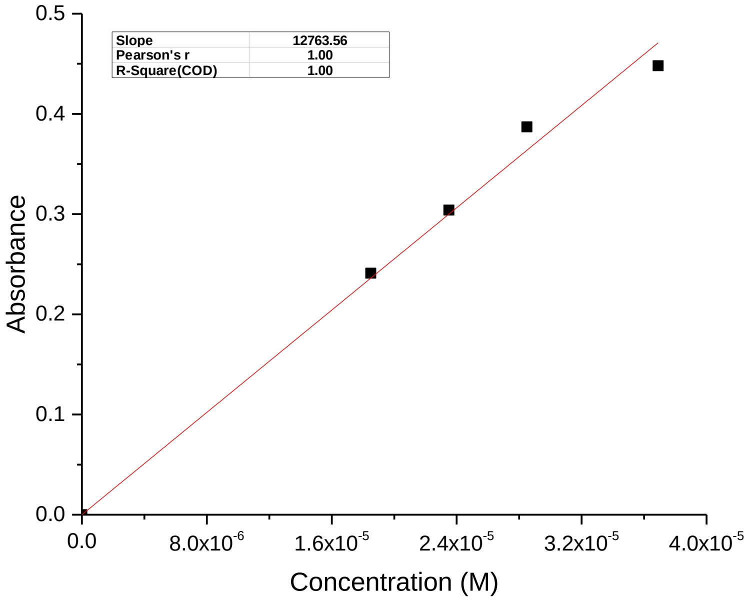

Figure 4.44. Absorbance versus concentration plot of P-**6** at 433 nm in DMF

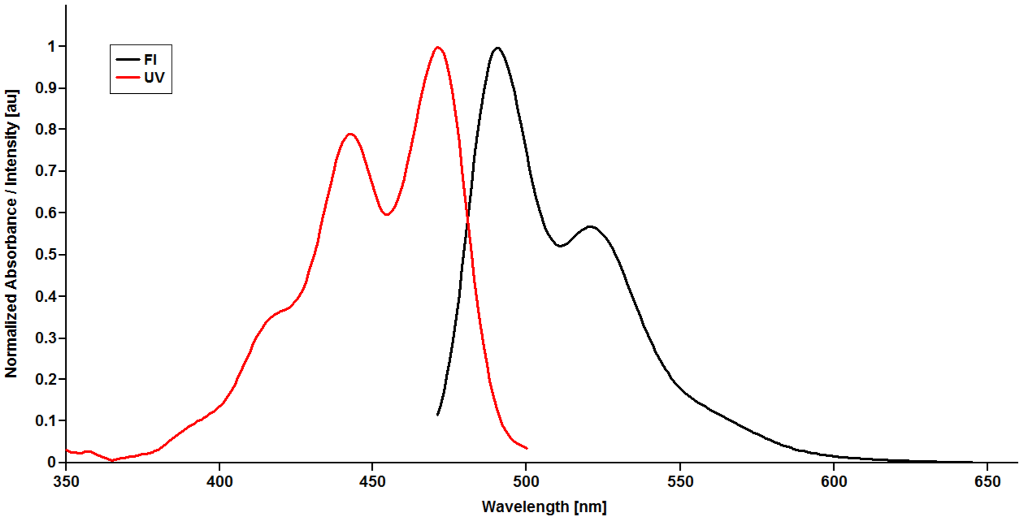

Figure 4.45. Normalized absorption and emission of P-**1** in $CHCl_3$

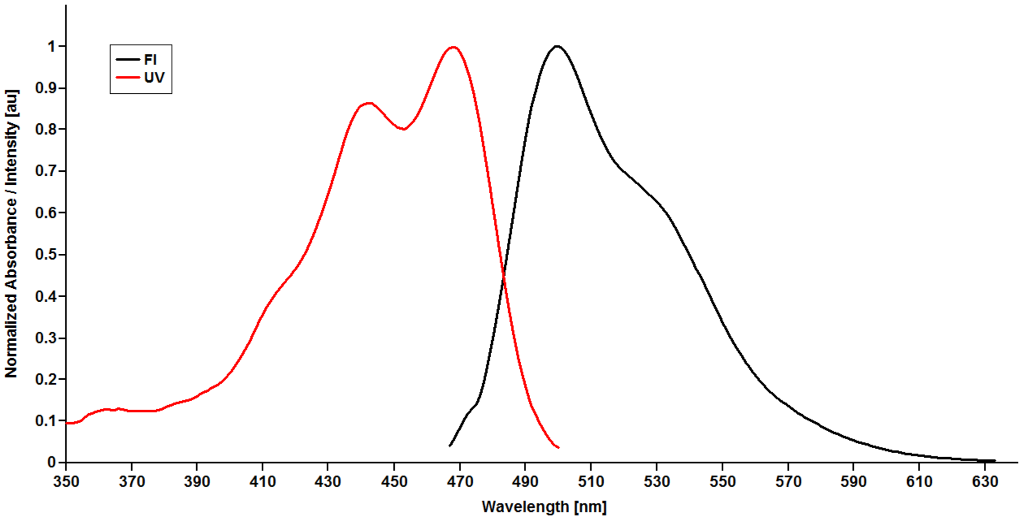

Figure 4.46. Normalized absorption and emission of P-**2** in $CHCl_3$

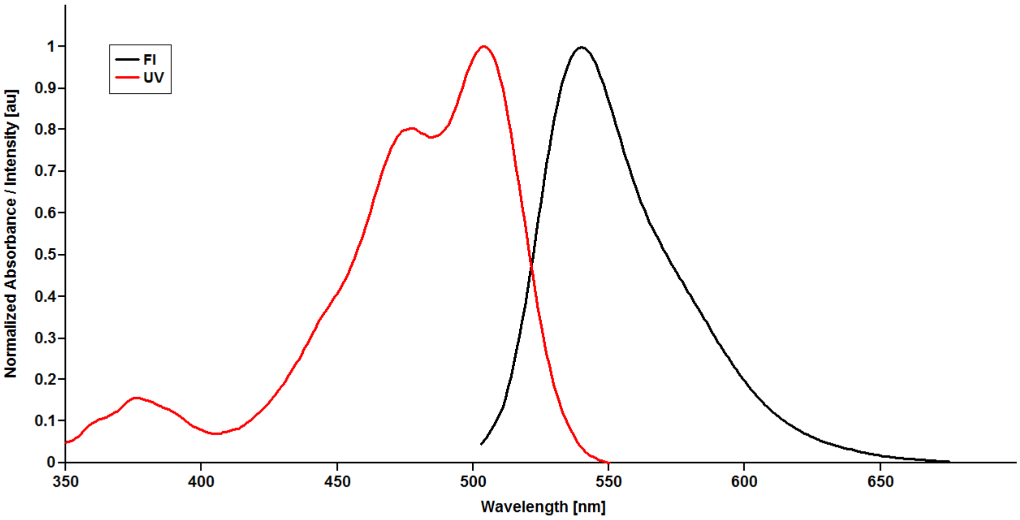

Figure 4.47. Normalized absorption and emission of P-**3** in $CHCl_3$

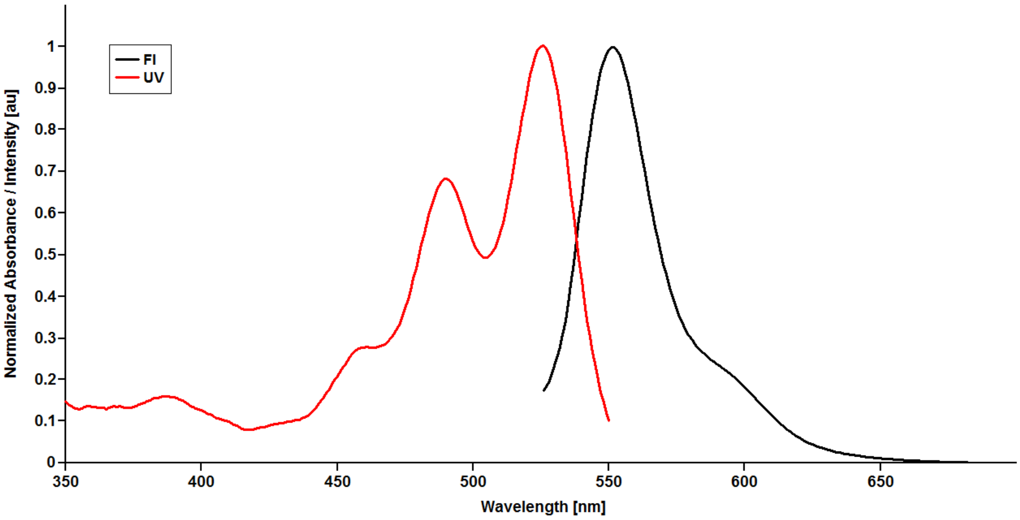

Figure 4.48. Normalized absorption and emission of P-**4** in $CHCl_3$

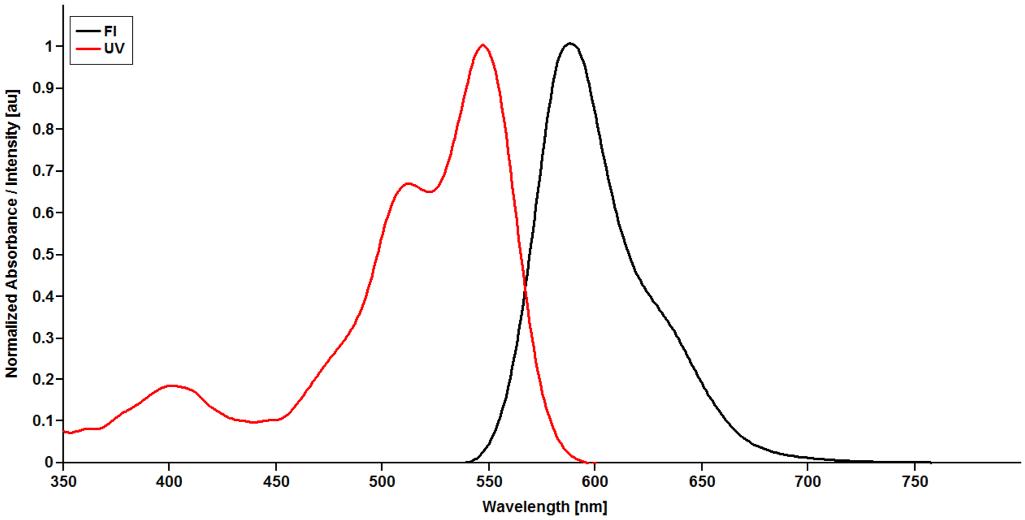

Figure 4.49. Normalized absorption and emission of P-**5** in $CHCl_3$

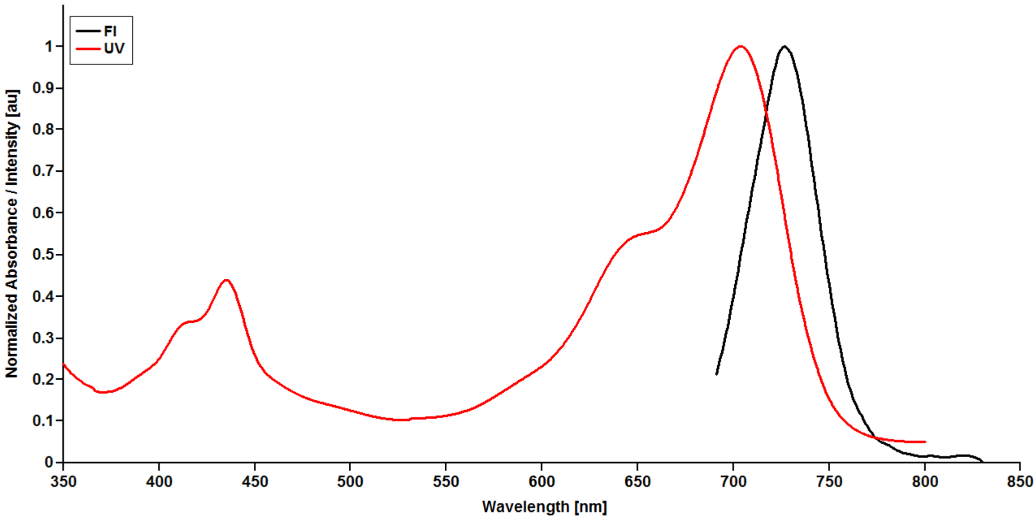

Figure 4.50. Normalized absorption and emission of P-**6** in $CHCl_3$

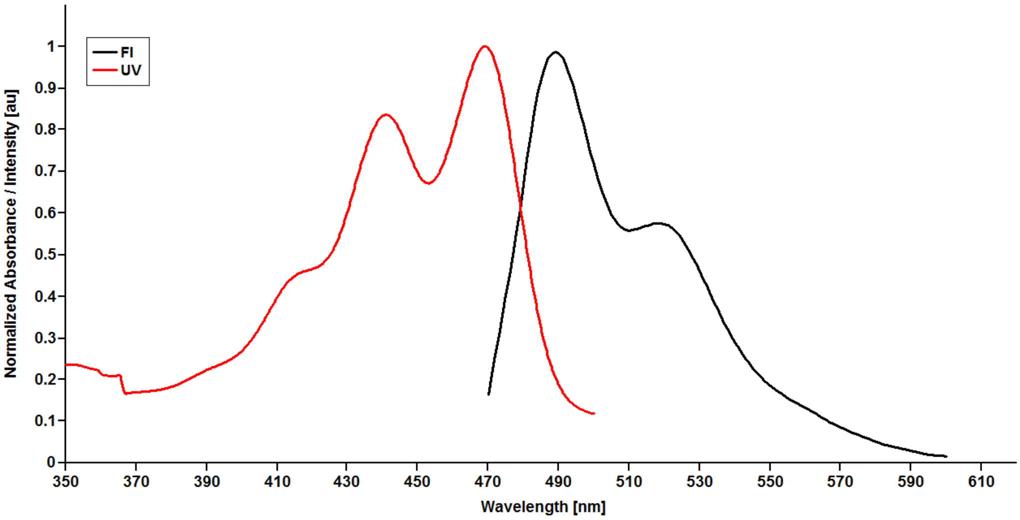

Figure 4.51. Normalized absorption and emission of P-**1** in DMF

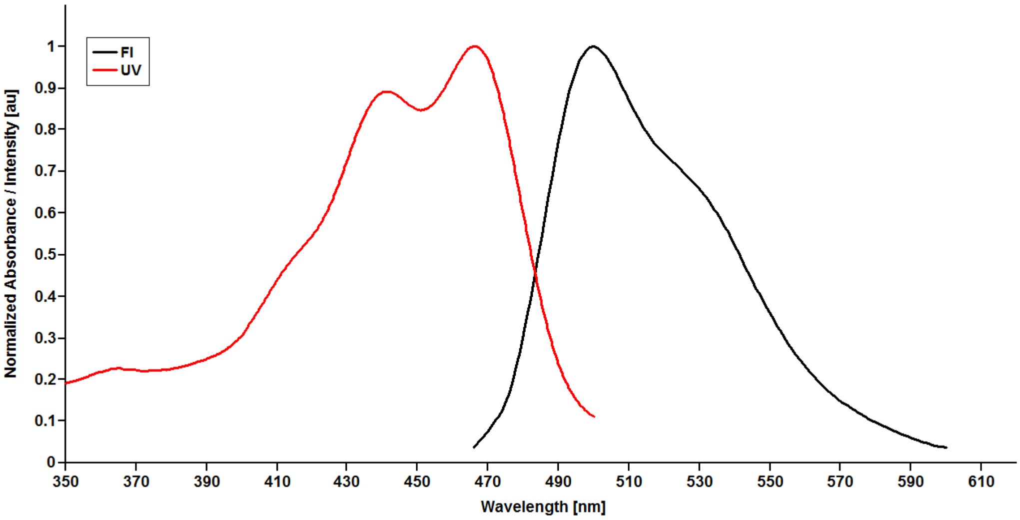

Figure 4.52. Normalized absorption and emission of P-**2** in DMF

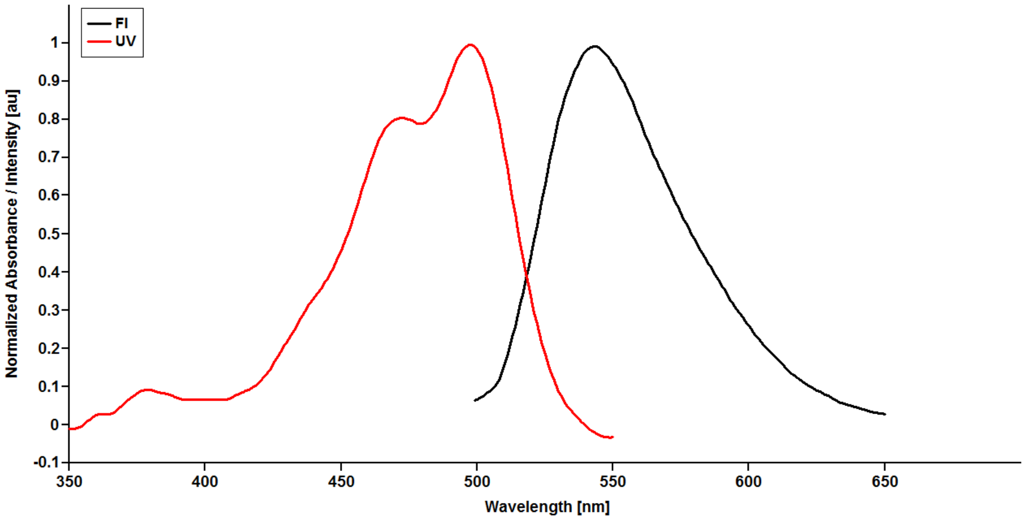

Figure 4.53. Normalized absorption and emission of P-**3** in DMF

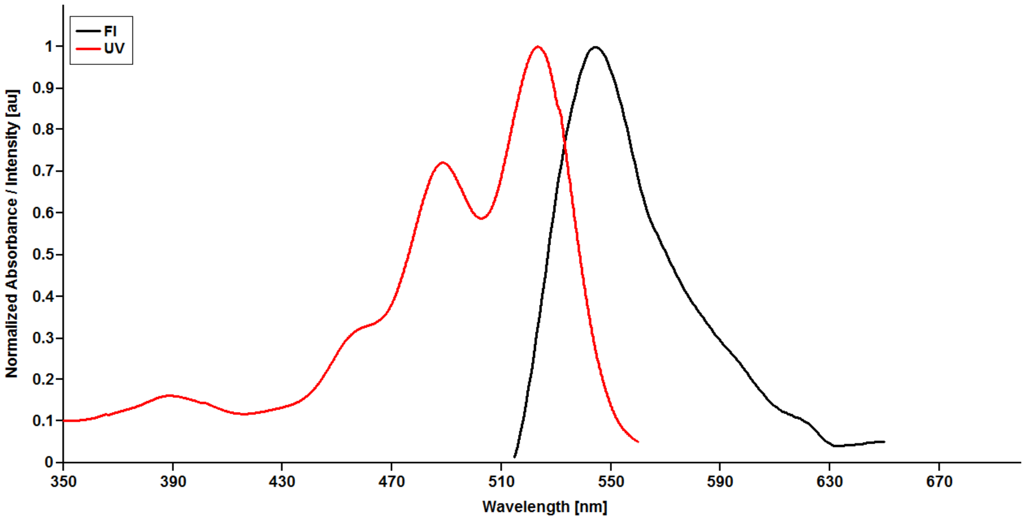

Figure 4.54. Normalized absorption and emission of P-**4** in DMF

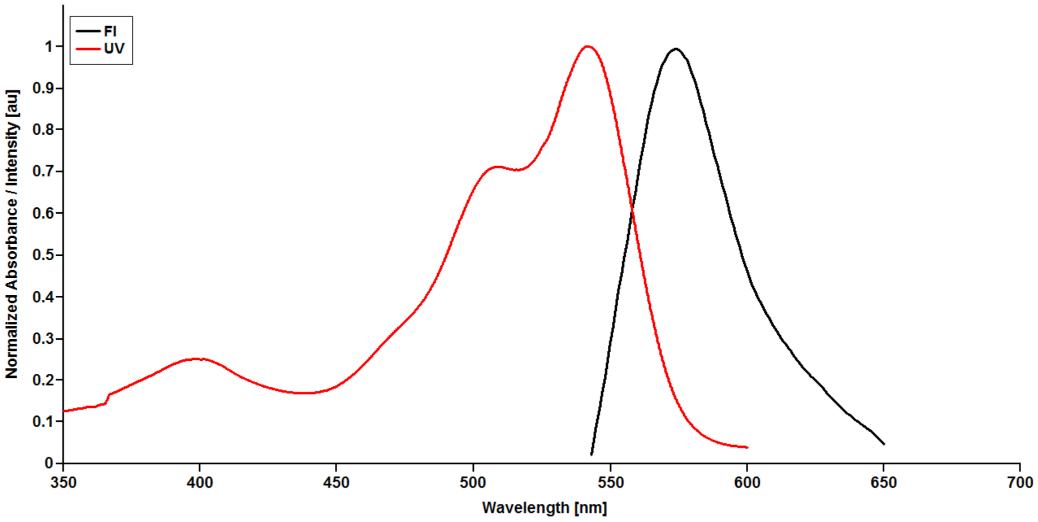

Figure 4.55. Normalized absorption and emission of P-**5** in DMF

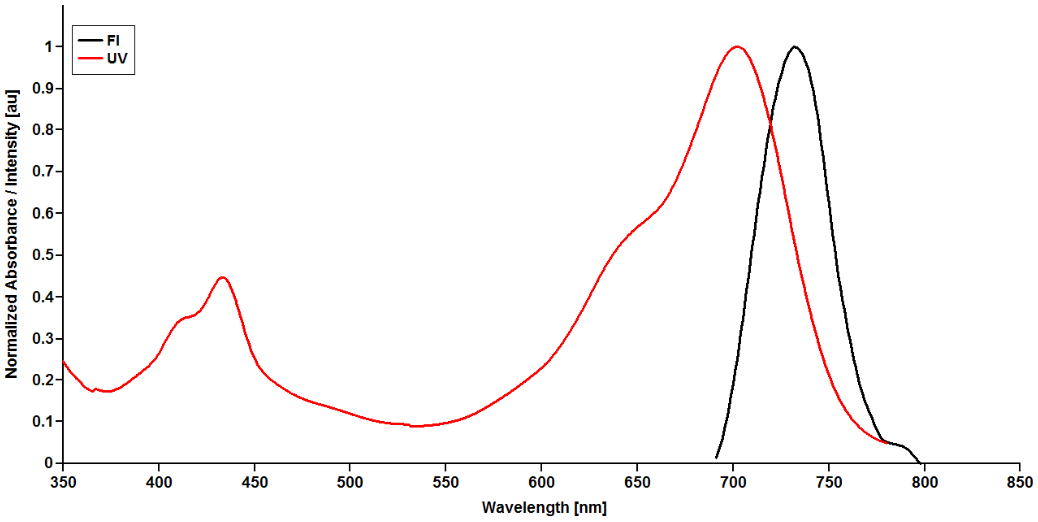

Figure 4.56. Normalized absorption and emission of P-**6** in DMF

4.3.3 Singlet Excitation Energies (E_s)

The minimum amount of energy required by a chromophore to get excited from the ground state to the excited state is known as Singlet Excitation Energy. A mathematical representation of Singlet Energy is expressed as [208]:

$$\mathrm{E_s} = \frac{2.86\times10^5}{\lambda_{\max}} \tag{5.2}$$

Where $\mathrm{E_s}$ is the singlet energy (kcal mol^{-1}), $\lambda_{\max}$ is the maximum absorption wavelength (Å). The singlet energies for the selected compounds calculated using equation (5.2) is shown in Table 4.1

Table 4.1. Singlet Excitation Energies for the selected compounds

Analysis	**Compound**					
	P-**1**	P-**2**	P-**3**	P-**4**	P-**5**	P-**6**
			Solvent: $CHCl_3$			
$\lambda_{\max}$ (Å)	4720	4680	5050	5260	5480	7040
E_s (kcal mol^{-1})	60.59	61.11	56.63	54.37	52.19	40.63
			Solvent: DMF			
$\lambda_{\max}$ (Å)	4690	4660	4970	5230	5410	7040
E_s (kcal mol^{-1})	60.98	61.37	57.55	54.68	52.87	40.63

4.3.4 Oscillator Strength (*f*)

Oscillator strength is a dimensionless quantity used to measure the relative strength of an electronic transition within an atomic and molecular system. A mathematical representation of Oscillator strength is expressed as [208]:

$$f = 4.32 \times 10^{-9} \Delta\bar{v}_{1/2}\, \varepsilon_{\max} \tag{5.3}$$

Where f is the oscillator strength, $\Delta\bar{v}_{1/2}$ is the half-width of an absorption (cm^{-1}), and $\varepsilon_{\max}$ is the maximum extinction coefficient at a certain absorption wavelength (L$^{\cdot}$ mol^{-}

$^{1}\cdot$ cm^{-1}). A schematic representation of the half-width selected for a specific absorption is given in Figure 4.57.

The half-width of an absorption ($\Delta\bar{v}_{1/2}$) represents the full or half-width of the maximum intensity curve, which is calculated as:

$$\Delta\bar{v}_{1/2} = \bar{v}_I - \bar{v}_{II} \tag{5.4}$$

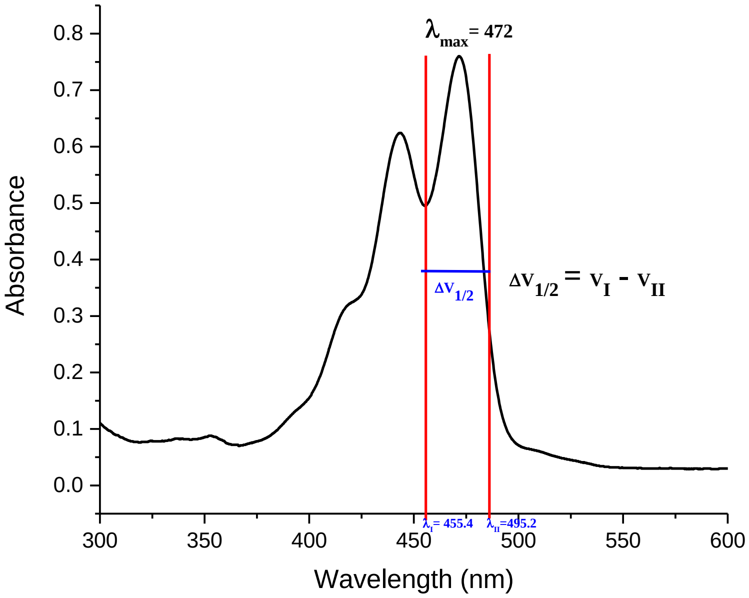

Figure 4.57. Representation of the Half-Width for P-**1** at 472 nm

From Figure 4.57, λ_I = 455.4 nm

Thus, λ_I = 455.4 nm × $\frac{10^{-9}}{1\,nm} \times \frac{1\,cm}{10^{-2}m} = 4.55 \times 10^{-5}$cm

$\bar{v}_I = \frac{1}{4.55\times10^{-5}}$ = 21,958.72 cm^{-1}

Also, λ_{II} = 486.4 nm

λ_{II} = 486.4 nm × $\frac{10^{-9}}{1\,nm} \times \frac{1\,cm}{10^{-2}m} = 4.86 \times 10^{-5}$cm

$\bar{\nu}_{\mathrm{II}} = \frac{1}{4.86\times10^{-5}}$ = 20,599.21 cm^{-1}

$\Delta\bar{\nu}_{1/2}$ = 22,011.89 cm^{-1} - 20,599.21 cm^{-1} = **1,399.51 cm^{-1}**

Using the aforementioned procedure, the half-width for remaining selected compounds is estimated in Table 4.2.

Table 4.2. Half-Width Estimation for the Selected Compounds

Compound	$\boldsymbol{\lambda_{\mathrm{max}}}$ (nm)	$\boldsymbol{\lambda_{\mathrm{I}}}$ (nm)	$\boldsymbol{\lambda_{\mathrm{II}}}$ (nm)	$\boldsymbol{\bar{\nu}_I}$ (cm^{-1})	$\boldsymbol{\bar{\nu}_{\mathrm{II}}}$ (cm^{-1})	$\boldsymbol{\Delta\bar{\nu}_{1/2}}$ (cm^{-1})
Solvent: $CHCl_3$						
P-**1**	472	455.40	486.40	21,958.72	20,599.21	1,399.51
P-**2**	468	451.81	484.64	22,133.20	20,633.87	1,499.33
P-**3**	505	486.08	524.35	20,572.75	19,071.23	1,501.51
P-**4**	526	505.27	541.69	19,791.40	18,460.74	1,330.66
P-**5**	548	522.61	566.42	19,134.73	17,654.74	1,479.98
P-**6**	704	665.05	730.50	15,036.46	13,689.25	1,347.21
Solvent: DMF						
P-**1**	469	453.00	483.40	22,075.06	20,686.80	1,388.25
P-**2**	466	451.60	482.00	22,143.49	20,746.89	1,396.60
P-**3**	497	480.60	519.70	20,807.32	19,241.87	1,565.45
P-**4**	523	505.10	540.30	19,798.06	18,508.24	1,289.82
P-**5**	541	520.70	555.70	19,204.92	17,995.32	1,209.60
P-**6**	704	664.60	734.00	15,046.64	13,623.98	1,422.67

4.3.5 Theoretical Radiative Lifetimes ($\boldsymbol{\tau_0}$)

In the absence of radiationless transitions, there is a theoretical lifetime of an excited molecule known as Theoretical Radiative Lifetime, expressed as [208]:

$$\tau_0 = \frac{3.5\times10^{8}}{\bar{\nu}^2{}_{max}\times\varepsilon_{max}\times\Delta\bar{\nu}_{1/2}} \qquad (5.5)$$

Where τ_0 is the theoretical radiative lifetime (ns), $\bar{\nu}_{max}$ is the mean frequency of the maximum absorption band (cm^{-1}), ε_{max} is the maximum extinction coefficient at a certain absorption wavelength ($L \cdot mol^{-1} \cdot cm^{-1}$) and $\Delta\bar{\nu}_{1/2}$ is the half-width of an absorption (cm^{-1}).

From Figure 4.57, λ_{max} = 472 nm

Thus, $\lambda_{max} = 472\ nm \times \frac{10^{-9}}{1\ nm} \times \frac{1\ cm}{10^{-2} m} = 4.72 \times 10^{-5} cm$

$\bar{\nu}_{max} = \frac{1}{4.72\times10^{-5}} = 21{,}186.44\ cm^{-1}$

$\bar{\nu}^2{}_{max} = (21{,}186.44\ cm^{-1})^2 = 4.49\times10^8\ cm^{-2}$

From equation (5.5), the theoretical radiative lifetime is calculated as:

$\tau_0 = \frac{3.5\times10^8}{4.49\times10^8\times29{,}974\ \times1{,}399.51} = \mathbf{18.60\ ns}$

Using the aforementioned algorithm, the theoretical radiative lifetime of the remaining compounds are shown in Table 4.3.

Table 4.3. Theoretical Radiative Lifetime of Compounds

Compounds	P-**1**	P-**2**	P-**3**	P-**4**	P-**5**	P-**6**
Solvent: $CHCl_3$						
$\bar{\nu}^2{}_{max}$ (cm^{-2})	4.49×10^8	4.57×10^8	3.92×10^8	3.61×10^8	3.33×10^8	2.02×10^8
$\Delta\bar{\nu}_{1/2}$ (cm^{-1})	1,399.51	1,499.33	1,501.51	1,330.66	1,479.98	1,347.21
ε_{max} ($M^{-1}\ cm^{-1}$)	29,974	32,362	41,209	57,019	53,394	32,485
τ_0(ns)	18.60	15.80	14.40	12.80	13.30	39.60
Solvent: DMF						
$\bar{\nu}^2{}_{max}$ (cm^{-2})	4.55×10^8	4.60×10^8	4.05×10^8	3.66×10^8	3.42×10^8	2.02×10^8
$\Delta\bar{\nu}_{1/2}$ (cm^{-1})	1,388.25	1,396.60	1,565.45	1,289.82	1,209.60	1,422.67
ε_{max} ($M^{-1}\ cm^{-1}$)	23,837	31,509	32,017	38,811	35,052	27,057
τ_0(ns)	23.30	17.30	17.20	19.10	24.10	45.00

4.3.6 Optical Band Gap Energy (E_g)

The optical band gap energies of the compounds are calculated using their absorption spectral by extrapolating the maximum absorption band to zero absorbance with the corresponding wavelength following equation (5.6):

$$E_{\mathrm{g}} = \frac{1240\ \mathrm{eV\ nm}}{\lambda} \tag{5.6}$$

Where E_{g} is the band gap energy in eV, and λ is the cut-off wavelength of the absorption band in nm.

From Figure 4.58, λ = 770 nm

Thus, $E_{\mathrm{g}} = \frac{1240\ \mathrm{eV\ nm}}{770\ \mathrm{nm}}$ =**1.61 eV**

Table 4.4 shows the various cut-off wavelength of the compounds while Figure shows the representation cut-off wavelength for P-**6** at 770 nm in DMF.

Table 4.4. Cut-off wavelength of Compounds

Compounds	P-**1**	P-**2**	P-**3**	P-**4**	P-**5**	P-**6**
Solvent: $CHCl_3$						
$\lambda_{0\rightarrow0}$ (nm)	494	497	542	555	582	756
Solvent: DMF						
$\lambda_{0\rightarrow0}$ (nm)	491	495	534	554	576	770

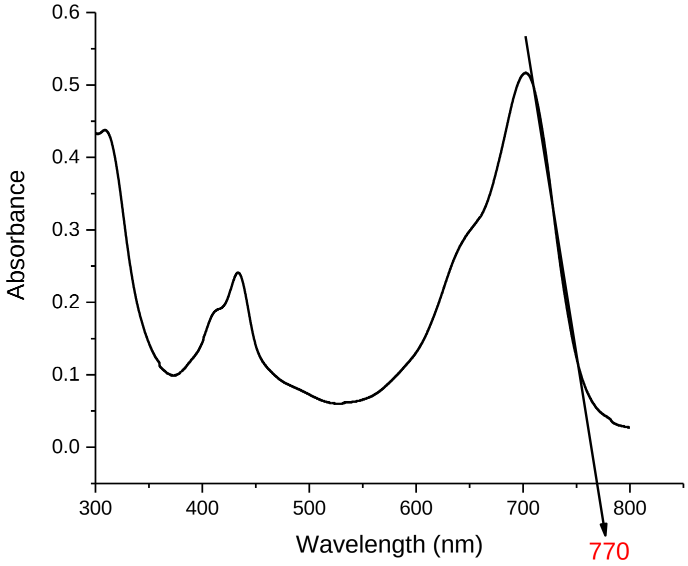

Figure 4.58. Cut-off Wavelength for P-**6** at 770 nm in DMF

4.3.7 Fluorescence Quantum Yield (Φ_F)

When light photons are absorbed by a fluorophore, an excited state is formed depending on the nature of the compound and its surroundings, nonetheless, the excitation ends in loss of energy (deactivation) and returns to ground state. Figure 4.59 shows a typical Jablonski diagram indicating all the processes of a fluorophore during excitation state. The ideal processes involve the loss of energy by the emission of a photon (fluorescence), internal conversion and vibrational relaxation (non-radiative loss of energy as heat to the surroundings), and intersystem crossing to the triplet manifold and subsequent non-radiative deactivation [209].

Fluorescence quantum yield (Φ_F) is defined as the ratio of photons emitted through fluorescence to the photons absorbed. In addition, information on the probability of an excited state being deactivated by fluorescence in contrast to the non-radiative mechanism is provided by the quantum yield.

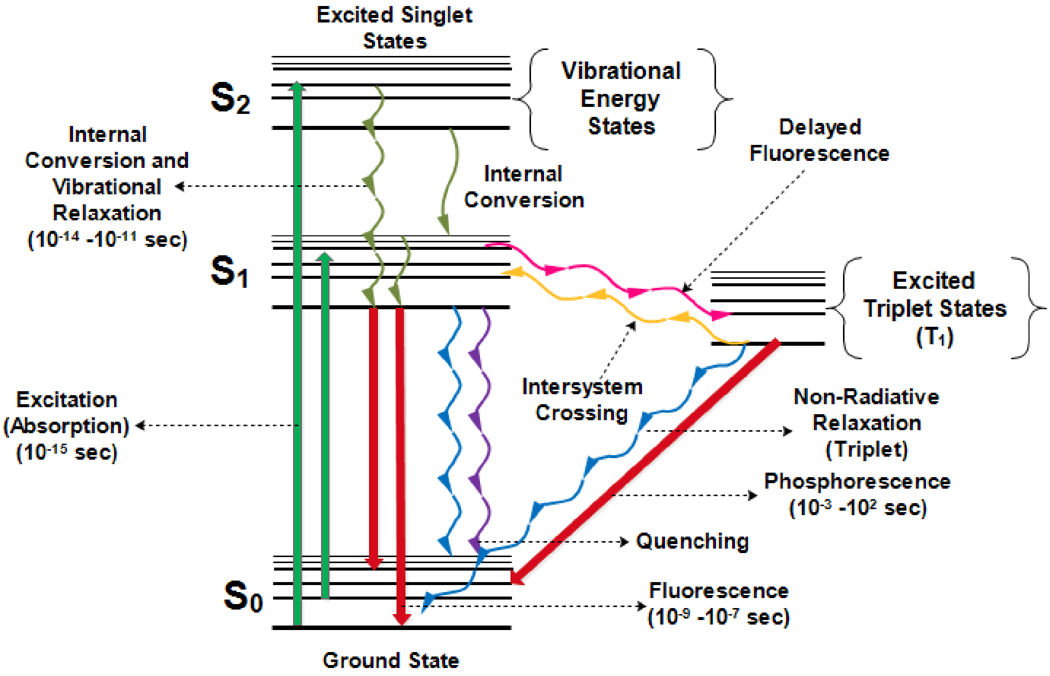

Figure 4.59. Typical Jablonski Diagram

The accuracy in the calculation of quantum yield for novel compounds is essential. Against the backdrop, the study employs the comparative method of Williams, Winfield [210], the most reliable method for recording quantum yield. The method involves the use of a well-characterized standard sample with a known quantum yield. Subsequently, solutions of the standard and test samples with the same absorbance and excitation wavelength is assumed to absorb the same number of photons. Accordingly, the ratio of the quantum yield values can be derived by a simple ratio of the integrated fluorescence intensities of the two solutions recorded under the same conditions. $\boldsymbol{\Phi_F}$ of the test samples is calculated as:

$$\boldsymbol{\Phi_u} = \boldsymbol{\Phi_{st}}\left(\frac{Grad_u}{Grad_{st}}\right)\left(\frac{\eta_u^2}{\eta_{st}^2}\right) \tag{5.7}$$

Where $\boldsymbol{\Phi_u}$ is the fluorescence quantum yield of the unknown sample, $\boldsymbol{\Phi_{st}}$ is the fluorescence quantum yield of the standard sample, $Grad_u$ is the gradient from the plot of integrated fluorescence intensity versus absorbance of the unknown, $Grad_{st}$ is the gradient from the plot of integrated fluorescence intensity versus absorbance of the standard sample (Figure 4.60), η_u is the refractive index of the solvent for the unknown sample and, η_{st} is the refractive index of the solvent for the standard sample.

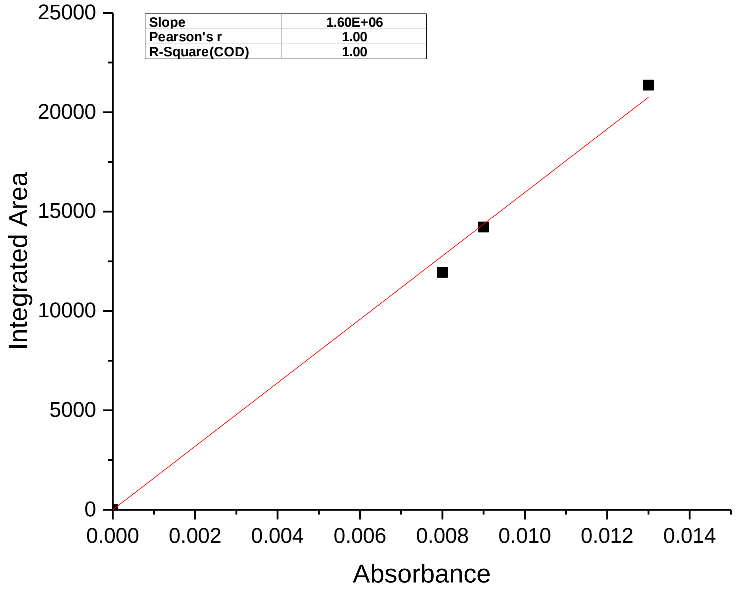

Figure 4.60. Gradient of Standard Sample

N,N'-bis(2,6-diisopropylphenyl)-perylene-3,4,9,10-tetracarboxdiimide with a $\boldsymbol{\Phi_F}$ = 100% in $CHCl_3$ was used as the standard sample for the quantum yield measurements of P-**4**, P-**5** and P-**6**. The emissions spectra for the standard and test samples was taken at the same wavelength, $\boldsymbol{\lambda_{exc}}$= 460 nm.

From equation (5.7), the quantum yield of P-**4** was calculated as:

$$\boldsymbol{\Phi_u} = 1\left(\frac{9429.1}{1.60\times10^6}\right)\left(\frac{1.4495^2}{1.4495^2}\right) = \mathbf{0.006}$$

4.3.8 Theoretical Fluorescence Lifetime ($\boldsymbol{\tau_F}$)

The theoretical fluorescence lifetime is defined as the theoretical average time of the molecules to stay in the excitation state before emitting photons (fluorescence). It is calculated as [208]:

$$\boldsymbol{\tau_F} = \boldsymbol{\tau_0} \times \boldsymbol{\Phi_F} \tag{5.8}$$

Where $\boldsymbol{\tau_F}$ is the fluorescence lifetime (ns), $\boldsymbol{\tau_0}$ is the theoretical radiative lifetime (ns) and $\boldsymbol{\Phi_F}$ is the fluorescence quantum yield.

From equation (5.8), the fluorescence lifetime of P-**4** is calculated as:

$\boldsymbol{\tau_F}$ = 0.006 × 12.8 = **0.08 ns**

Table 4.5 shows the remaining fluorescence lifetime of P-**5** and P-**6**. Compounds P-**4** and P-**6** have shorter fluorescence lifetime making them weak emitters compared to P-**5** that has a longer fluorescence lifetime leading to a low photon turnover rates.

Table 4.5. Theoretical Fluorescence Lifetime of P-**4** - P-**6** in $CHCl_3$

Compound	$\boldsymbol{\Phi_F}$	$\boldsymbol{\tau_0}$	$\boldsymbol{\tau_F}$
P-**4**	0.006	12.80	0.08
P-**5**	0.133	13.30	1.77
P-**6**	0.007	39.60	0.28

4.3.9 Fluorescence Rate Constant ($\mathbf{k}_{\boldsymbol{F}}$)

The theoretical fluorescence rate constant for the compounds is calculated as:

$$\mathbf{k}_{\boldsymbol{F}} = \frac{1}{\boldsymbol{\tau_0}} \tag{5.9}$$

Where $\mathbf{k}_{\boldsymbol{F}}$ is the fluorescence rate constant (s^{-1}) and $\boldsymbol{\tau_0}$ is the theoretical radiative lifetime (ns).

From equation (5.9), the fluorescence rate constant of P-**4** was calculated as:

$$\mathbf{k}_{F} = \frac{1}{1.28 \times 10^{-8}} = \mathbf{7.81 \times 10^{7}\ s^{-1}}$$

Table 4.6 shows the theoretical fluorescence rate constant of P-**4** - P-**6**.

Table 4.6. Theoretical Fluorescence Rate Constant of P-**4** - P-**6** in $CHCl_3$

Compound	$\boldsymbol{\tau_0}$	$\mathbf{k}_{F}$ (s^{-1})
P-**4**	12.80	7.81×10^{7}
P-**5**	13.30	7.52×10^{7}
P-**6**	39.60	2.53×10^{7}

4.3.10 Rate Constant of Radiationless Deactivation ($\mathbf{k}_{d}$)

The rate constant of radiationless deactivation of the compounds was calculated as:

$$\mathbf{k}_{d} = \left(\frac{\mathbf{k}_{F}}{\boldsymbol{\tau_0}}\right) - \mathbf{k}_{F} \tag{5.10}$$

Where $\mathbf{k}_{d}$ is the rate constant of radiationless deactivation (s^{-1}), $\mathbf{k}_{F}$ is the fluorescence rate constant (s^{-1}) and $\boldsymbol{\tau_0}$ is the theoretical radiative lifetime (ns).

From equation (5.10), the fluorescence rate constant of P-**4** was calculated as:

$$\mathbf{k}_{d} = \left(\frac{7.81 \times 10^{7}}{0.008}\right) - 7.81 \times 10^{7} = \mathbf{7.81 \times 10^{7}\ s^{-1}}$$

Table 4.7 shows the rate constant of radiationless deactivation of P-**4** - P-**6**.

Table 4.7. Rate Constant of Radiationless Deactivation of P-**4** - P-**6** in $CHCl_3$

Compound	$\boldsymbol{\tau_0}$	$\mathbf{k}_{F}$ (s^{-1})	$\mathbf{k}_{d}$ (s^{-1})
P-**4**	12.80	7.81×10^{7}	1.29×10^{10}
P-**5**	13.30	7.52×10^{7}	4.90×10^{8}
P-**6**	39.60	2.53×10^{7}	3.58×10^{9}

CHAPTER 5

RESULTS AND DISCUSSION

The study aims at designing and synthesizing low band-gap bay-substituted perylene-bisimides to increase the solar light harvesting properties, as potential sensitizers for dye-sensitized solar cell application. In order to accomplish the aim of the study, a number of various donor substituents are introduced at the core positions of the perylene unit as depicted in Figure 5.1. The experimental procedure involves a systematic synthesis, functionalization and purification of the novel target molecules shown in Figure 5.1.

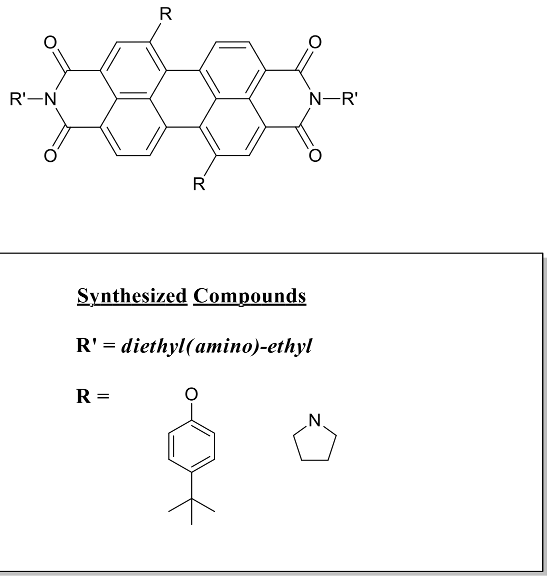

Figure 5.1. Schematic representation of the synthesized target structures

5.1 Chemical Synthesis

The synthesis of the proposed target structures at the bay-position starts with the halogenation of the perylene-3,4,9,10-tetracarboxylic bisanhydride (PBA), in accordance with the procedures outlined in the BASF patent [170] (Scheme 2.3). Under the applied experimental conditions, a respective 1,7-dibromo-, 1,6-dibromo and 1,6,7,-tribromo-PBA, are produced from the reaction as regioisomeric mixtures [171].

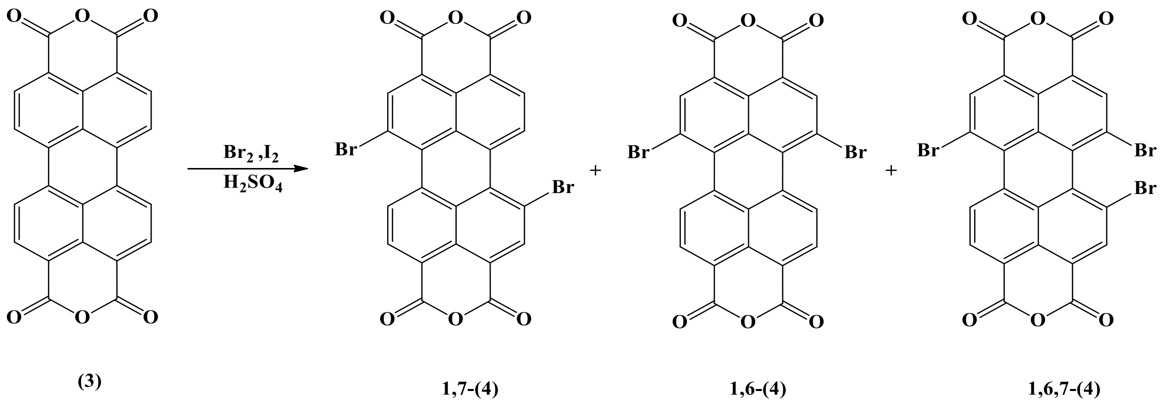

Scheme 2.3. Schematic representation of the bromination of perylene bisanhydride

Due to the insolubility of the resultant isomeric mixture, the synthesized bay-substituted compounds from this mixture are not isomerically pure. A recent research has demonstrated that the optical and electrochemical properties of the 1,6- and 1,7-substituted perylene bis-imides (PBIs) can be distinctly different [205]. This requires the separation of the resulting isomers from the aforementioned reaction where this has been proven difficult if not impossible.

Nevertheless, a new route for the synthesis of the isomerically pure 1,7-dibrominated perylene compounds have recently been reported [200]. The reported synthons are outstanding starting materials for the synthesis of a large variety of the bay-position-substituted compounds and with the advantage of controlling the optical and electrochemical properties of the target materials. Therefore, in this study, our synthetic strategy was based on the reaction pathway shown in Scheme 2.4. The significant intermediates in this scheme are perylene-3,4,9,10-tetracarboxylic tetraesters (PTEs), Scheme 2.4 (**5**) and (**6**).

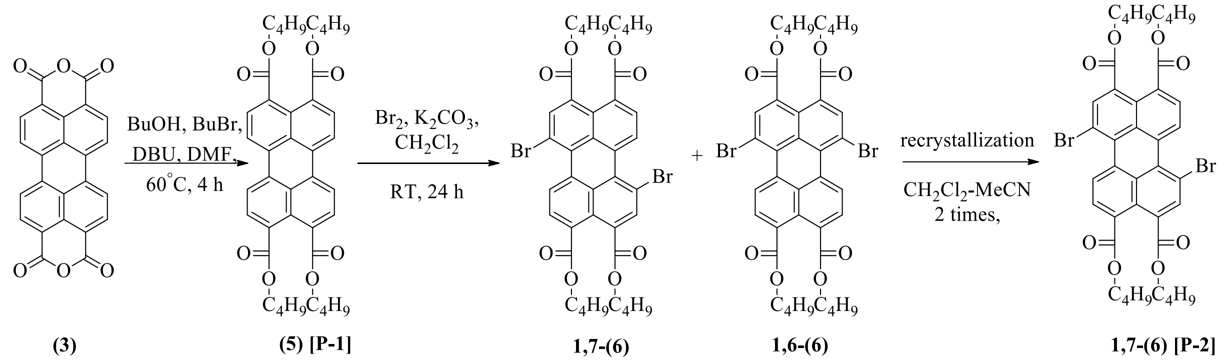

Scheme 2.4. Schematic representation of the synthesis of regioisomerically pure 1,7-Dibromoperylene-3,4,9,10-tetracarboxy Tetrabutylester (P-**2**) from PBA (**1**)

The advantage of this procedure is that the dibromination of PDA can be carried out in very mild conditions with high yield. From the resulting mixture of the dibromo 1,7-(**6**) and 1,6-(**6**), 1,7-isomer of (**6**) can be obtained in the pure form by repetitive crystallization from an acetonitrile/dichloromethane mixture [200].

Synthesis starts with the formation of perylene tetracarboxylic tetrabutylester (**5**) from commercially available Perylene-3,4,9,10-tetracarboxylic dianhydride (**3**) in Scheme 2.4. In DMF, using a liphophilic base 1,8-diazabicyclo[5.4.0]undec-7-ene (DBU) together with butanol and n-butyl bromide leads to the tetrabutylester (**5**) with excellent yield. Subsequent bromination at the bay position in dichloromethane can be carried out at mild conditions, in fact at room temperature. The bromination product is an isomeric mixture of (1,7) and (1,6) isomers. NMR analysis revealed that (1,7)/(1,6) isomeric ratio is 4/1. Repetitive crystallization from acetonitrile / dichloromethane mixture leads to the isolation of (1,7) isomer of (**6**) in pure form (see Scheme 2.4).

The synthesis of isomerically pure 1,7-Dibromoperylene-3,4,9,10-tetracarboxylic bisanhydride in Scheme 2.5 (**7**) can be achieved by an acid catalyzed dehydration reaction.

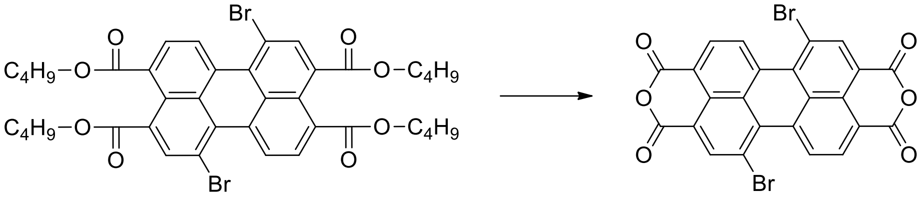

1,7-(6) [P-2]

(8) [P-X]

Scheme 2.5. Tetraester to Bisanhydride formation

The study followed the imidization process with a subsequent bay-substitution strategy for the synthetic plan, en route to the design of new compounds. Imidization of an isomerically pure 1,7-dibromo perylene dianhydride with N,N-diethylene diamine was carried at mild conditions in 2-propanol/water mixture as solvent and using acetic acid as catalyst.

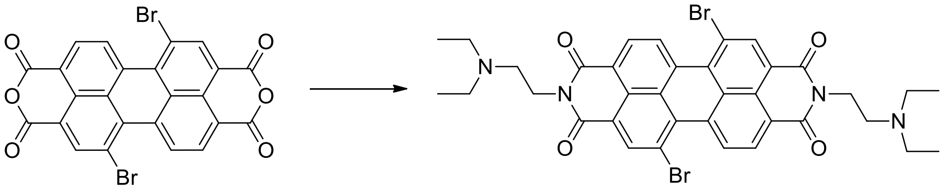

(8) [P-X]

(9) [P-4]

Scheme 2.6. Bisimide formation

This compound is a key intermediate structure in synthesizing isomerically pure 1,7-bay-substituted perylene diimide compounds bearing various bay-substituents. The design involves the attachment of electron donating groups to the perylene ring at 1, 7-positions leading to two novel bay-substituted perylene bisimide compounds (P-**5** and P-**6**).

In order to attach phenoxy groups, we carried out nucleophilic substitution reactions that involve double aromatic substitution. The reaction was carried out in dry toluene as solvent at 90 °C, with a mild base K_2CO_3 and crown-ether (18-crown-6) as phase transfer catalyst. The desired product was obtained in pure form after column chromatographic separation with a good yield of 69 %.

Secondary cyclic amines like pyrrolidine are known to be good electron-donating substances. In order to investigate the effect of N-substitution and compare it with phenoxy-substitution, we synthesized the isomerically pure novel compound (P-**6**) bearing pyrrolidinyl groups at 1,7-positions of perylene-core. The synthesis of compound (P-**6**) was achieved by reacting 1,7-dibromo bisimide (P-**4**) in pyrrolidine at 60 °C. After column chromatographic separation and purification, the title "green-perylenebisimide" compound was obtained with a 70 % isolated yield.

It is reported in the literature that the perylenetetracarboxy-monoanhydride-diester, the main intermediate for the unsymmetrically substituted perylene-imides can be synthesized from a symmetrically tetra-substituted perylene esters like (**3**) or (**4**), by an acid-catalyzed partial hydrolysis reaction [211].

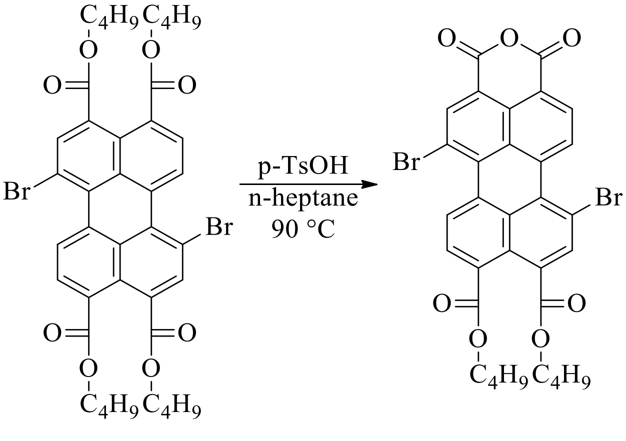

(6) [P-2] **(7) [P-3]**

Scheme 2.7. Schematic representation of the Synthesis of Regioisomerically Pure 1,7-Dibromoperylene-3,4,9,10-tetracarboxy monoanhydride-dibutylester (**7**) from (**6**)

Scheme 2.7 presents the synthesis of regioisomerically pure 1,7-Dibromoperylene-3,4,9,10-tetracarboxy monoanhydride-dibutylester (**7**) from (**6**). It was further reported that, in order to suppress the dianhydride formation, which reduces the yield of formation of (**7**), a solvent that dissolves (**6**) but hardly dissolves (**7**) is used at the reaction temperature. Our initial attempts to synthesize (**7**) in n-heptane as the solvent at 90°C resulted in a significantly lower yield than the reported 82% literature yield.

Observations from the outcome shown that besides the choice of solvent, a temperature at which the reaction is carried out and the reaction time were important factors needed to be controlled. As a result, there are ongoing efforts on optimizing the reaction conditions. It is worth to mention that (**7**) is an excellent synthon *en route* to the unsymmetrically substituted perylene imides, which will be the subject of a future work.

All synthesized compounds within this study were isolated, purified, and structurally characterized by standard characterization techniques like IR, and NMR spectroscopic techniques (see the experimental section for full synthetic procedures and characterization data).

5.2 Physical Properties

The observable features of compounds (P-**1** - P-**6**) are analyzed to distinguish one substance from the other. The physical properties of the compounds analyzed include the colour and solubility. Qualitatively, solubilities are determined at both room temperature (RT) and hot solvents (60 ℃) presented in Table 5.1. Figure 5.2 and Figure 5.3 show a picture of P-**1** - P-**6** in chloroform in daylight and under UV light. The colour of the compounds (P-**1** - P-**6**) depends on an alteration that affects the π-system. This structural alteration causes the absorption band to have longer wavelength thus, the colour of the compounds move from yellow ≥ orange ≥ pink ≥ green (i.e. bathochromic shift) while an emission of the residual energy (i.e. light) in P-**1**, P-**2**, and P-**3** causes the compound to glow (fluorescence) under UV light as shown in Figure 5.3.

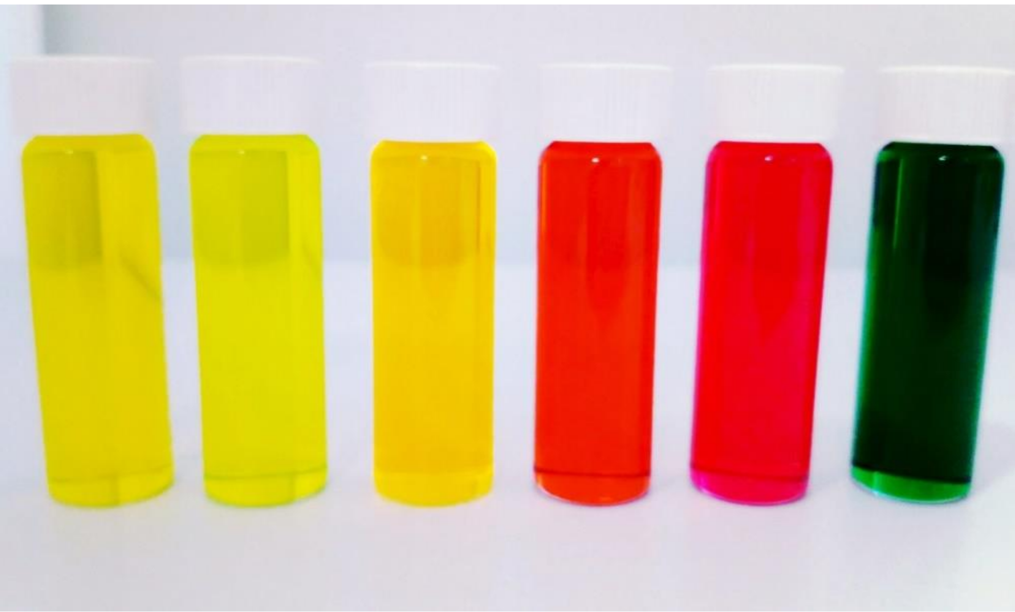

Figure 5.2. Picture of P-**1** - P-**6** in chloroform in daylight

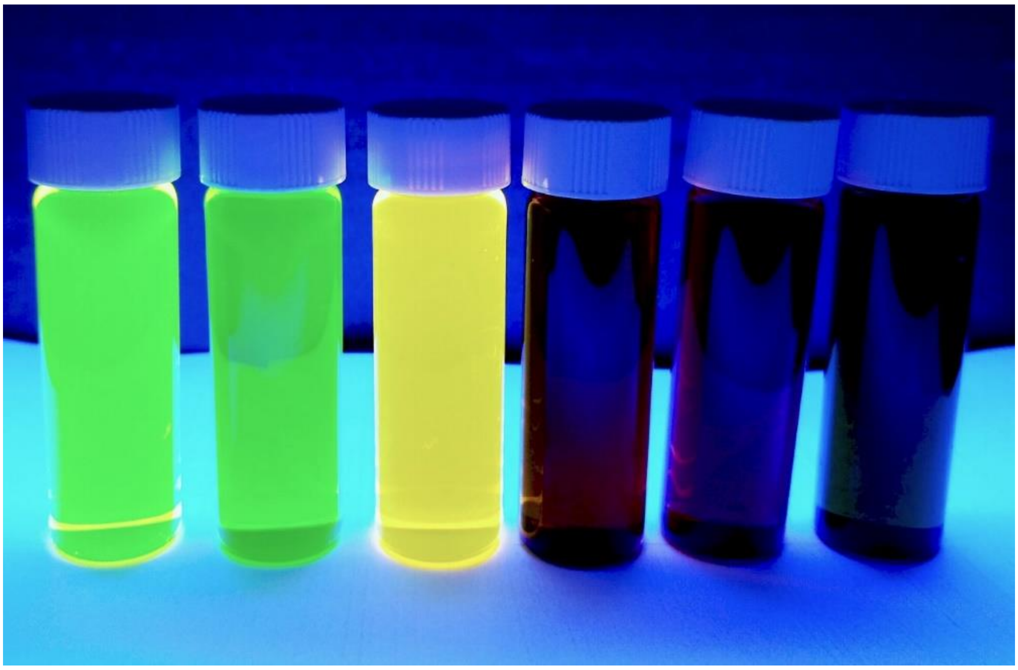

Figure 5.3. Picture of P-**1** - P-**6** in chloroform under UV light

5.3 Solubility Properties

Among some other essential properties, to be able to use as sensitizer component in a DSSC, compounds must have good solubility properties. The solubility properties of the synthesized compounds at various conditions are presented in Table 5.1. Table 5.1 shows the solubility test for P-**1** - P-**6** in a non-polar solvent (Chloroform), polar protic solvent (Ethanol), and polar aprotic solvents (Dimethylformamide and Acetonitrile). Best solubilities are observed in low-polarity solvent $CHCl_3$, where all the compounds are fully soluble in chloroform at room temperature and in hot condition. P-**1** and P-**3** are fully soluble in DMF at room temperature and in hot condition, however, P-**2**, P-**4** and P-**5** are partially soluble in DMF at room temperature but fully soluble in hot condition while P-**6** is sparingly soluble in DMF at room temperature but fully soluble in hot condition. P-**1** and P-**6** are partially soluble in ethanol at room temperature but fully soluble in hot condition, P-**2** is sparingly soluble in ethanol at room temperature but fully soluble in hot condition while P-**3**, P-**4**, and P-**5** are sparingly soluble in ethanol at room temperature but partially soluble in hot condition. P-**3** is partially soluble in acetonitrile at room temperature but fully soluble in hot condition. P-**1**, P-**2** and P-**6** are sparingly soluble in ethanol at room temperature but fully soluble in hot condition. P-**5** is sparingly soluble in acetonitrile at room temperature but partially soluble in hot condition, while P-**4** is sparingly soluble in both room temperature and in hot condition.

Core-unsubstituted perylene bisimide compounds usually show poor solubility and strong aggregate formation tendencies especially in higher polarity solvents due to the strong π-π interactions between the aromatic perylene cores. The introduction of bay substituents distorts the perylene core, leading to twisting of core ring plane, which reduces the degree of π-π interactions and aggregate formations and significantly increases the solubility.

Table 5.1. Solubility Test for P-**1** - P-**6**

Solvent	**Compounds**											
	P-**1**		P-**2**		P-**3**		P-**4**		P-**5**		P-**6**	
	RT	Hot	RT	Hot	RT	Hot	RT	Hot	RT	Hot	RT	Hot
$CHCl_3$	+++	+++	+++	+++	+++	+++	+++	+++	+++	+++	+++	+++
	Yellowish-green colour		Dark-yellow colour		Dark-yellow colour		Dark-red colour		Dark-pink colour		Dark-green colour	
EtOH	++	+++	+	+++	+	++	+	++	+	++	+	+++
	Yellowish-green colour		Dark-yellow colour		Dark-yellow colour		Pale-red colour		Pink colour		Green colour	
DMF	+++	+++	++	+++	+++	+++	++	+++	++	+++	+	+++
	Yellowish-green colour		Dark-yellow colour		Dark-yellow colour		Pale-red colour		Pale-pink colour		Pale-green colour	
MeCN	+	+++	+	+++	++	+++	+	+	+	++	+	+++
	Yellowish-green colour		Dark-yellow colour		Dark-yellow colour		Very pale-red colour		Pale-pink colour		Pale-green colour	

-Not Soluble, +++ Fully Soluble, ++ Partially Soluble, and + Sparingly Soluble. Hot: (60 °C)

5.4 Optical Properties

5.4.1 Steady-State Absorption

The optical properties of the synthesized compounds of P-**1** - P-**6** in solution were studied by ultraviolet-visible (UV-Vis) and fluorescence spectroscopy. Information on the structural features of molecules can be obtained from UV-vis spectra studied from the solution. It is noteworthy that substitutions along the peri-positions do not have much effect on the absorption properties of this class of compounds (because of the available node on the imide nitrogen HOMO and LUMO) but significantly affect aggregation and solubility properties. On the other hand, bay-substitution results in alterations not only on the electronic and optical properties but on solubility as well, resulting in substances that are more soluble. This increased the solubility results from the distortion of the perylene core where it significantly reduced the π-π interactions, leading to higher solubilities over a wider range of solvents. Figure 5.4 shows the absorption spectra of P-**1** - P-**6** recorded in $CHCl_3$ (a) and in DMF (b).

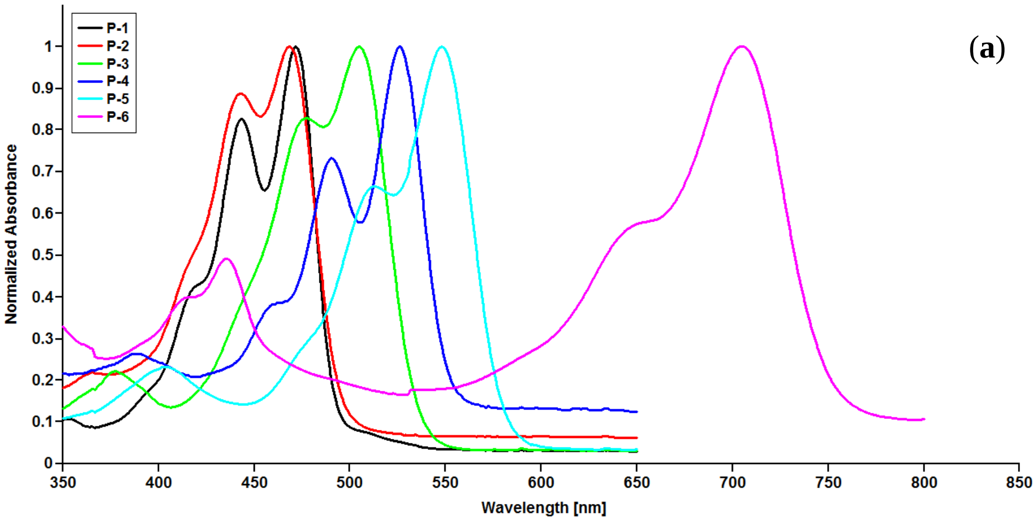

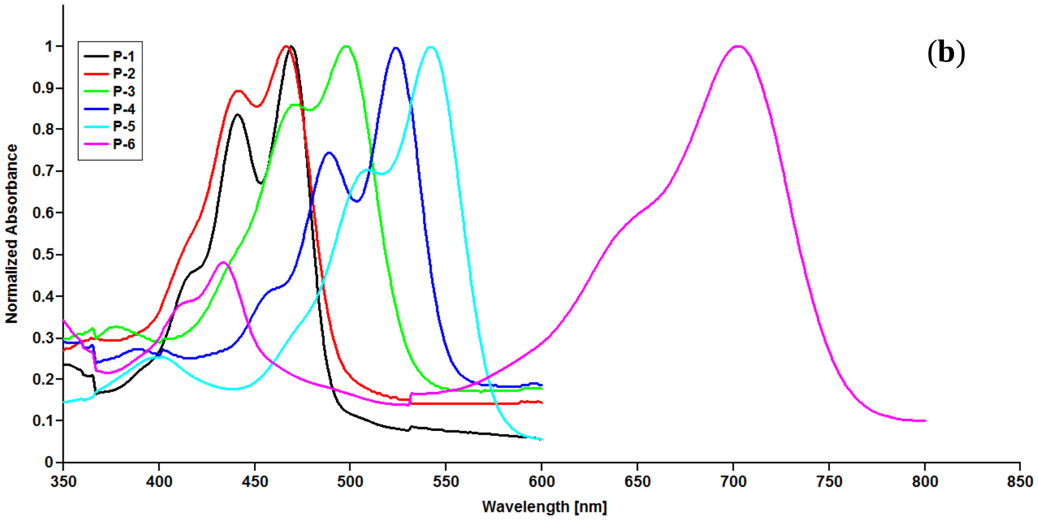

Figure 5.4. Absorption Spectra of P-**1** - P-**6** recorded in (**a**) $CHCl_3$ and (**b**) DMF

In literature, there is evidence that at the bay-positions, 1,6- and 1,7-disubstituted perylene imides may show significantly different electrochemical and photophysical properties [205]. Therefore, the isomerically pure 1,7-substituted compounds (P-**4**, P-**5**, and P-**6**) prepared and purified in this study are significant molecules for studying the structure-property relationship of this class of compounds.

Perylene bis-imide compounds are usually characterized with three well-defined sharp absorption bands, which are vibronic in nature ($S_0 \rightarrow S_1$ transitions). Among the synthesized compounds P-**1** - P-**6**, taking 1,7-dibromo perylene tetracarboxylic dianhydride P-**4** as parent compound (λ_{abs} = 526nm, λ_{abs} = 491 nm *in* $CHCl_3$), perylene tetracarboxylic monoanhydride compound [P-**3**] (λ_{abs} = 505 nm and λ_{abs} = 484 nm *in* $CHCl_3$), shows absorption maxima, which are 21 nm and 7 nm blue (hypsochromic) shifted respectively. Large hypsochromic shifts were observed with perylene tetracarboxylic tetraesters P-**1** (λ_{abs} = 472 nm and λ_{abs} = 443 nm *in* $CHCl_3$), and P-**2** (λ_{abs} = 468 nm and λ_{abs} = 443 nm *in* $CHCl_3$), as 33 nm and 41 nm (in the case of P-**1**), and 37 nm and 41 nm (in the case of P-**2**) respectively. It is noteworthy that among the perylene tetracarboxylic derivatives, tetraesters are the weakest in terms of electron withdrawing ability, because of their weak perylene-core ester-carbonyls orbital interactions. This type of orbital interaction that enhances delocalization of electrons are stronger in bisimide derivatives and strongest in bisanhydride derivatives which are in accordance with the electron withdrawing ability of ester < imide < anhydride groups. It is evident that the attachment of weakly electron withdrawing bromine groups further shifts the absorption maxima of P-**2** by 4 nm to lower wavelengths compared to that of P-**1**. Table 5.2 and Table 5.3 show the measured and calculated photophysical data for P-**1** - P-**6** in $CHCl_3$ and DMF respectively.

Table 5.2. Photophysical data of P-**1** - P-**6** in $CHCl_3$

Compound	**λ_{max}(nm)/ε_{max} (M^{-1} cm^{-1})**	**λ_{ems}(nm)**	**Φ_F/λ_{exc}(nm)**	**Stokes shift (nm)**	**E_s(kcal mol^{-1})**	***f***	**τ_0 (ns)**	**E_g (eV)**
P-**1**	472(29974) 443(23837)	490	-	18	60.59	0.18	18.60	2.51
P-**2**	468(32362) 443(28719)	499	-	31	61.11	0.21	15.80	2.49
P-**3**	505(41209) 484(34093)	540	-	35	56.63	0.27	14.40	2.29
P-**4**	526(57019) 491(40512)	552	0.006/460	26	54.37	0.33	12.80	2.23
P-**5**	548(53394) 512(35820)	586	0.133/460	38	52.19	0.34	13.30	2.13
P-**6**	704(32485) 436(14842)	727	0.007/460	23	40.63	0.19	39.60	1.64

A common strategy to red shift the absorption band of sensitizers, which is applied in this work as well, is to incorporate electron-donating substituents at positions that can extend the electron delocalization through the structure.

As expected, the attachment of two electron donating tert-butyl-phenoxy groups at the 1,7-positions in P-**5** resulted in 22 nm red shift of $S_0 \rightarrow S_1$ transitions with λ_{max} moving from 526 nm to 548 nm. Electronic coupling between the electron-rich tert-butylphenoxy substituents and electron-deficient perylene core accounts to such a change in absorption spectra.

The molar absorptivity of compounds P-**1** - P-**6** was measured in $CHCl_3$ and DMF as shown in Table 5.2 and Table 5.3. In order to confirm the accuracy of the molar absorptivity of the compounds, five different concentrations are measured in $CHCl_3$ and DMF. The slope (thus, ε) is analysed with four accurate points, with corresponding R-squared and Pearson's correlation obtained from the absorbance versus concentration plot.

There is a loss of vibrational energy as an electron moves from an excited state to the ground state. As a result, there is a shift in the emission spectrum to longer wavelengths compared to the absorption spectrum known as the stokes shift. It is noteworthy that, the higher the stokes shift, the greater it is to separate the excitation light from the emission light. The stokes shift for compounds P-**1** - P-**6** in $CHCl_3$ are 18, 31, 35, 26, 38, and 23 nm while in DMF are 19, 33, 47, 23, 32, and 28 nm as shown in Table 5.2 and Table 5.3.

Table 5.3. Photophysical data of P-**1** - P-**6** in DMF

Compound	**λ_{max}(nm)/ε_{max} (M^{-1} cm^{-1})**	**λ_{ems}(nm)**	**Φ_F/λ_{exc}(nm)**	**Stokes shift (nm)**	**E_s(kcal mol^{-1})**	***f***	**τ_0 (ns)**	**E_g (eV)**
P-**1**	469(46069) 441(38616)	488	-	19	60.98	0.28	23.30	2.53
P-**2**	466(31509) 441(28249)	499	-	33	61.37	0.19	17.30	2.51
P-**3**	497(32017) 469(26757)	544	-	47	57.55	0.22	17.20	2.32
P-**4**	523(38811) 488(27925)	546	-	23	54.68	0.22	19.10	2.24
P-**5**	541(35052) 508(24658)	573	-	32	52.87	0.18	24.10	2.15
P-**6**	704(27057) 433(12764)	732	-	28	40.63	0.17	45.00	1.61

The steady state UV-visible absorption spectra of P-**6** shows a broad absorption band within 400-750 nm band. Absorption maxima of lowest energy transition now shift to 704 nm. In addition to the characteristic of $S_0 \rightarrow S_1$ transition band locating λ_{max} at 704 nm, a second peak is located at 436 nm. This second peak is presumably the result of $S_0 \rightarrow S_2$ transitions.

In all cases, substitution at the bay positions resulted in bathochromic shifts of the absorption maxima, and a broadening of the absorption bands leading to the loss of three characteristic sharp absorption bands observed in core-unsubstituted perylene-bisimides originating from vibronic nature of the transitions. Observed band broadening may be the result of increased conjugation between the bay-substituents and perylene ring and/or bay-substituents induced twisting of the perylene core [212-216].

5.4.2 Steady-State Fluorescence

Fluorescence spectra of the compounds are recorded in both chloroform and DMF. Figure 5.5 shows the emission spectra of P-**1** - P-**6** in $CHCl_3$ (a) and DMF (b) while the data is summarized in Table 5.2 ($CHCl_3$) and Table 5.3 (DMF).

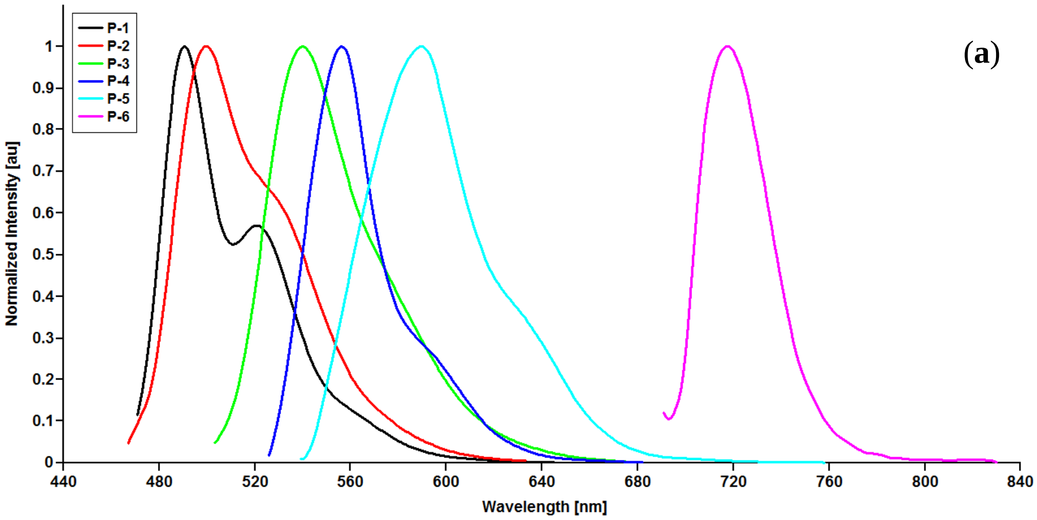

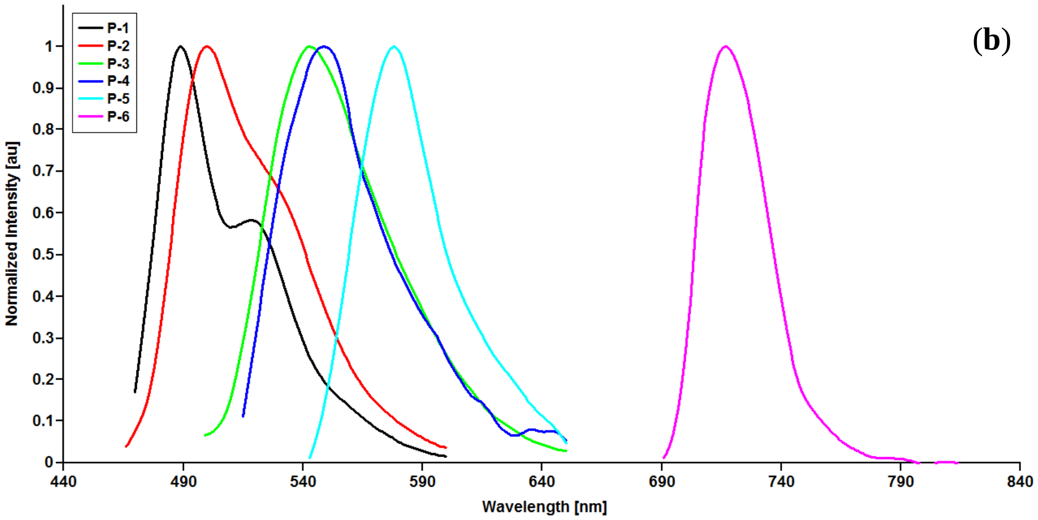

Figure 5.5. Normalized emission spectra of P-**1** - P-**6** in (**a**) $CHCl_3$ and (**b**) DMF

Similar to that observed in absorption spectra, the emission maxima of P-**5** and P-**6** red-shifted significantly compared to that of P-**4**. The emission spectrum of P-**5** is recorded with excitation at 548 nm (in $CHCl_3$) and at 542 nm (in DMF). The emission band (λ_{ems} = 586) shows 34 nm red shift in $CHCl_3$ and (λ_{ems} = 573) shows 27 nm red shift in DMF, compared to that of P-**4**. On the other hand excitation of P-**6** at 703 nm both in $CHCl_3$ (λ_{ems} = 727 nm) and in DMF (λ_{ems} = 732 nm) lead to 175 nm and 186 nm red shifts in these solvents respectively.

While P-**1** - P-**3** are fluorescent, P-**4** - P-**6** are weakly fluorescent. Fluorescence quantum yields of P-**4** - P-**6** in $CHCl_3$ are determined relative to N,N'-bis(2,6-diisopropylphenyl)-perylene-3,4,9,10-tetracarboxdiimide, the standard compound (Φ_F = 1.00). High dilution conditions are applied, where the absorbance of the compounds at the excitation wavelength (λ_{ex} =460 nm) are < 0.01 unit, in order to avoid self-quenching. The calculated quantum yields are 0.006, 0.133, and 0.007 for P-**4**, P-**5**, and P-**6** respectively. The perylene-core is strongly an electron withdrawing, therefore an introduction of substituents bearing tertiary amine units at the peri-positions as well as electron donating groups at the 1,7-positions introduces a charge transfer character to the excited states. It is essential to note that the observed extremely small quantum yields are in line with this reasoning.

Optical band gaps (E_g) have been determined from the absorption onsets as presented in Table 5.2 and Table 5.3. It is noteworthy that very similar trends and optical properties are observed in low-polarity solvent $CHCl_3$ and in polar aprotic solvent DMF.

CHAPTER 6

CONCLUSION AND FUTURE WORK

In this study, low band-gap bay-substituted perylene-bisimides were designed and synthesized successfully to increase the solar light harvesting properties for dye-sensitized solar cell applications. A number of various donor substituents were introduced at the core positions of the perylene unit. Two new isomerically pure 1,7-substituted perylene-bisimide derivatives namely; 1,7-Di(4-tert-butylphenoxy)-N,N'-bis[2-(diethylamino)ethyl]-3,4,9,10-perylene-tetracarboxylic diimide and 1,7-Di(pyrrolidinyl)-N,N'-bis[2-(diethylamino)ethyl]-3,4,9,10-perylene- tetracarboxylic diimide, have been synthesized, isolated, purified and characterized by NMR and FTIR-spectroscopy. Solubilities, as well as optical and photophysical properties, were studied by steady-state UV-visible and fluorescence spectroscopy.

The molar absorptivities of the synthesized compounds are 53394 at 548 nm in $CHCl_3$ and 35052 at 541 in DMF for 1,7-Di(4-tert-butylphenoxy)-N,N'-bis[2-(diethylamino)ethyl]-3,4,9,10-perylene-tetracarboxylic diimide and 53394 at 548 nm in $CHCl_3$ and 35052 at 541 in DMF for 1,7-Di(pyrrolidinyl)-N,N'-bis[2-(diethylamino)ethyl]-3,4,9,10-perylene- tetracarboxylic diimide. The measured molar absorptivities are high and reflect the desired high photon absorbing ability of these compounds. It was evidential that the attachment of two electron donating tert-butyl-phenoxy groups at the 1,7-positions in 1,7-Di(4-tert-butylphenoxy)-N,N'-bis[2-(diethylamino)ethyl]-3,4,9,10-perylene-tetracarboxylic diimide resulted in 18 nm red shift of $S_0 \rightarrow S_1$ transitions with λ_{max} moving from 526 nm to 543 nm.

Electronic coupling between the electron-rich tert-butyl-phenoxy substituents and electron-deficient perylene core accounts to such a change in absorption spectra. The steady state UV-visible absorption spectra of 1,7-Di(pyrrolidinyl)-N,N'-bis[2-(diethylamino)ethyl]-3,4,9,10-perylene- tetracarboxylic diimide shows a broad absorption band within the red region. Absorption maxima of lowest energy transition now shift to 704 nm. In addition to the characteristic of $S_0 \rightarrow S_1$ transition band locating λ_{max} at 704 nm, a second peak is located at 436 nm. This second peak was apparently the result of $S_0 \rightarrow S_2$ transitions.

Evidence from the study shows that the low quantum yields of 1,7-Dibromo-N,N’-Bis[2-(diethylamino)ethyl]-3,4,9,10-perylene-tetracarboxylic Diimide and, 1,7-Di(pyrrolidinyl)-N,N’-bis[2-(diethylamino)ethyl]-3,4,9,10-perylene-tetracarboxylic diimide are due to the attachment of pyrrolidine, as well as the tertiary amine groups attached at the peri-positions.

The 1,7-Di(4-tert-butylphenoxy)-N,N’-bis[2-(diethylamino)ethyl]-3,4,9,10-perylene-tetracarboxylic diimide exhibited a higher fluorescence due to the attachment of tert-butyl-phenol at the bay position of the perylene core which leads to low-photon turnover rates.

The 1,7-Di(4-tert-butylphenoxy)-N,N’-bis[2-(diethylamino)ethyl]-3,4,9,10-perylene-tetracarboxylic diimide and 1,7-Di(pyrrolidinyl)-N,N’-bis[2-(diethylamino)ethyl]-3,4,9,10-perylene- tetracarboxylic diimide have unique characteristics that are desired for a sensitizer component to be used in photovoltaic devices. Thus, the former results in a high quantum yield while the later results in a broader absorption range (350-750 nm), which allows more photons to be captured. The 1,7-Bay substitution increased the solubility of the compounds which helps improve the processability of synthesized compound.

The estimation of the energy potential of the compounds P-**1** – P-**6** in a solar spectrum perspective is depicted in Figure 5.6. A critical look at the optical properties of the compounds reveals their light harvesting potentials for electricity generation in dye-sensitized solar cell applications. The maximum extinction coefficient and the corresponding optical bandgap energies of compounds P-**1** – P-**3** happens to be lower compared to P-**4**, the parent compound. However, for a potential sensitizer that can harness the entire energy spectrum of sunlight from 3.54-1.65 eV (350-750 nm), P-**5** and P-**6** surpasses the remaining compounds. Against the background, P-**5** and P-**6** are good candidates with outstanding optical properties that can increase the photo-conversion efficiency of dye-sensitized solar cell applications.

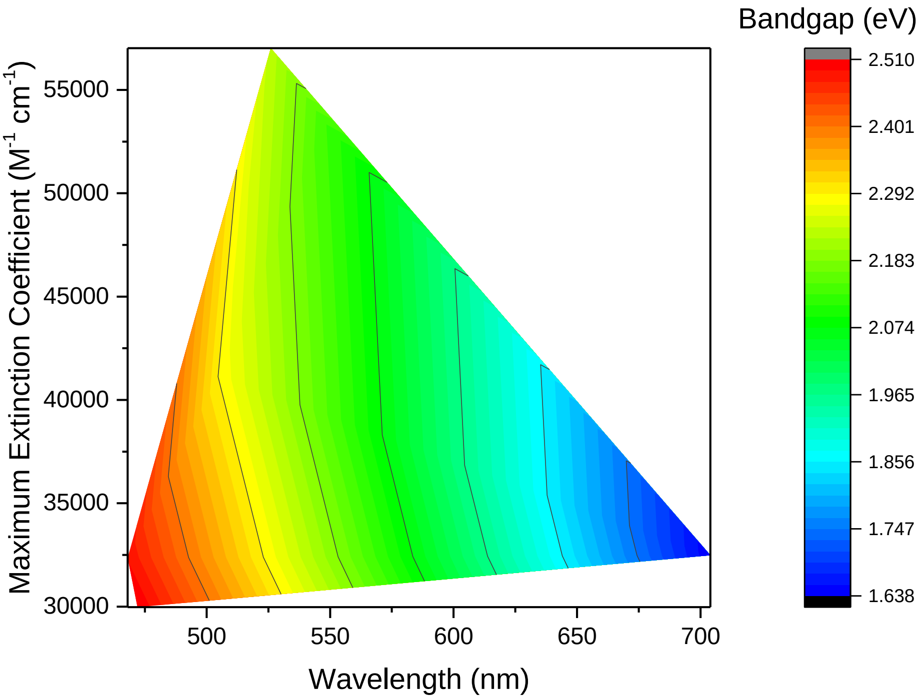

Figure 5.6. Estimation of Energy Potential

Future studies should aim at analyzing the thermal stability and electrochemical properties of 1,7-Di(4-tert-butylphenoxy)-N,N’-bis[2-(diethylamino)ethyl]-3,4,9,10-perylene-tetracarboxylic diimide and 1,7-Di(pyrrolidinyl)-N,N’-bis[2-(diethylamino) ethyl]-3,4,9,10-perylene- tetracarboxylic diimide. Finally, the bay position of 1,7-dibromoperylene-3,4,9,10-tetracarboxy monoanhydride dibutylester can further be substituted with tert-butyl-phenol / pyrrolidine, en route to the nonsymmetrical bay-substituted monoimide mono-anhydride compounds, in order to compare their properties with P-**5** and P-**6** and to ascertain its potential for dye-sensitized solar cell applications.

REFERENCES

[1] Sustainability UIotEa. A Feasibility Analysis of Installing Solar Photovoltaic Panels Over California Water Canals. UCLA Institute of the Environment and Sustainability; 2014.

[2] IPCC. IPCC Report Graphics. 2016.

[3] Owusu P, Asumadu-Sarkodie S. A Review of Renewable Energy Sources, Sustainability Issues and Climate Change Mitigation. Cogent Eng. 2016;3:1167990.

[4] Owusu PA, Asumadu-Sarkodie S, Ameyo P. A review of Ghana's water resource management and the future prospect. Cogent Eng. 2016;3:1164275.

[5] Chen CJ. Physics of solar energy: John Wiley & Sons; 2011.

[6] Liu C, Li F, Ma LP, Cheng HM. Advanced materials for energy storage. Advanced materials. 2010;22:E28-62.

[7] Li B, Wang L, Kang B, Wang P, Qiu Y. Review of recent progress in solid-state dye-sensitized solar cells. Solar Energy Materials and Solar Cells. 2006;90:549-73.

[8] Grätzel M. Low cost and efficient photovoltaic conversion by nanocrystalline solar cells. Proc Indian Acad Sci (Chem Sci). 1995;107:607-19.

[9] Nazeeruddin MK, Baranoff E, Grätzel M. Dye-sensitized solar cells: A brief overview. Solar Energy. 2011;85:1172-8.

[10] International Energy Agency. World Energy Outlook Special Report. In: Agency IE, editor. Africa Energy Outlook2014.

[11] BP. BP Statistical Review of World Energy 2015. 2015.

[12] Bloomberg New Energy Finance. Global Gross Power Generation Capacity. 2015.

[13] Chapin DM, Fuller C, Pearson G. A new silicon p-n junction photocell for converting solar radiation into electrical power. Journal of Applied Physics. 1954:676-7.

[14] Grant CD, Schwartzberg AM, Smestad GP, Kowalik J, Tolbert LM, Zhang JZ. Characterization of nanocrystalline and thin film TiO 2 solar cells with poly (3-undecyl-2, 2′-bithiophene) as a sensitizer and hole conductor. Journal of electroanalytical Chemistry. 2002;522:40-8.

[15] Tulloch GE. Light and energy—dye solar cells for the 21st century. Journal of Photochemistry and Photobiology A: Chemistry. 2004;164:209-19.

[16] Froehling PE. Dendrimers and dyes—a review. Dyes and pigments. 2001;48:187-95.

[17] Grätzel M. Solar energy conversion by dye-sensitized photovoltaic cells. Inorg Chem. 2005;44:6841-51.

[18] Zhang X, Xiao Y, Qian X. Highly efficient energy transfer in the light harvesting system composed of three kinds of boron-dipyrromethene derivatives. Organic letters. 2008;10:29-32.

[19] Chen X, Zheng Z, Ke X, Jaatinen E, Xie T, Wang D, et al. Supported silver nanoparticles as photocatalysts under ultraviolet and visible light irradiation. Green Chem. 2010;12:414-9.

[20] Odobel F, Pellegrin Y, Warnan J. Bio-inspired artificial light-harvesting antennas for enhancement of solar energy capture in dye-sensitized solar cells. Energy Environ Sci. 2013;6:2041-52.

[21] Kamat PV. Quantum dot solar cells. Semiconductor nanocrystals as light harvesters†. The Journal of Physical Chemistry C. 2008;112:18737-53.

[22] Youngblood WJ, Lee S-HA, Maeda K, Mallouk TE. Visible light water splitting using dye-sensitized oxide semiconductors. Acc Chem Res. 2009;42:1966-73.

[23] Bach U, Lupo D, Comte P, Moser J, Weissörtel F, Salbeck J, et al. Solid-state dye-sensitized mesoporous TiO2 solar cells with high photon-to-electron conversion efficiencies. Nature. 1998;395:583-5.

[24] Stathatos E, Lianos P, Falaras P, Siokou A. Photocatalytically deposited silver nanoparticles on mesoporous TiO2 films. Langmuir. 2000;16:2398-400.

[25] Zhao D, Peng T, Lu L, Cai P, Jiang P, Bian Z. Effect of annealing temperature on the photoelectrochemical properties of dye-sensitized solar cells made with mesoporous TiO2 nanoparticles. The Journal of Physical Chemistry C. 2008;112:8486-94.

[26] Hartmann P, Lee D-K, Smarsly BM, Janek J. Mesoporous TiO2: comparison of classical sol− gel and nanoparticle based photoelectrodes for the water splitting reaction. ACS nano. 2010;4:3147-54.

[27] Peng T, Fan K, Zhao D, Chen J. Enhanced Energy Conversion Efficiency of Mg2+-Modified Mesoporous TiO2 Nanoparticles Electrodes for Dye-Sensitized Solar Cells. The Journal of Physical Chemistry C. 2010;114:22346-51.

[28] Wang M, Chamberland N, Breau L, Moser J-E, Humphry-Baker R, Marsan B, et al. An organic redox electrolyte to rival triiodide/iodide in dye-sensitized solar cells. Nat Chem. 2010;2:385-9.

[29] Papageorgiou N, Maier W, Grätzel M. An iodine/triiodide reduction electrocatalyst for aqueous and organic media. Journal of the electrochemical Society. 1997;144:876-84.

[30] Boschloo G, Häggman L, Hagfeldt A. Quantification of the effect of 4-tert-butylpyridine addition to I-/I3-redox electrolytes in dye-sensitized nanostructured TiO2 solar cells. The Journal of Physical Chemistry B. 2006;110:13144-50.

[31] Gibson EA, Le Pleux L, Fortage Jrm, Pellegrin Y, Blart E, Odobel F, et al. Role of the triiodide/iodide redox couple in dye regeneration in p-type dye-sensitized solar cells. Langmuir. 2012;28:6485-93.

[32] Wei D. Dye sensitized solar cells. Int J Mol Sci. 2010;11:1103-13.

[33] Ameen S, Akhtar MS, Kim YS, Yang O-B, Shin H-S. Sulfamic acid-doped polyaniline nanofibers thin film-based counter electrode: application in dye-sensitized solar cells. The Journal of Physical Chemistry C. 2010;114:4760-4.

[34] Robertson N. Optimizing Dyes for Dye-Sensitized Solar Cells. Angewandte Chemie International Edition. 2006;45:2338-45.

[35] Suzuki K, Yamaguchi M, Kumagai M, Yanagida S. Application of Carbon Nanotubes to Counter Electrodes of Dye-sensitized Solar Cells. Chem Lett. 2003;32:28-9.

[36] Imahori H, Umeyama T, Ito S. Large π-aromatic molecules as potential sensitizers for highly efficient dye-sensitized solar cells. Acc Chem Res. 2009;42:1809-18.

[37] Li Q, Wu J, Tang Q, Lan Z, Li P, Lin J, et al. Application of microporous polyaniline counter electrode for dye-sensitized solar cells. Electrochemistry Communications. 2008;10:1299-302.

[38] Ferber J, Luther J. Computer simulations of light scattering and absorption in dye-sensitized solar cells. Solar Energy Materials and Solar Cells. 1998;54:265-75.

[39] Chen J, Li K, Luo Y, Guo X, Li D, Deng M, et al. A flexible carbon counter electrode for dye-sensitized solar cells. Carbon. 2009;47:2704-8.

[40] Ito S, Murakami TN, Comte P, Liska P, Grätzel C, Nazeeruddin MK, et al. Fabrication of thin film dye sensitized solar cells with solar to electric power conversion efficiency over 10%. Thin solid films. 2008;516:4613-9.

[41] Chiba Y, Islam A, Watanabe Y, Komiya R, Koide N, Han L. Dye-Sensitized Solar Cells with Conversion Efficiency of 11.1%. Japanese Journal of Applied Physics. 2006;45:L638-L40.

[42] Yella A, Lee H-W, Tsao HN, Yi C, Chandiran AK, Nazeeruddin MK, et al. Porphyrin-sensitized solar cells with cobalt (II/III)–based redox electrolyte exceed 12 percent efficiency. Science. 2011;334:629-34.

[43] Han L, Islam A, Chen H, Malapaka C, Chiranjeevi B, Zhang S, et al. High-efficiency dye-sensitized solar cell with a novel co-adsorbent. Energy Environ Sci. 2012;5:6057-60.

[44] Nazeeruddin MK. Engineering of efficient panchromatic sensitizers for nanocrystalline TiO2-based solar cells. J Am Chem Soc. 2001;123:1613-24.

[45] Yu J, Fan J, Lv K. Anatase TiO 2 nanosheets with exposed (001) facets: improved photoelectric conversion efficiency in dye-sensitized solar cells. Nanoscale. 2010;2:2144-9.

[46] Yanagida M, Onozawa-Komatsuzaki N, Kurashige M, Sayama K, Sugihara H. Optimization of tandem-structured dye-sensitized solar cell. Solar Energy Materials and Solar Cells. 2010;94:297-302.

[47] Wang H, Liu M, Zhang M, Wang P, Miura H, Cheng Y, et al. Kinetics of electron recombination of dye-sensitized solar cells based on TiO 2 nanorod arrays sensitized with different dyes. Phys Chem Chem Phys. 2011;13:17359-66.

[48] Morandeira A, López-Duarte I, O'Regan B, Martinez-Diaz MV, Forneli A, Palomares E, et al. Ru (II)-phthalocyanine sensitized solar cells: the influence of co-adsorbents upon interfacial electron transfer kinetics. J Mater Chem. 2009;19:5016-26.

[49] He J, Benkö G, Korodi F, Polívka T, Lomoth R, Åkermark B, et al. Modified phthalocyanines for efficient near-IR sensitization of nanostructured TiO2 electrode. J Am Chem Soc. 2002;124:4922-32.

[50] Ikeda M, Koide N, Han L, Sasahara A, Onishi H. Scanning tunneling microscopy study of black dye and deoxycholic acid adsorbed on a rutile TiO2 (110). Langmuir. 2008;24:8056-60.

[51] Kalyanasundaram K, Grätzel M. Applications of functionalized transition metal complexes in photonic and optoelectronic devices. Coord Chem Rev. 1998;177:347-414.

[52] Tian H, Sun L. Iodine-free redox couples for dye-sensitized solar cells. J Mater Chem. 2011;21:10592-601.

[53] Nusbaumer H, Moser J-E, Zakeeruddin SM, Nazeeruddin MK, Grätzel M. CoII (dbbip) 22+ complex rivals tri-iodide/iodide redox mediator in dye-sensitized photovoltaic cells. The Journal of Physical Chemistry B. 2001;105:10461-4.

[54] Hardin BE, Sellinger A, Moehl T, Humphry-Baker R, Moser J-E, Wang P, et al. Energy and hole transfer between dyes attached to titania in cosensitized dye-sensitized solar cells. J Am Chem Soc. 2011;133:10662-7.

[55] Li R, Liu J, Cai N, Zhang M, Wang P. Synchronously reduced surface states, charge recombination, and light absorption length for high-performance organic dye-sensitized solar cells. The Journal of Physical Chemistry B. 2010;114:4461-4.

[56] Yum J-H, Baranoff E, Wenger S, Nazeeruddin MK, Grätzel M. Panchromatic engineering for dye-sensitized solar cells. Energy Environ Sci. 2011;4:842-57.

[57] Ogura RY, Nakane S, Morooka M, Orihashi M, Suzuki Y, Noda K. High-performance dye-sensitized solar cell with a multiple dye system. Applied Physics Letters. 2009;94:073308.

[58] Islam A, Chowdhury FA, Chiba Y, Komiya R, Fuke N, Ikeda N, et al. Ruthenium (II) Tricarboxyterpyridyl Complex with a Fluorine-substituted. BETA.-Diketonato Ligand for Highly Efficient Dye-sensitized Solar Cells. Chem Lett. 2005;34:344-5.

[59] Gao S, Islam A, Numata Y, Han L. A β-diketonato ruthenium (II) complex with high molar extinction coefficient for panchromatic sensitization of nanocrystalline TiO2 film. Applied physics express. 2010;3:062301.

[60] Chen C-Y, Wang M, Li J-Y, Pootrakulchote N, Alibabaei L, Ngoc-le C-h, et al. Highly efficient light-harvesting ruthenium sensitizer for thin-film dye-sensitized solar cells. ACS nano. 2009;3:3103-9.

[61] Green MA. Third generation photovoltaics: Ultra-high conversion efficiency at low cost. Progress in Photovoltaics: Research and Applications. 2001;9:123-35.

[62] Goetzberger A, Hebling C. Photovoltaic materials, past, present, future. Solar energy materials and solar cells. 2000;62:1-19.

[63] Green MA. Third generation photovoltaics: solar cells for 2020 and beyond. Physica E: Low-dimensional Systems and Nanostructures. 2002;14:65-70.

[64] Rekioua D, Matagne E. Photovoltaic Applications Overview. Optimization of Photovoltaic Power Systems: Springer; 2012. p. 1-29.

[65] Bauer G. Photovoltaic Solar Energy Conversion: Springer; 2015.

[66] Ellis H. Characterization of dye-sensitized solar cells: Components for environmentally friendly photovoltaics. 2014.

[67] Coursera. The big question is: why we want to focus on renewable energy? 2016.

[68] Honsberg C, Bowden S. PVCDrom. 2009.

[69] Tress W. Organic Solar Cells: Springer; 2014.

[70] NREL. Reference Solar Spectral Irradiance: Air Mass 1.5. 2016.

[71] Breyer C, Gerlach A. Global overview on grid-parity. Progress in Photovoltaics: Research and Applications. 2013;21:121-36.

[72] Dufo-López R, Bernal-Agustín JL. Photovoltaic grid parity in Spain. Advances in Mechanical and Electronic Engineering: Springer; 2013. p. 235-9.

[73] Grossmann W, Grossmann I, Steininger KW. Solar electricity supply isolines of generation capacity and storage. Proc Natl Acad Sci U S A. 2015;112:3663-8.

[74] Electric S. Photovoltaic History. Solar Tech2015.

[75] Becquerel A. On electric effects under the influence of solar radiation. CR Acad Sci. 1839;9:711-4.

[76] Smith W. Effect of light on selenium during the passage of an electric current. SPIE MILESTONE SERIES MS. 1992;56:3-.

[77] Hertz H. Ueber einen Einfluss des ultravioletten Lichtes auf die electrische Entladung. Annalen der Physik. 1887;267:983-1000.

[78] Einstein A. A Heuristic Viewpoint Concerning the Production and Transformation of Light1929.

[79] Lenard P. Ueber die lichtelektrische Wirkung. Annalen der Physik. 1902;313:149-98.

[80] Einstein A. Über einen die Erzeugung und Verwandlung des Lichtes betreffenden heuristischen Gesichtspunkt. Annalen der Physik. 1905;322:132-48.

[81] Fritts CE. On a new form of selenium cell, and some electrical discoveries made by its use. American Journal of Science. 1883:465-72.

[82] Jenny D, Loferski J, Rappaport P. Photovoltaic Effect in GaAs p− n Junctions and Solar Energy Conversion. Physical Review. 1956;101:1208.

[83] Prince M. Silicon solar energy converters. Journal of Applied Physics. 1955;26:534-40.

[84] Loferski JJ. Theoretical considerations governing the choice of the optimum semiconductor for photovoltaic solar energy conversion. Journal of Applied Physics. 1956;27:777-84.

[85] Wysocki JJ, Rappaport P. Effect of temperature on photovoltaic solar energy conversion. Journal of Applied Physics. 1960;31:571-8.

[86] Shockley W, Queisser HJ. Detailed balance limit of efficiency of p-n junction solar cells. Journal of applied physics. 1961;32:510-9.

[87] Lindmayer J, Allison J. The violet cell: an improved silicon solar cell. Solar cells. 1990;29:151-66.

[88] Mohedano Martínez JB. Batteries in PV systems. 2011.

[89] Kathleen S. ARCO Solar began dying in 1990s. 2013.

[90] SolarWorld. SolarWorld History. 2016.

[91] Contreras MA, Egaas B, Ramanathan K, Hiltner J, Swartzlander A, Hasoon F, et al. Progress toward 20% efficiency in Cu (In, Ga) Se2 polycrystalline thin-film solar cells. Progress in Photovoltaics: Research and applications. 1999;7:311-6.

[92] Friedman D, Kurtz SR, Bertness K, Kibbler A, Kramer C, Olson J, et al. Accelerated publication 30.2% efficient GaInP/GaAs monolithic two-terminal tandem concentrator cell. Progress in Photovoltaics: Research and Applications. 1995;3:47-50.

[93] Wanlass M, Ahrenkiel S, Albin D, Carapella J, Duda A, Emery K, et al. GaInP/GaAs/GaInAs monolithic tandem cells for high-performance solar concentrators. Proc International Conference on Solar Concentrators for the Generation of Electricity or Hydrogen: Citeseer; 2005. p. 1-5.

[94] Grätzel M. Perspectives for dye-sensitized nanocrystalline solar cells. Progress in photovoltaics: research and applications. 2000;8:171-85.

[95] Asumadu-Sarkodie S, Owusu PA. The potential and economic viability of solar photovoltaic power in Ghana. Energ Source Part A. 2016;38:709-16.

[96] EPIA. Global Market Outlook For Photovoltaics 2014-2018. 2016.

[97] ARC UNSW. ARC Photovoltaics. 2014.

[98] Abrams NM. Efficiency Enhancement in Dye-sensitized Solar Cells Through Light Manipulation: The Pennsylvania State University; 2005.

[99] Li C, Wonneberger H. Perylene Imides for Organic Photovoltaics: Yesterday, Today, and Tomorrow. Advanced Materials. 2012;24:613-36.

[100] Li C, Liu M, Pschirer NG, Baumgarten M, Müllen K. Polyphenylene-based materials for organic photovoltaics. Chem Rev. 2010;110:6817-55.

[101] Grätzel M. Dye-sensitized solar cells. Journal of Photochemistry and Photobiology C: Photochemistry Reviews. 2003;4:145-53.

[102] Collings AF, Critchley C. Artificial photosynthesis: from basic biology to industrial application: John Wiley & Sons; 2007.

[103] Grätzel M. Conversion of sunlight to electric power by nanocrystalline dye-sensitized solar cells. Journal of Photochemistry and Photobiology A: Chemistry. 2004;164:3-14.

[104] Hagfeldt A, Grätzel M. Molecular photovoltaics. Acc Chem Res. 2000;33:269-77.

[105] O'Regan B, Gratzel M. A low-cost, high-efficiency solar cell based on dye-sensitized colloidal TiO2 films. Nature. 1991;353:737-40.

[106] Moser J. Note about the gain photoelectric currents by optical sensitization. Monatsh Chem. 1887;8:373.

[107] Moser J. Monatsh.‘Dye-sensitization of Becquerel's photo-electrochemical cell’. Chem; 1887.

[108] Tsubomura H, Matsumura M, Nomura Y, Amamiya T. Dye sensitized zinc oxide: aqueous electrolyte: platinum photocell. 1976.

[109] Gerischer H, Michel-Beyerle M, Rebentrost F, Tributsch H. Sensitization of charge injection into semiconductors with large band gap. Electrochimica Acta. 1968;13:1509-15.

[110] Tributsch H, Gerischer H. The use of semiconductor electrodes in the study of photochemical reactions. Berichte der Bunsengesellschaft für physikalische Chemie. 1969;73:850-4.

[111] Desilvestro J, Graetzel M, Kavan L, Moser J, Augustynski J. Highly efficient sensitization of titanium dioxide. J Am Chem Soc. 1985;107:2988-90.

[112] Duonghond D, Serpone N, Grätzel M. Integrated systems for water cleavage by visible light; Sensitization of TiO2 particles by surface derivatization with ruthenium complexes. Helv Chim Acta. 1984;67:1012-8.

[113] Grätzel M. Photoelectrochemical cells. Nature. 2001;414:338-44.

[114] Ardo S, Meyer GJ. Photodriven heterogeneous charge transfer with transition-metal compounds anchored to TiO 2 semiconductor surfaces. Chem Soc Rev. 2009;38:115-64.

[115] Pugliese D. New insights in Dye-sensitized Solar Cells: novel nanostructured photoanodes, metal-free dye, quasi-solid electrolytes and physics-based modeling: Politecnico di Torino; 2014.

[116] Gratzel M. Photoelectrochemical cells. Nature. 2001;414:338-44.

[117] Calzolari A, Ruini A, Catellani A. Anchor group versus conjugation: toward the gap-state engineering of functionalized ZnO (1010) surface for optoelectronic applications. J Am Chem Soc. 2011;133:5893-9.

[118] Kong F-T, Dai S-Y, Wang K-J. Review of recent progress in dye-sensitized solar cells. Advances in OptoElectronics. 2007;2007.

[119] Karlsson KM. Design, synthesis and properties of organic sensitizers for dye sensitized solar cells. 2011.

[120] Hara K, Dan-oh Y, Kasada C, Ohga Y, Shinpo A, Suga S, et al. Effect of additives on the photovoltaic performance of coumarin-dye-sensitized nanocrystalline TiO2 solar cells. Langmuir. 2004;20:4205-10.

[121] Mishra A, Fischer MK, Bäuerle P. Metal-free organic dyes for dye-sensitized solar cells: From structure: Property relationships to design rules. Angewandte Chemie International Edition. 2009;48:2474-99.

[122] Li C, Yum JH, Moon SJ, Herrmann A, Eickemeyer F, Pschirer NG, et al. An improved perylene sensitizer for solar cell applications. ChemSusChem. 2008;1:615-8.

[123] Edvinsson T, Li C, Pschirer N, Schöneboom J, Eickemeyer F, Sens R, et al. Intramolecular charge-transfer tuning of perylenes: spectroscopic features and performance in dye-sensitized solar cells. The Journal of Physical Chemistry C. 2007;111:15137-40.

[124] Wang Z-S, Koumura N, Cui Y, Takahashi M, Sekiguchi H, Mori A, et al. Hexylthiophene-functionalized carbazole dyes for efficient molecular photovoltaics: tuning of solar-cell performance by structural modification. Chem Mater. 2008;20:3993-4003.

[125] Ito S, Miura H, Uchida S, Takata M, Sumioka K, Liska P, et al. High-conversion-efficiency organic dye-sensitized solar cells with a novel indoline dye. Chemical Communications. 2008:5194-6.

[126] Yao Q-H, Shan L, Li F-Y, Yin D-D, Huang C-H. An expanded conjugation photosensitizer with two different adsorbing groups for solar cells. New journal of chemistry. 2003;27:1277-83.

[127] Kitamura T, Ikeda M, Shigaki K, Inoue T, Anderson NA, Ai X, et al. Phenyl-conjugated oligoene sensitizers for TiO2 solar cells. Chem Mater. 2004;16:1806-12.

[128] Hagberg DP, Yum J-H, Lee H, De Angelis F, Marinado T, Karlsson KM, et al. Molecular engineering of organic sensitizers for dye-sensitized solar cell applications. J Am Chem Soc. 2008;130:6259-66.

[129] Choi H, Baik C, Kang SO, Ko J, Kang MS, Nazeeruddin MK, et al. Highly Efficient and Thermally Stable Organic Sensitizers for Solvent-Free Dye-Sensitized Solar Cells. Angewandte Chemie International Edition. 2008;47:327-30.

[130] Hara K, Wang Z-S, Sato T, Furube A, Katoh R, Sugihara H, et al. Oligothiophene-containing coumarin dyes for efficient dye-sensitized solar cells. The Journal of Physical Chemistry B. 2005;109:15476-82.

[131] Kim S, Lee JK, Kang SO, Ko J, Yum J-H, Fantacci S, et al. Molecular engineering of organic sensitizers for solar cell applications. J Am Chem Soc. 2006;128:16701-7.

[132] Nazeeruddin MK, Pechy P, Grätzel M. Efficient panchromatic sensitization of nanocrystalline TiO 2 films by a black dye based on a trithiocyanato–ruthenium complex. Chemical Communications. 1997:1705-6.

[133] Nazeeruddin MK, Kay A, Rodicio I, Humphry-Baker R, Müller E, Liska P, et al. Conversion of light to electricity by cis-X2bis (2, 2'-bipyridyl-4, 4'-dicarboxylate)

ruthenium (II) charge-transfer sensitizers (X= Cl-, Br-, I-, CN-, and SCN-) on nanocrystalline titanium dioxide electrodes. J Am Chem Soc. 1993;115:6382-90.

[134] Nazeeruddin MK, Zakeeruddin S, Humphry-Baker R, Jirousek M, Liska P, Vlachopoulos N, et al. Acid-base equilibria of (2, 2'-bipyridyl-4, 4'-dicarboxylic acid) ruthenium (II) complexes and the effect of protonation on charge-transfer sensitization of nanocrystalline titania. Inorg Chem. 1999;38:6298-305.

[135] Nazeeruddin MK, Pechy P, Renouard T, Zakeeruddin SM, Humphry-Baker R, Comte P, et al. Engineering of efficient panchromatic sensitizers for nanocrystalline TiO2-based solar cells. J Am Chem Soc. 2001;123:1613-24.

[136] Zeng W, Cao Y, Bai Y, Wang Y, Shi Y, Zhang M, et al. Efficient dye-sensitized solar cells with an organic photosensitizer featuring orderly conjugated ethylenedioxythiophene and dithienosilole blocks. Chem Mater. 2010;22:1915-25.

[137] Lu H-P, Tsai C-Y, Yen W-N, Hsieh C-P, Lee C-W, Yeh C-Y, et al. Control of dye aggregation and electron injection for highly efficient porphyrin sensitizers adsorbed on semiconductor films with varying ratios of coadsorbate. The Journal of Physical Chemistry C. 2009;113:20990-7.

[138] Bessho T, Zakeeruddin SM, Yeh CY, Diau EWG, Grätzel M. Highly Efficient Mesoscopic Dye-Sensitized Solar Cells Based on Donor–Acceptor-Substituted Porphyrins. Angewandte Chemie International Edition. 2010;49:6646-9.

[139] Hagfeldt A, Boschloo G, Sun L, Kloo L, Pettersson H. Dye-sensitized solar cells. Chem Rev. 2010;110:6595-663.

[140] Hauch A, Georg A. Diffusion in the electrolyte and charge-transfer reaction at the platinum electrode in dye-sensitized solar cells. Electrochimica Acta. 2001;46:3457-66.

[141] Kay A, Grätzel M. Low cost photovoltaic modules based on dye sensitized nanocrystalline titanium dioxide and carbon powder. Solar Energy Materials and Solar Cells. 1996;44:99-117.

[142] Pettersson H, Gruszecki T, Bernhard R, Häggman L, Gorlov M, Boschloo G, et al. The monolithic multicell: a tool for testing material components in dye-sensitized solar cells. Progress in Photovoltaics: Research and Applications. 2007;15:113-21.

[143] Saito Y, Kitamura T, Wada Y, Yanagida S. Application of Poly (3, 4-ethylenedioxythiophene) to Counter Electrode in Dye-Sensitized Solar Cells. Chem Lett. 2002:1060-1.

[144] Bay L, West K, Winther-Jensen B, Jacobsen T. Electrochemical reaction rates in a dye-sensitized solar cell—the iodide/tri-iodide redox system. Solar energy materials and solar cells. 2006;90:341-51.

[145] Andrade L, Zakeeruddin SM, Nazeeruddin MK, Aguilar Ribeiro H, Mendes A, Graetzel M. Influence of Sodium Cations of N3 Dye on the Photovoltaic Performance and Stability of Dye-Sensitized Solar Cells. Chemphyschem. 2009;10:1117-24.

[146] Yu Z, Vlachopoulos N, Gorlov M, Kloo L. Liquid electrolytes for dye-sensitized solar cells. Dalton Transactions. 2011;40:10289-303.

[147] Nusbaumer H, Zakeeruddin SM, Moser JE, Grätzel M. An Alternative Efficient Redox Couple for the Dye-Sensitized Solar Cell System. Chemistry–A European Journal. 2003;9:3756-63.

[148] Hattori S, Wada Y, Yanagida S, Fukuzumi S. Blue copper model complexes with distorted tetragonal geometry acting as effective electron-transfer mediators in dye-sensitized solar cells. J Am Chem Soc. 2005;127:9648-54.

[149] Oskam G, Bergeron BV, Meyer GJ, Searson PC. Pseudohalogens for dye-sensitized TiO2 photoelectrochemical cells. The Journal of Physical Chemistry B. 2001;105:6867-73.

[150] Ferrere S, Zaban A, Gregg BA. Dye sensitization of nanocrystalline tin oxide by perylene derivatives. The Journal of Physical Chemistry B. 1997;101:4490-3.

[151] Wang P, Zakeeruddin SM, Moser J-E, Humphry-Baker R, Grätzel M. A solvent-free, SeCN-/(SeCN) 3-based ionic liquid electrolyte for high-efficiency dye-sensitized nanocrystalline solar cells. J Am Chem Soc. 2004;126:7164-5.

[152] Bai Y, Cao Y, Zhang J, Wang M, Li R, Wang P, et al. High-performance dye-sensitized solar cells based on solvent-free electrolytes produced from eutectic melts. Nature materials. 2008;7:626-30.

[153] Gregg BA, Pichot F, Ferrere S, Fields CL. Interfacial recombination processes in dye-sensitized solar cells and methods to passivate the interfaces. The Journal of Physical Chemistry B. 2001;105:1422-9.

[154] Ravirajan P, Peiró AM, Nazeeruddin MK, Graetzel M, Bradley DD, Durrant JR, et al. Hybrid polymer/zinc oxide photovoltaic devices with vertically oriented ZnO nanorods and an amphiphilic molecular interface layer. The Journal of Physical Chemistry B. 2006;110:7635-9.

[155] Somani PR, Radhakrishnan S. Solid state electrochemical reaction in photocells made using conducting polyaniline and sensitized with methylene blue. Journal of Solid State Electrochemistry. 2003;7:166-70.

[156] Murakoshi K, Kogure R, Wada Y, Yanagida S. Solid State Dye-Sensitized TiO2 Solar Cell with Polypyrrole as Hole Transport Layer. Chem Lett. 1997:471-2.

[157] Li J, Osasa T, Hirayama Y, Sano T, Wakisaka K, Matsumura M. Solid-state dye-sensitized solar cells using poly [2-methoxy-5-(2-ethylhexyloxy)-1, 4-phenylene-vinylene] as a hole-transporting material. Jpn J Appl Phys. 2006;45:8728.

[158] Tennakone K, Kumara G, Kumarasinghe A, Wijayantha K, Sirimanne P. A dye-sensitized nano-porous solid-state photovoltaic cell. Semiconductor Science and Technology. 1995;10:1689.

[159] O'Regan B, Schwartz DT. Efficient dye-sensitized charge separation in a wide-band-gap p-n heterojunction. Journal of applied physics. 1996;80:4749-54.

[160] Zhang C, Huang Y, Huo Z, Chen S, Dai S. Photoelectrochemical effects of guanidinium thiocyanate on dye-sensitized solar cell performance and stability. The Journal of Physical Chemistry C. 2009;113:21779-83.

[161] Peter L. Transport, trapping and interfacial transfer of electrons in dye-sensitized nanocrystalline solar cells. Journal of Electroanalytical Chemistry. 2007;599:233-40.

[162] Chen L, Li C, Müllen K. Beyond perylene diimides: synthesis, assembly and function of higher rylene chromophores. Journal of Materials Chemistry C. 2014;2:1938.

[163] Wonneberger H, Ma CQ, Gatys MA, Li C, Bauerle P, Mullen K. Terthiophene-perylene diimides: color tuning via architecture variation. J Phys Chem B. 2010;114:14343-7.

[164] Liu Y, Wang Y, Ai L, Liu Z, Ouyang X, Ge Z. Perylenebisimide regioisomers: Effect of substituent position on their spectroscopic, electrochemical, and photovoltaic properties. Dyes and Pigments. 2015;121:363-71.

[165] Singh P, Mittal LS, Kumar S, Bhargava G, Kumar S. Perylene Diimide Appended with 8-Hydroxyquinoline for Ratiometric Detection of Cu2+ Ions and Metal Displacement Driven "Turn on" Cyanide Sensing. Journal of fluorescence. 2014;24:909-15.

[166] Uzun D, Ozser ME, Yuney K, Icil H, Demuth M. Synthesis and photophysical properties of N,N′-bis(4-cyanophenyl)-3,4,9,10-perylenebis(dicarboximide) and N,N′-bis(4-cyanophenyl)-1,4,5,8-naphthalenediimide. Journal of Photochemistry and Photobiology A: Chemistry. 2003;156:45-54.

[167] Huang C, Barlow S, Marder SR. Perylene-3,4,9,10-tetracarboxylic Acid Diimides: Synthesis, Physical Properties, and Use in Organic Electronics. The Journal of Organic Chemistry. 2011;76:2386-407.

[168] Dubey RK, Efimov A, Lemmetyinen H. 1,7- And 1,6-Regioisomers of Diphenoxy and Dipyrrolidinyl Substituted Perylene Diimides: Synthesis, Separation, Characterization, and Comparison of Electrochemical and Optical Properties. Chem Mater. 2011;23:778-88.

[169] Wurthner F. Perylene bisimide dyes as versatile building blocks for functional supramolecular architectures. Chemical Communications. 2004:1564-79.

[170] Böhm A, Arms H, Henning G, Blaschka P. German Pat. DE 19547209 A1, 1997. Chem Abstr1997. p. 96569g.

[171] Würthner F, Stepanenko V, Chen Z, Saha-Möller CR, Kocher N, Stalke D. Preparation and Characterization of Regioisomerically Pure 1,7-Disubstituted Perylene Bisimide Dyes. The Journal of Organic Chemistry. 2004;69:7933-9.

[172] Berberich M, Krause A, Orlandi M, Scandola F, Würthner F. Angew Chem, Int Ed. 2008;47:6616.

[173] Dubey RK, Efimov A, Lemmetyinen H. 1, 7-And 1, 6-Regioisomers of Diphenoxy and Dipyrrolidinyl Substituted Perylene Diimides: Synthesis, Separation, Characterization, and Comparison of Electrochemical and Optical Properties†. Chem Mater. 2010;23:778-88.

[174] Zhang X, Zhan C, Zhang X, Yao J. Orientation of bromination in bay-region of perylene diimides. Tetrahedron. 2013;69:8155-60.

[175] Avlasevich Y, Li C, Müllen K. Synthesis and applications of core-enlarged perylene dyes. J Mater Chem. 2010;20:3814-26.

[176] Herbst W, Hunger K. Industrial organic pigments: production, properties, applications: John Wiley & Sons; 2006.

[177] Langhals H. Cyclic carboxylic imide structures as structure elements of high stability. Novel developments in perylene dye chemistry. Heterocycles. 1995;1:477-500.

[178] Nakazono S, Easwaramoorthi S, Kim D, Shinokubo H, Osuka A. Synthesis of Arylated Perylene Bisimides through C− H Bond Cleavage under Ruthenium Catalysis. Organic letters. 2009;11:5426-9.

[179] Battagliarin G, Li C, Enkelmann V, Müllen K. 2, 5, 8, 11-Tetraboronic ester perylenediimides: a next generation building block for dye-stuff synthesis. Organic letters. 2011;13:3012-5.

[180] Seybold G, Wagenblast G. New perylene and violanthrone dyestuffs for fluorescent collectors. Dyes and Pigments. 1989;11:303-17.

[181] Lütke Eversloh C, Li C, Müllen K. Core-extended perylene tetracarboxdiimides: the homologous series of coronene tetracarboxdiimides. Organic letters. 2011;13:4148-50.

[182] Lu X, Guo Z, Sun C, Tian H, Zhu W. Helical Assembly induced by hydrogen bonding from chiral carboxylic acids based on perylene bisimides. The Journal of Physical Chemistry B. 2011;115:10871-6.

[183] Würthner F, Osswald P, Schmidt R, Kaiser TE, Mansikkamäki H, Könemann M. Synthesis and optical and electrochemical properties of core-fluorinated perylene bisimides. Organic letters. 2006;8:3765-8.

[184] Ahrens MJ, Fuller MJ, Wasielewski MR. Cyanated perylene-3, 4-dicarboximides and perylene-3, 4: 9, 10-bis (dicarboximide): facile chromophoric oxidants for organic photonics and electronics. Chem Mater. 2003;15:2684-6.

[185] Zhao Y, Wasielewski MR. 3, 4: 9, 10-Perylenebis (dicarboximide) chromophores that function as both electron donors and acceptors. Tetrahedron Lett. 1999;40:7047-50.

[186] Gsänger M, Oh JH, Könemann M, Höffken HW, Krause AM, Bao Z, et al. A Crystal-Engineered Hydrogen-Bonded Octachloroperylene Diimide with a Twisted Core: An n-Channel Organic Semiconductor. Angewandte Chemie International Edition. 2010;49:740-3.

[187] Nolde F, Pisula W, Müller S, Kohl C, Müllen K. Synthesis and self-organization of core-extended perylene tetracarboxdiimides with branched alkyl substituents. Chem Mater. 2006;18:3715-25.

[188] Nolde F, Qu J, Kohl C, Pschirer NG, Reuther E, Müllen K. Synthesis and Modification of Terrylenediimides as High-Performance Fluorescent Dyes. Chemistry–A European Journal. 2005;11:3959-67.

[189] Kardos M. German Patent 276357, 1913. There is no corresponding record for this reference.

[190] Dubey RK. Synthesis and Function of Photoactive Donor− Acceptor Systems of Bay-Functionalized Perylene Diimide Dyes in View of 1, 7-and 1, 6-Regioisomers. Tampereen teknillinen yliopisto Julkaisu-Tampere University of Technology Publication; 1127. 2013.

[191] Kazmaier PM, Hoffmann R. A theoretical study of crystallochromy. Quantum interference effects in the spectra of perylene pigments. J Am Chem Soc. 1994;116:9684-91.

[192] Wang S, Li Y, Du C, Shi Z, Xiao S, Zhu D, et al. Dye sensitization of nanocrystalline TiO 2 by perylene derivatives. Synthetic metals. 2002;128:299-304.

[193] Zafer C, Kus M, Turkmen G, Dincalp H, Demic S, Kuban B, et al. New perylene derivative dyes for dye-sensitized solar cells. Solar energy materials and solar cells. 2007;91:427-31.

[194] Shibano Y, Umeyama T, Matano Y, Imahori H. Electron-donating perylene tetracarboxylic acids for dye-sensitized solar cells. Organic Letters. 2007;9:1971-4.

[195] Fortage J, Séverac M, Houarner-Rassin C, Pellegrin Y, Blart E, Odobel F. Synthesis of new perylene imide dyes and their photovoltaic performances in nanocrystalline TiO 2 dye-sensitized solar cells. Journal of Photochemistry and Photobiology A: Chemistry. 2008;197:156-69.

[196] Planells M, Céspedes-Guirao FJ, Gonçalves L, Sastre-Santos A, Fernández-Lázaro F, Palomares E. Supramolecular interactions in dye-sensitized solar cells. J Mater Chem. 2009;19:5818-25.

[197] Liu B, Zhu W, Wu W, Ri KM, Tian H. Hybridized ruthenium (II) complexes with high molar extinction coefficient unit: Effect of energy band and adsorption on photovoltatic performances. Journal of Photochemistry and Photobiology A: Chemistry. 2008;194:268-74.

[198] Huang C. Perylene diimide-based materials for organic electronics and optical limiting applications. 2010.

[199] Iverson IK, Tam-Chang S-W. Cascade of molecular order by sequential self-organization, induced orientation, and order transfer processes. J Am Chem Soc. 1999;121:5801-2.

[200] Sengupta S, Dubey RK, Hoek RW, van Eeden SP, Gunbas DD, Grozema FC, et al. Synthesis of regioisomerically pure 1,7-dibromoperylene-3,4,9,10-tetracarboxylic acid derivatives. J Org Chem. 2014;79:6655-62.

[201] Hassheider T, Benning SA, Kitzerow HS, Achard MF, Bock H. Color-Tuned Electroluminescence from Columnar Liquid Crystalline Alkyl Arenecarboxylates. Angewandte Chemie International Edition. 2001;40:2060-3.

[202] Langhals H, Sprenger S, Brandherm MT. Perylenamidine-imide dyes. Liebigs Annalen. 1995;1995:481-6.

[203] Baggerman J, Jagesar DC, Vallée RA, Hofkens J, De Schryver FC, Schelhase F, et al. Fluorescent perylene diimide rotaxanes: spectroscopic signatures of wheel–chromophore interactions. Chemistry–A European Journal. 2007;13:1291-9.

[204] Yuan Z, Xiao Y, Li Z, Qian X. Efficient synthesis of regioisomerically pure bis (trifluoromethyl)-substituted 3, 4, 9, 10-perylene tetracarboxylic bis (benzimidazole). Organic letters. 2009;11:2808-11.

[205] Dubey RK, Niemi M, Kaunisto K, Efimov A, Tkachenko NV, Lemmetyinen H. Direct Evidence of Significantly Different Chemical Behavior and Excited-State Dynamics of 1, 7-and 1, 6-Regioisomers of Pyrrolidinyl-Substituted Perylene Diimide. Chemistry–A European Journal. 2013;19:6791-806.

[206] Armarego WL, Chai CLL. Purification of laboratory chemicals: Butterworth-Heinemann; 2013.

[207] Friedrich M. Spectragryph - optical spectroscopy software. 1 ed2016.

[208] Turro N. Molecular photochemistry, WA Benjamim. Inc, New York. 1965.

[209] Yvon HJ. A guide to recording Fluorescence Quantum Yields. HORIBA, Jobin Yvon Ltd, Stanmore, Middlesex, UK. 2012.

[210] Williams ATR, Winfield SA, Miller JN. Relative fluorescence quantum yields using a computer-controlled luminescence spectrometer. Analyst. 1983;108:1067-71.

[211] Xue C, Sun R, Annab R, Abadi D, Jin S. Perylene monoanhydride diester: a versatile intermediate for the synthesis of unsymmetrically substituted perylene tetracarboxylic derivatives. Tetrahedron Lett. 2009;50:853-6.

[212] Chao C-C, Leung M-k, Su YO, Chiu K-Y, Lin T-H, Shieh S-J, et al. Photophysical and electrochemical properties of 1, 7-diaryl-substituted perylene diimides. The Journal of organic chemistry. 2005;70:4323-31.

[213] Sugiyasu K, Fujita N, Shinkai S. Visible-light-harvesting organogel composed of cholesterol-based perylene derivatives. Angewandte Chemie. 2004;116:1249-53.

[214] Kohl C, Weil T, Qu J, Müllen K. Towards Highly Fluorescent and Water-Soluble Perylene Dyes. Chemistry–A European Journal. 2004;10:5297-310.

[215] Osswald P, Leusser D, Stalke D, Würthner F. Perylene bisimide based macrocycles: Effective probes for the assessment of conformational effects on optical properties. Angewandte Chemie International Edition. 2005;44:250-3.

[216] Chen Z, Debije MG, Debaerdemaeker T, Osswald P, Würthner F. Tetrachloro-substituted Perylene Bisimide Dyes as Promising n-Type Organic Semiconductors: Studies on Structural, Electrochemical and Charge Transport Properties. Chemphyschem. 2004;5:137-40.